

ABSTRACT

Title of dissertation: Plasma-Neutral Equilibrium
in Centrifugally Confined Plasma

Sheung-Wah Ng
Doctor of Philosophy, 2007

Dissertation directed by: Professor Adil Hassam
Department of Physics

Plasma-neutral interactions are considered for a centrifugally confined plasma, such as the Maryland Centrifugal eXperiment (MCX), wherein a crossfield plasma rotation inhibits plasma escape along the magnetic field. Interactions along the magnetic field are considered first. Analytic and numerical solutions from a simple one-dimensional isothermal model are obtained. It is shown that for perfect recycling the neutral density at the wall is exponentially smaller than the central plasma density for strong centrifugal confinement compared to the case of no confinement for which the neutral wall density equals the central plasma density. The exponential factor is effectively $\exp(-M_s^2/2)$, where M_s is the sonic Mach number of the rotation speed. The effective neutral penetration depth along the field, of the same order as the crossfield penetration depth in the zero confinement limit, increases significantly in the strong confinement case. From the one-dimensional cold-ion calculation, the ratio of the neutral densities at the end-wall to the side-wall, $N_{||}/N_{\perp}$, is much larger than unity for weak confinement. But when M_s is about 3, the two densities are about equal and the inequality reverses beyond that.

We next extend an existing MHD numerical code to include the neutral fluid, allowing two dimensional study. Slab geometry has been used with a reasonable force model for the confinement mechanism. We found that when the rotation Mach number is about 3.7, $N_{\parallel}/N_{\perp} = 1$. The experimental relevant interaction parameter, nN , is also shown to be peaking at the side-wall rather than the end-wall when confinement is strong. A preliminary study in MCX geometry is also carried out giving first results for more realistic 2D structures.

Finally, an analytical study of momentum confinement time due to dissipative processes at the insulator is commenced. The momentum loss along the field line to the insulating end-wall might be a concern. Classical Hartmann theory suggests that the MCX results would not be obtainable. By including the Hall effect in the Hartmann problem, an analytical solution is found and has the potential to increase the momentum confinement time by factor of $\sqrt{\epsilon/\eta}$ where $\epsilon = c/\omega_{pi}L$ and η is resistivity normalized to $4\pi LVa/c^2$.

Plasma-Neutral Equilibrium in Centrifugally Confined Plasma

by

Sheung-Wah Ng

Dissertation submitted to the Faculty of the Graduate School of the
University of Maryland, College Park in partial fulfillment
of the requirements for the degree of
Doctor of Philosophy
2007

Advisory Committee:

Professor Adil B. Hassam, Advisor

Associate Professor William D. Dorland

Professor Richard F. Ellis

Senior Research Scientist Parvez N. Guzdar

Professor Eve C. Ostriker

© Copyright by
Sheung-Wah Ng
2007

Dedication

To my parents

Shu Sun Ng and Pui Yung Lee

and my wife

Danna Tang

Table of Contents

List of Tables	v
List of Figures	v
1 Introduction	1
1.1 Motivation	1
1.2 Outline of Dissertation	5
1.3 Physics Overview and Approaches	6
2 Theories on One Dimensional Equilibria	12
2.1 Crossfield Equilibria	13
2.1.1 Goldston and Rutherford Calculation Review	14
2.1.2 Modified Goldston Calculation	15
2.2 Parallel-to-field Equilibrium	18
2.2.1 Derivation of Equations and Normalization for Equivalent 1-D Problem	19
2.2.2 Baseline case: No Centrifugal Confinement	22
2.2.3 Finite Centrifugal Confinement	25
2.2.4 Strong Confinement Limit	28
2.2.5 Numerical Results	30
2.3 Summary and Conclusion	35
3 Two Dimensional Simulation	37
3.1 The Numerical Model	40
3.2 The Wall Boundary Conditions	42
3.2.1 The Recombination Layer: Spatial dependence of α_r	43
3.2.2 The Insulating End-Wall	46
3.2.3 The Conducting Side-Wall	49
3.3 Code Validation: One Dimensional Results Comparisons	51
3.4 Simulation Results	54
3.4.1 Plasma neutral system without confinement	57
3.4.2 Plasma neutral system with various confinement strengths	59
3.5 Experimental Implication	67
3.6 Conclusion	72
4 Hartmann Physics in Centrifugally Confined Plasma	75
4.1 Classical Hartmann Problem Review	80
4.1.1 Flow Across a Homogeneous Magnetic Field and the Solution	80
4.1.2 Observations and Implications	83
4.2 Analytical Solution for the Resistive-Hall Hartmann Problem	86
4.2.1 The Non-resistive (Hall-only) Limit	88
4.2.2 Implication and Discussion	91
4.3 Summary	93

5	Conclusion	98
A	Parallel-to-field Plasma-Neutral Equilibria Asymptotic Calculations	103
A.1	1D Solution with Bohm equality as the boundary condition	103
A.2	Weak Confinement Approximation with Bohm Equality Boundary Condition	104
B	Normalized Equation for the NMCX in 1D parallel direction	107
C	Estimation of $M_{s,crit}$ by combining the 1D solutions in crossfield and along the field directions	110
D	Possible Density-Variation Effect on Hartmann Problem	111
E	Preliminary Simulation in MCX Geometry	117
F	Simulation Parameters	126
	Bibliography	128

List of Tables

4.1	Momentum confinement times for MCX and fusion grade plasma due to different physics. First row: Classical viscous damping. Second row: Resistive Hartmann flow. Third row: Hall Hartmann flow. . . .	97
F.1	Physical parameters assumed for MCX	126
F.2	Comparison of the normalized physical parameters assumed for MCX and those used in the 2D simulations	127

List of Figures

1.1	Schematic diagram explaining the basic concept of centrifugal confinement. The plasma is being rotated (by a radial E-field, not shown her) across the strong external mirror B-field. The parallel-to-field component of the centrifugal force then confines the plasma in the mid-plane region.	2
1.2	Schematic diagram of the implementation of Maryland Centrifugal eXperiment(MCX). The mirror field, which is provided by the coils surrounding the chamber, ends at the insulating end plate. The E-field, which is used to drive the rotation, is maintained by a voltage difference between central axial conductor and the outer conducting chamber. Note that only the upper half of the system is shown. . . .	2
1.3	Recycling of particles. A solid surface tends to be a plasma sink. Charged particles are absorbed by the surface and recombine. A neutral particle then re-enter the system. Perfect recycling is required in a steady state without external particle source.	8
1.4	Charge-exchange process: Relatively high temperature ion receives an electron from a neutral particle at the edge region and becomes a neutral. The newly born neutral particles is more energetic than the original neutral allowing it to penetrate deeper into the plasma. . . .	9
1.5	Schematic of the main physics in the plasma-neutral particle equilibrium. Plasma recombine and recycle to neutral at the boundary while neutral particles re-enter the system through charge-exchange interaction and are ionized to refuel the plasma.	9

2.1	Normalized plasma and neutral densities profiles along the field for no centrifugal confinement. Distance along the field line, ζ , is normalized to l_0 , the neutral penetration depth. Perfect recycling wall is assumed at $l = 0$	24
2.2	Numerical solutions of the normalized plasma and neutral densities versus parallel length for the case of centrifugal confinement. A gaussian profile is assumed for effective confinement force, centered at $\zeta = 10$. Two different strengths of confinement, \tilde{g}_0 , are shown. The penetration length for the neutrals is increased in the higher confinement case due to the decrease in plasma density around the wall.	32
2.3	Neutral drag on the plasma, $-nN(u - U)$ for the two cases shown in Fig. 2.2. The small bump for the higher confinement case results from greater neutral penetration.	33
2.4	Log-linear plot for normalized neutral density vs confinement strength. The circles are the numerical solution with the $n_w = 0$ boundary condition. The triangles are for the Bohm equality boundary condition, i.e. u_w equals sound speed. Solid line and dash line are for the asymptotic solutions with the Bohm equality boundary conditions for the two different limits, $1 \ll \hat{\alpha}e^{-\tilde{g}_0}$ (which corresponds to $n_w = 0$ in the limit $\hat{\alpha} \rightarrow \infty$) and $1 \gg \hat{\alpha}e^{-\tilde{g}_0}$, respectively. The squares are for the numerical solution of the full system Eqs.(2.26)-(2.29) with Bohm equality boundary condition. Asymptotic decay rates for large \tilde{g}_0 are shown to be 0.50 and 1.0 for the two different boundary conditions respectively. Also note that decay rate for weak confinement (small \tilde{g}_0 region) has also been calculated for the $0 \leq \tilde{g}_0 \leq 0.001$ (Not shown here). The result agrees with the approximation given by Eq.(A.14).	34
3.1	Normalized plasma boundary density, $n(x_{RL})$ vs. recombination layer strength, $\alpha_{r,0}$ in one dimensional cross-field simulation. Note that n value is chosen at x_{RL} (start of RL) rather than x_w	45
3.2	Normalized neutral boundary density, $N(x_{RL})$ vs. recombination layer strength, $\alpha_{r,0}$ in one dimensional cross-field simulation. Note that N value is chosen at x_{RL} (start of RL) rather than x_w	46
3.3	Recombination coefficient, α_r as a function of x and z . It shows the recombination layer at both of the side-wall and end-wall. Note x and z variables are not in the same scale. System size in z -direction is much longer than that in x -direction.	47

3.4	Comparisons of analytical [Sect. 2] and simulation results for the case without confinement. The left plot shows the plasma and neutral densities. The right plot shows the plasma flow. Wall is located at $z = 5$. Recombination layer starts at $z = 4.95$ (shown by vertical dash-line). In units of the numerical code, $T = 0.01$, $\alpha_i = \alpha_{cx} = 0.5$ and average of total density $\langle n + N \rangle = 1$. Neutral penetration length l_0 is about 0.2.	52
3.5	Comparison of simulation and numerical modified Goldston (NMG) calculation, Eq.(2.12) for plasma density along the crossfield direction. The NMG result is obtained by shooting method. For details see the text.	55
3.6	Same as Fig. 3.5, except that N , u_x , U_x and B_z are plotted.	56
3.7	2-D plasma density profile without confinement. x is the cross-field direction and z is the parallel to field direction. Due to symmetry in x and z directions, simulation is carried out only the half-domain of both of x and z directions. Walls are located at $z = 10$ and $x = 0.5$	60
3.8	Same simulation as Fig. 3.7 but with neutral density profile plotted.	61
3.9	Comparison of the normalized neutral wall density ratio, N_{\perp}/N_{\parallel} , between the 2D simulation and the separated 1D results [see Eq.(3.14)]. No centrifugal confinement is applied.	62
3.10	Plasma density for $M_s = 0$	66
3.11	Plasma density for $M_s = 2.7$	66
3.12	Plasma density for $M_s = 3.7$	66
3.13	Neutral density for $M_s = 0$	67
3.14	Neutral density for $M_s = 2.7$	67
3.15	Neutral density for $M_s = 3.7$	67
3.16	Plots of neutral wall densities, N_{\parallel} and N_{\perp} , which are measured at (x_{core}, z_{RL}) and (x_{RL}, z_{core}) respectively, versus confinement strength (i.e. modeled rotational Mach number). Confinement is imposed through an additional ng -term defined by the gaussian function $g(z, x) = g_0 H(x) \exp[-(z - z_1)^2]$, to the momentum equation in z -direction, where $H(x) \equiv 1 - \alpha_r(x, z_{core})/\alpha_r(x_w, z_{core})$, z_1 is mid-point between the mid-plane and end-wall. The Mach number can be converted from g_0 by using Eq.(B.8). We have used $T = 0.04$, $\alpha_i = 0.5$ and $\alpha_{cx} = 0.5$	68

3.17	Vector plots of plasma flow for different confinement strengths. Left: $M_s = 0$, Middle: $M_s = 2.7$, Right: $M_s = 3.7$	69
3.18	Vector plots of neutral flow for different confinement strengths. Left: $M_s = 0$, Middle: $M_s = 2.7$, Right: $M_s = 3.7$	70
3.19	Interaction parameters nN for $M_s = 0$	72
3.20	Interaction parameters nN for $M_s = 2.7$	72
3.21	Interaction parameters nN for $M_s = 3.7$	72
3.22	Plots of the interaction parameter nN at the center of the side and end walls versus confinement strengths. Simulation details are the same as Fig. (3.16).	73
4.1	In MCX, the dominant azimuthal rotation across the strong external field which ends at the insulating end-plate. Hartmann physics is a therefore a concern.	77
4.2	A one dimensional classical Hartmann flow of a liquid metal between insulating plates. In this example, current in the (negative) x -direction is used to drive the flow in y -direction across a strong external B-field in the z -direction.	78
4.3	A solution of classical Hartmann problem for the normalized B_y/K , u_y/K and J_x/K along ζ . $(\mu, \eta, \varepsilon) = (0.04, 0.01, 0)$ is used. The Hartmann number H_a is therefore 50.	84
4.4	A solution of the Resistive-Hall Hartmann problem for the normalized B_y/K , u_y/K and J_y/K along ζ . $(\mu, \eta, \varepsilon) = (0.04, 0.01, 0.01)$ is used. Hartmann-Hall number $Q = 1/\sqrt{\mu(\eta + i\varepsilon)}$ is therefore $39 - 16i$	89
4.5	A solution of the Resistive-Hall Hartmann problem for the normalized B_x/K , u_x/K and J_x/K along ζ . $(\mu, \eta, \varepsilon) = (0.04, 0.01, 0.01)$ is used. Hartmann-Hall number $Q = 1/\sqrt{\mu(\eta + i\varepsilon)}$ is therefore $39 - 16i$	90
4.6	A solution for the Non-resistive Hartmann problem for the normalized B_y/K , u_y/K and J_y/K along ζ . $(\mu, \eta, \varepsilon) = (0.04, 0, 0.01)$ is used. Hall number $q = 1/\sqrt{2\mu\varepsilon}$ is therefore 35.	94
4.7	A solution for the Non-resistive Hartmann problem for the normalized B_x/K , u_x/K and J_x/K along ζ . $(\mu, \eta, \varepsilon) = (0.04, 0, 0.01)$ is used. Hall number $q = 1/\sqrt{2\mu\varepsilon}$ is therefore 35.	95

B.1	Modeling of the centrifugal confinement force in simulations: Plots of the model confinement force and the corresponding rotational speed square, as a function of distance along the B-field line.	109
E.1	Contour plot of recombination coefficient α_r in the MCX simulation. Red curves are the external mirror B-field. Recombination rate is then assumed to be high outside the “Last Flux Surface”	119
E.2	Contour plots of plasma density distribution at different Mach numbers. Left: 0.8, middle: 1.9, right: 2.3. The red curve lines are the external mirror B-field lines. Centrifugal confinement is clearly demonstrated.	121
E.3	Contour plots of neutral density distribution at different Mach numbers. Left: 0.8, middle: 1.9, right: 2.3. The red curve lines are the external mirror B-field lines. The end-wall neutral density is decreasing as the confinement gets better.	122
E.4	Contour plots of interaction parameter nN distribution at different Mach numbers. Left: 0.8, middle: 1.9, right: 2.3. The red curve lines are the external mirror B-field lines. The dominant interaction region is shifting from the end-region to the side which, in this case, is along the LFS.	123
E.5	Neutral flow vectors plots at different Mach numbers. Left: 0.8, middle: 1.9, right: 2.3. The red curve lines are the external mirror B-field lines. It shows the 2D flow structures in the mirror field geometry. . .	124
E.6	Charge-exchange frictional force on plasma in the azimuthal direction, $nN(u_\theta - U_\theta)$, at different Mach numbers. Left: 0.8, middle: 1.9, right: 2.3. The red curve lines are the external mirror B-field lines. The frictional force is found to be decreasing and concentrating on the end-wall for this range of Mach numbers.	125

Chapter 1

Introduction

1.1 Motivation

In the centrifugal scheme for fusion plasma confinement[1], a plasma in a shaped axial magnetic field is made to rotate crossfield with the idea that the plasma can be confined axially due to the component of the centrifugal force along the shaped field (see Fig. 1.1). This idea is recently being actively investigated in the Maryland Centrifugal eXperiment (MCX)[2, 3, 4, 5] (see Fig. 1.2 for its implementation). The success of this scheme depends greatly on the efficiency of maintaining the required supersonic azimuthal flow: if the flow is subsonic, not only is axial confinement poor, but the plasma is linearly unstable to the interchange mode since the latter mode is stabilized by large velocity shear[6, 7, 8].

In an ideal plasma, once the rotation has been set up by an initial radial current, no more torque is required to maintain the plasma rotation. However, on the longer dissipative time scales, viscosity and friction slow down the plasma and a radial current drive with circulating input power is necessary for maintaining the flow. An accounting of momentum losses is essential to assess the feasibility of centrifugal confinement as a fusion system. In a recent MCX investigation[3], momentum confinement time has been measured to be $(100 - 200\mu s)$. This time is much longer than ideal instability growth times, supporting the idea that the plasma is possibly

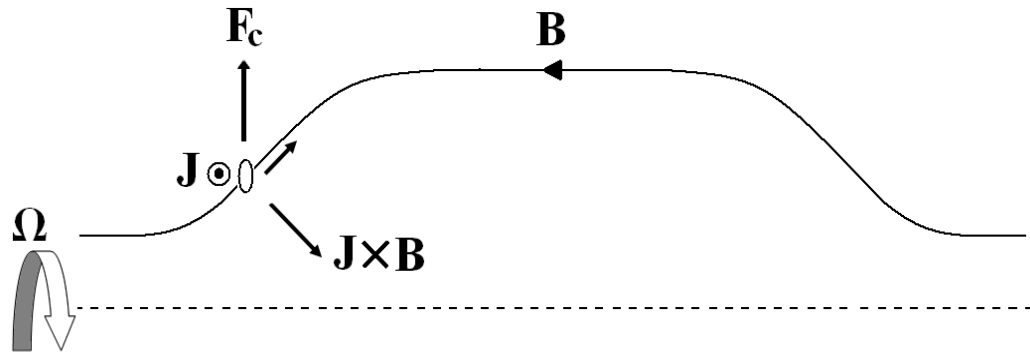


Figure 1.1: Schematic diagram explaining the basic concept of centrifugal confinement. The plasma is being rotated (by a radial E-field, not shown here) across the strong external mirror B-field. The parallel-to-field component of the centrifugal force then confines the plasma in the mid-plane region.

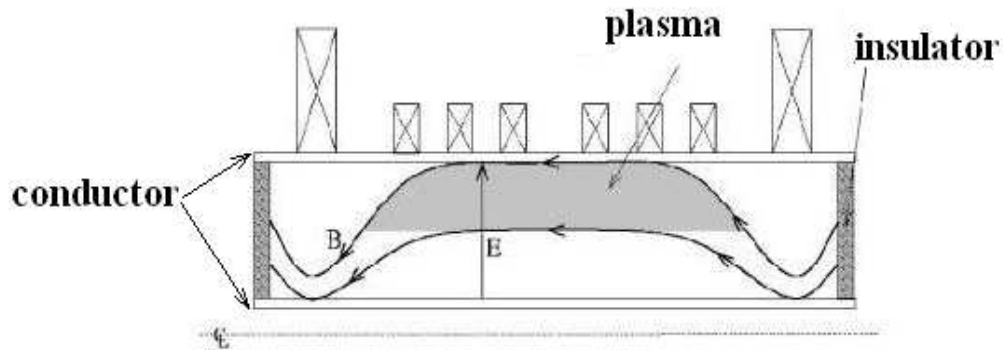


Figure 1.2: Schematic diagram of the implementation of Maryland Centrifugal experiment (MCX). The mirror field, which is provided by the coils surrounding the chamber, ends at the insulating end plate. The E-field, which is used to drive the rotation, is maintained by a voltage difference between central axial conductor and the outer conducting chamber. Note that only the upper half of the system is shown.

stable to the interchange. The time, however, is much shorter than the classical crossfield plasma viscous damping time scale ($8000\mu s$). One explanation is that the dominant drag is due to the charge-exchange (CX) interaction between plasma ions and the neutral particles emergent from the boundary region. Charge exchange loss processes are generally important in small fusion experiments on account of the smaller size and low temperature with the attendant higher fraction of neutral density in the plasma interior; thus, this is likely the explanation. In the MCX experiment, it is imperative to obtain an understanding of the neutral density distribution to ascertain whether friction due to CX is the explanation of the mentioned time scales discrepancy. This is particularly so because another potent loss mechanism in MCX could be residual turbulence from weakly unstable interchange modes. It is difficult to get a direct measurement of the latter and present experiments cannot rule out this possibility as a loss mechanism. A more precise understanding of neutral distributions would also put bounds on the residual turbulence. Studies of the edge physics in fusion devices have been of great interest in recent years (see [9, 10] for reviews and references). It has been known that edge/neutral effects are important [11, 12, 13]. A number of numerical codes have been developed, for example UEDGE [14] (fluid approach) and DEGAS [15] (kinetic approach). Various one dimensional fluid models of plasma-neutral equilibrium systems have also been developed for different configurations and parameter regimes, see for example [16, 17]. However, a plasma-neutral equilibrium study in a centrifugal confinement system is still lacking. Thus, the main part of this dissertation is to investigate the neutral density distribution in such system.

Our main motivations in studying neutrals in a centrifugally confined plasma is to understand how it affects the azimuthal rotation mechanism. We are very interested in understanding whether the frictional forces, due to the charge-exchange interactions between plasma and neutrals, would downgrade the rotation efficiency. Suppose now we model the local strength of the dragging force on a plasma system by a parameter μ . One would find that the way μ affect the plasma rotation is very different depending on the spatial dependence of μ . The dominant dragging mechanism depends on whether the strong μ region is connected to the plasma core through a strong magnetic field or not. Also, the momentum confinement times due to the two different mechanisms are very different. More explicitly, we take MCX as an example. If μ is large only around the side-wall, the core rotation would only be affected through fluid collision drag. However, if μ is large at the end-wall instead, the core crossfield flow would be hindered by both of the fluid collision drag and the magnetic field line strength, in a combinational manner. Hartmann was the first to describe this latter mechanism in 1937[18], when he studied liquid metal flow across magnetic field. In order to push a Hartmann flow, breaking the frozen-in condition is crucial. In the classical Hartmann case, this breaking occurs because there is non-zero resistivity. However, we found that, by including the Hall effect in Ohm's law, an even more prominent breaking of frozen-in is possible (due to the normalized Hall parameter is larger than the resistivity by order of magnitude). Thus, an estimation of this non-frozen-in effect in confinement time is extremely important.

1.2 Outline of Dissertation

The aim of this dissertation is to gain more understanding of the neutral distribution in a centrifugal confined plasma as well as the momentum confinement time due to the drag forces.

In Chapter 2, we give semi-analytical fluid models and solutions to one-dimensional plasma-neutral equilibria. Both the crossfield and parallel-to-field with various confinement strengths are studied. These give a baseline to our full understanding of the two-dimensional system. In general, the problem is at least 2-dimensional in a shaped field. A two dimensional analytic solution is, however, not straightforward. Goldston and Rutherford[19] have provided a one dimensional analytic solution for plasma and neutral density profiles for the crossfield problem. We review their calculation and also give a modified version which includes the density dependence of the classical crossfield diffusion coefficient. Our main focus in Chapter 2 is to study the analogous problem along the B-field line, including the centrifugal force physics. An understanding of each problem separately can then help in the understanding of the full 2D problem. Our aim is to assess the role of centrifugal confinement, which dominantly alters the density profile along the field. We find as our main result that the neutral density at the wall boundary decreases exponentially with increasing confinement strength (i.e., the rotation speed). We also find that the neutral penetration length increases with strong confinement, due to the reduced plasma density around the boundary.

However, a study of neutral penetration in centrifugally confined plasmas must

take into account the effects of centrifugal force as well as the interplay between parallel and perpendicular plasma particle losses. In Chapter 3, we study plasma-neutral equilibria of MCX by “MHD-plus-neutral” numerical simulations in two-dimension. The model system is a slab geometry with a centrifugal confinement modeling force. The main focus is how the centrifugal confinement strength changes the neutral distribution in two-dimension. An estimation of the critical rotation Mach number is obtained at which point the dominant neutral density region shifts from end-plate to the side-wall. A preliminary MCX simulation is carried out in Appendix E which gives some interesting results which is not available in the slab geometry.

In Chapter 4, we consider how Hartmann flow would affect the MCX-like rotation. We firstly review the classical Hartmann problem. Then we extend the problem to include Hall effect and solve it analytically. We also assess and compare the momentum confinement time in each case.

Finally, we conclude the dissertation in Chapter 5.

1.3 Physics Overview and Approaches

In the following, we give a qualitative introduction of the main physical phenomena that we address and the approach we use to handle them in this dissertation. In studying the neutral penetration of a system, we need to understand what the sources of the neutral particles are. In MCX, apart from the pre-fill pressure, the neutral sources are the end-wall and the side-wall (see Fig. 1.2). Since plasma-

solid/boundary interactions is a very complicated subject, as a first study, we would only consider neutral particle recycling of the same species as the plasma, ionization, charge-exchange (CX) interaction and recombination. Readers who are interested in other physical phenomena, for example the physical or chemical sputtering (and control) of impurities, sheath/presheath physics, target design, radiative power loss, should consult Post and Behrisch[20], Wesson[21] and Stangeby[16]. Fig. 1.3 shows what happens when a solid surface is placed inside a plasma. This solid surface acts as a sink of charged particles. (Indeed, a sheath is formed on the solid surface and Langmuir[22] is among the first to study it. Bohm[23] provides a sheath boundary condition which demands the plasma flow entering the sheath at least at sound speed.) After the charged particles recombine at the surface, since the newly formed neutral particle is weakly bounded to the surface, it will re-enter the system[16]. There are two possible fates for this neutral particle. First, it could be ionized very quickly at the boundary region by colliding with an electron. Second, it could undergo a resonant process called CX interaction with the plasma ion[19]. The relatively hot plasma ion receives an electron from the neutral and becomes a neutral particle while the original colder neutral particle becomes an ion. Because the energy change involved in the two particles exactly cancel, it is a resonant process and believed to be important in plasma-wall equilibria. The CX-generated neutral particle is more energetic than the original neutral particle. It allows the neutral particle to go deeper into the system and therefore a deeper neutral penetration. Fig. 1.4 shows the process pictorially. Of course, at a certain point inside the plasma, almost all of the neutral particles would be ionized due to the core's

high temperature. The plasma would then diffuse out to the wall again. Fig. 1.5 shows schematically the particles recycling in a plasma-wall system.

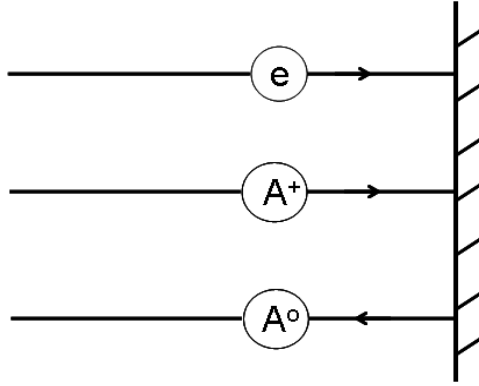


Figure 1.3: Recycling of particles. A solid surface tends to be a plasma sink. Charged particles are absorbed by the surface and recombine. A neutral particle then re-enter the system. Perfect recycling is required in a steady state without external particle source.

In order to have an accessible and intuitive understanding of the plasma-neutral equilibrium, we will approach the problem from a fluid point of view¹. (For kinetic theories and sheath physics, see [22, 24, 25]²). The MHD equations are modified to reflect the ionization, recombination and CX interaction. Ionization and recombination appear as source and sink terms in the plasma continuity equation. CX interaction not only allows the neutral particle penetrate deeper into the core, it also acts as a frictional force for the faster moving species of the two. Therefore, a CX terms is added to the plasma momentum equation. We also put the

¹Throughout this study, we will assume temperature is constant.

²See[26, 27], for recent controversy on the understanding of sheath and the fluid-sheath boundary conditions.

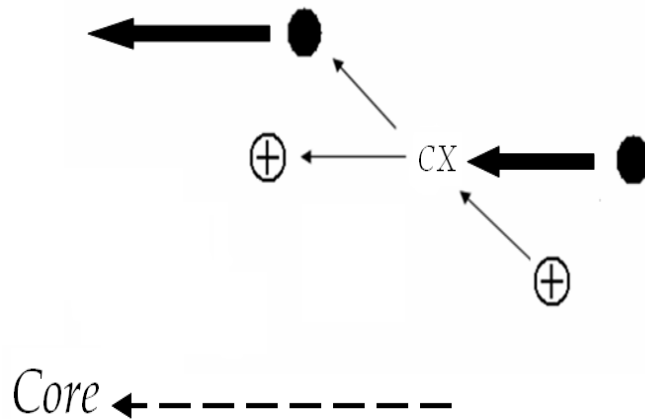


Figure 1.4: Charge-exchange process: Relatively high temperature ion receives an electron from a neutral particle at the edge region and becomes a neutral. The newly born neutral particles is more energetic than the original neutral allowing it to penetrate deeper into the plasma.

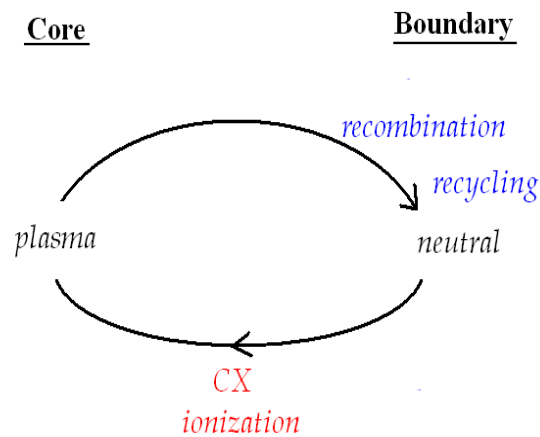


Figure 1.5: Schematic of the main physics in the plasma-neutral particle equilibrium. Plasma recombine and recycle to neutral at the boundary while neutral particles re-enter the system through charge-exchange interaction and are ionized to refuel the plasma.

plasma and neutral in an equal footing. In other words, we will treat the neutral as a separate fluid. The whole system then conserve total number of particles and momentum internally (apart from any loss due to specific boundary conditions). In using the fluid approach, we assume that the neutral charge-exchange mean free path, $\lambda \sim v_N / \langle \sigma_{cx} v_i \rangle n_i \sim v_{i,th} / \langle \sigma_{cx} v_i \rangle n_i$, where $\langle \sigma_{cx} v_i \rangle n_i$ is the CX rate and v_N and v_i are the neutral and ion speeds respectively, is much smaller than any macroscopic scale length, L . It is known that the neutral penetration length l_0 is about $v_i / n_i \sqrt{\langle \sigma_{cx} v_i \rangle \langle \sigma_{ion} v_i \rangle}$. Thus, if we use $L \sim l_0$, the fluid assumption criteria is translated to the condition $\langle \sigma_{cx} v_i \rangle / \langle \sigma_{ion} v_i \rangle \gg 1$, where $\langle \sigma_{ion} v_i \rangle n_i$ is the ionization rate. In the current operation temperature of MCX, $\langle \sigma_{cx} v_i \rangle / \langle \sigma_{ion} v_i \rangle \gtrsim 1$, which means that the fluid assumption criteria is only marginally satisfied.

The major difficulty of a plasma-wall simulation is to determine a set of self-consistent boundary conditions for the equations. In a one-dimensional parallel-to-field analysis, the boundary condition is more or less known. The Bohm criteria[23] gives the plasma flow condition and the conditions for other quantities follows. In the crossfield calculation, the boundary conditions are not very well known[16]. Yet, a relatively small plasma density at the boundary should be a reasonable assumption because it is expected that the plasma particles recombine at the relatively lower temperature walls. Based on this assumption, the analytical calculation in Chapter 2 uses $n_w = 0$ as a boundary condition. Unfortunately having plasma density vanish in the full two-dimensional simulation is not a choice as it implies an infinite Alfvén speed. Thus, we develop a recombination layer(RL) method, which ensure a relatively small (but not too small) boundary density at the wall, for the two-

dimensional simulation in Chapter 3. In principle, the parameter of the RL could be adjusted in such a way that the wall plasma density agrees with experimental data.

For a full MCX geometry analysis, we need to understand more about the boundary conditions because field lines are tilted at some parts of the boundary[28, 29]. Also the Hartmann flow physics enforces a relatively thin boundary layer without considering Hall physics. These are difficult to deal with numerically in the present stage. Yet, in Appendix E, we provide a preliminary simulation result, by bypassing these questions.

Chapter 2

Theories on One Dimensional Equilibria

In this chapter, we consider both of the crossfield and along the field one-dimensional plasma-neutral equilibria for a centrifugally confined plasma. The cross-field neutral penetration problem was considered by Lehnert[30, 31, 32] wherein he discussed the long and short neutral mean free path limits. Goldston and Rutherford[19] provide a simple analytical model for it in the short neutral mean free path limit. In section 2.1, we review Goldston and Rutherford's crossfield calculation and provide a modification to their theory by assuming the diffusion coefficient D_{\perp} is strictly classical. That is, we consider D_{\perp} proportional to plasma density n rather than being constant. Our main focus in this chapter is the parallel-to-field neutral penetration under the influence of confinement force. In section 2.2, we will tackle the plasma-neutral equilibrium problem in the parallel-to-field direction. Both the no-confinement and confinement cases are considered. In the confinement case, it is shown that the centrifugal confinement force can be represented by a gravity-like force pulling the plasma toward the core along the field. This allows us to model the confinement force in 1D. Numerical studies have been carried out for the finite confinement case. We also solve the asymptotic solution in the strong confinement limit.

2.1 Crossfield Equilibria

In this section, we study the plasma-neutral equilibria in the cross-field direction, as a complement to the parallel direction calculation. In the crossfield direction, the plasma thermal pressure is mainly balanced by the magnetic pressure. This is the celebrated idea of magnetic confinement. The neutral pressure (and therefore neutral charge-exchange) is relatively small for moderate plasma density. That is, the charge-exchange drag is secondary when considering plasma momentum. For the plasma flow, it is determined by the induction equation with the aid of the resistive ohm's law, in steady state:

$$\partial_x(u_x B_z) = \eta \partial_{xx} B_z, \quad (2.1)$$

where x is the crossfield coordinate, z is the dominant B-field direction. Because we have conducting boundary condition, the magnetic flux has to be conserved. This conservation is guaranteed. It is because the B-flux brought outward by the plasma diffusion is canceled by the resistivity inward B-flux diffusion. On the other hand, neutral is not affected by the B-field directly. The neutral pressure is balanced by the charge-exchange (CX) drag.

Goldston and Rutherford[19] have developed a simple theory for this problem. They treat the plasma diffusion coefficient as a constant while keeping the inverse density dependence for the neutral diffusion coefficient. This dependence is due to the CX interaction. Simple analytic solutions for the plasma and neutral densities and the neutral penetration depth have been obtained in their treatment. We will present it in the next section. We will see that the penetration depth in the cross-field

direction is of the same order as that in the parallel direction . It also shows that the ratio of boundary neutral density to the core plasma densities is equal to the ratio of the diffusion of the plasma to that of the neutral. Note that this behavior is not unique to the crossfield balance. A simple extension to the treatment of Goldston and Rutherford by including the density variation in the classical plasma diffusion is also presented and similar conclusion to the original treatment is obtained, although detailed solution profiles are different.

2.1.1 Goldston and Rutherford Calculation Review

In this section, we present Goldston and Rutherford’s quantitative treatment[19] on the penetration of neutral into plasma. Their starting equations are

$$\begin{aligned}\frac{\partial n}{\partial t} &= D \frac{\partial^2 n}{\partial x^2} + \alpha_i n N \\ \frac{\partial N}{\partial t} &= \frac{\partial}{\partial x} \left(D_N \frac{\partial N}{\partial x} \right) - \alpha_i n N ,\end{aligned}\tag{2.2}$$

where t is time, x is the crossfield spatial coordinate, n and N are the plasma and neutral densities respectively and $\alpha_i n$ is the ionization rate. D is the constant plasma diffusion coefficient. $D_N = T/M\alpha_{cx}n$, where $\alpha_{cx}n$ is the charge-exchange rate, is the neutral diffusion coefficient due to charge exchange. In this calculation, Goldston and Rutherford assume “perfect recycling” of particles. That is to say that whenever an ion hits the wall, it becomes a neutral particle by recombining with an electron and return back to the system. Using this assumption, and the boundary conditions $N_{core} = n_w = 0$, they obtain the following ordinary differential

equation

$$\frac{\partial n}{\partial x} = \left(\frac{\alpha_i}{4D_{N,core}n_{core}} \right)^{1/2} (n_{core}^2 - n^2) . \quad (2.3)$$

An analytic solution for Eq.(2.3) is given by,

$$\begin{aligned} n(x) &= n_{core} \tanh(x/x_0) \\ N(x) &= N_w \operatorname{sech}^2(x/x_0) \\ x_0 &= \left(\frac{4T}{M\alpha_i\alpha_{cx}n_{core}^2} \right)^{1/2} \\ \frac{N_w}{n_{core}} &= \frac{D}{2D_{N,core}} . \end{aligned} \quad (2.4)$$

First, it can be seen that the profile scale length, that is also the neutral penetration depth, x_0 is of the order of $\sqrt{T/M\alpha_i\alpha_{cx}n^2}$. Second, the ratio of the neutral wall density to the plasma core density N_w/n_{core} is inversely proportional to their diffusion coefficient. It will be seen that the above two points are indeed also applicable to the parallel direction.

2.1.2 Modified Goldston Calculation

In the last section, we presented Goldston's solution for the neutral penetration in the cross-field direction, taking account of the plasma density dependence in the neutral diffusion coefficient but not in the plasma diffusion coefficient. In this section, we would like to present a small extension of Goldston's calculation to include the plasma density variation in the plasma diffusion. It shows that the neutral penetration length in this modification is of the same order as original calculation. The only change is the details of the solution profiles.

We start with the same set of equations but with diffusion coefficient changed,

$$Dn' + D_N N' = 0 \quad (2.5)$$

$$(Dn')' = -\alpha_i n N, \quad (2.6)$$

where the prime denotes derivatives respect to x , $D = n(\eta T/B^2) \equiv nS_n$ and $D_N = (T/M\alpha_{cx})/n \equiv S_N/n$ with constants S_n and S_N . By carrying out some algebra similar to the last section, again, demanding that $n'_{core} = 0$ and $N_{core} = 0$, we find

$$(\hat{n}^2)'' = \frac{2}{3}(\hat{n}^4 - \hat{n}), \quad (2.7)$$

where densities and lengths have been rescaled with n_{core} and $l_0 = \sqrt{S_N/\alpha_i n_{core}^2} = \sqrt{T/M\alpha_i \alpha_{cx} n_{core}^2}$ respectively. By carrying out simple variable transformations, Eq.(2.7) can be solved analytically with solution

$$\ln\left(\frac{1 - \hat{n}}{1 - \hat{n}_w}\right) - \frac{1}{2} \ln\left(\frac{1 + \hat{n} + \hat{n}^2}{1 + \hat{n}_w + \hat{n}_w^2}\right) + \sqrt{3} \tan^{-1} \left[\frac{\sqrt{3}(\hat{n} - \hat{n}_w)}{2 + \hat{n} + \hat{n}_w + 2\hat{n}\hat{n}_w} \right] = -\hat{x} \quad (2.8)$$

where \hat{n}_w is the normalized plasma density at the wall assumed to be given as a boundary condition. For illustration purpose, we take $\hat{n}_w = 0$ as the boundary condition here. The neutral wall density can be found to be

$$\hat{N}_w = \frac{S_n}{3S_N} \hat{n}_{core}^2, \quad (2.9)$$

or

$$\frac{N_w}{n_{core}} = \frac{D_{core}}{3D_{N,core}}. \quad (2.10)$$

Once again, it illustrates that the ratio of the neutral wall density to the plasma core density is inversely proportional to their respective diffusion coefficient. The factor 3 reflects the detail power dependence of the coefficients on the plasma density. It

is found that the first term on the LHS of Eq.(2.8) is dominant over the second and the third term when \hat{n} is greater than 0.2. Therefore, we could approximate the solution as, in the dimensional form

$$n = (1 - e^{-x/l_0}) n_{core} . \quad (2.11)$$

Note that the analytic solution Eq.(2.8) is only applicable when the system size is much larger than l_0 so that N_{core} vanishes. However, we will see in Chapter 3 that this is not the case for MCX because the width of the system is about 20 – 30 cm while l_0 is about 5 cm. Therefore, in order to have a tool to justify our 2D simulations result, we better to have a way to find the 1D solution for a moderate size system. It turns out that we can find a high order non-linear differential equation in n by combining Eqs.(2.5) and (2.6) without imposing any boundary condition at this stage, we then have

$$(n^3)' = \frac{3S_N}{2\alpha_i} \left[\frac{(n^2)''}{n} \right]' , \quad (2.12)$$

in dimensional form. We would like to emphasize that this equation contains the same physics as the solution Eq.(2.8). The only difference is that Eq.(2.8) is obtained after imposing the infinite system size conditions, including $N_{core} = 0$ and $n'_{core} = 0$ while Eq.(2.12)'s boundary conditions are yet to be imposed. Once we get $n(x)$, the solutions for other quantities follow as, by assuming perfect recycling condition, $nu = -NU$,

$$u = \frac{\eta n' T}{2C} \quad (2.13)$$

$$N = \frac{(nu)'}{\alpha_i n} \quad (2.14)$$

$$U = -\frac{nu}{N} \quad (2.15)$$

$$B = \sqrt{2(C - nT)}, \quad (2.16)$$

where $C \equiv B_{core}^2/2 + n_{core}T$. We will return to Eqs.(2.12)-(2.16) when we validate the 2D numerical code in Chapter 3.

2.2 Parallel-to-field Equilibrium

The governing equations for a plasma and neutral fluid are,

$$\frac{\partial n}{\partial t} + \nabla \cdot (n\mathbf{u}) = \alpha_i N n \quad (2.17)$$

$$\frac{\partial M n \mathbf{u}}{\partial t} + \nabla \cdot (M n \mathbf{u} \mathbf{u}) = -T \nabla n + \mathbf{J} \times \mathbf{B} - \alpha_{cx} M N n (\mathbf{u} - \mathbf{U}) \quad (2.18)$$

$$+ \alpha_i M N n \mathbf{U} \quad (2.19)$$

$$\frac{\partial N}{\partial t} + \nabla \cdot (N \mathbf{U}) = -\alpha_i N n \quad (2.20)$$

$$\frac{\partial M N \mathbf{U}}{\partial t} + \nabla \cdot (M N \mathbf{U} \mathbf{U}) = -T \nabla N + \alpha_{cx} M n N (\mathbf{u} - \mathbf{U}) \quad (2.21)$$

$$- \alpha_i M N n \mathbf{U}, \quad (2.22)$$

where n and \mathbf{u} are the plasma density and velocity respectively and N and \mathbf{U} are the corresponding quantities for the neutrals. The products $\alpha_i n$ and $\alpha_{cx} n$ are the ionization and charge-exchange (CX) rates respectively. The last two terms in Eqs.(2.19) and (2.22) represent momentum exchange between plasmas and neutrals[33]. The ideal gas law is assumed to be true for the plasma and neutral kinetic pressures, namely $p = nT$ and $p_N = NT$ respectively. Here, we assume isothermal conditions for simplicity. Perfect recycling of neutrals, $n_w u_w = -N_w U_w$ at the boundaries will be assumed. The immediate consequence of this is that the system conserves the to-

tal number of particles, that is $\int (n + N) d^3\mathbf{x}$ is constant. The above system should be closed by the Maxwell equations for \mathbf{B} , with $\mathbf{J} \equiv \nabla \times \mathbf{B}$. However, in what follows we assume that the magnetic field is very strong and thus, to lowest order, \mathbf{B} is just the vacuum, potential field. Then, only the \mathbf{B} component of Eq.(2.19) is used and \mathbf{J} is not required for the parallel balance. Azimuthal symmetry will be assumed in the following discussion. Note the equations we are using (apart from geometry) have effectively identical physical terms to the numerical code UDEGE[14] except we always solve the full neutral momentum equation and do not use an effective diffusion coefficient. However, no isothermal assumption is used in UEDGE. Our focus here is the centrifugal confinement, which has not been studied.

2.2.1 Derivation of Equations and Normalization for Equivalent 1-D Problem

We begin by deriving equations for the two fluids for dynamics along the shaped magnetic field. The field is assumed to be purely poloidal and axisymmetric, thus

$$\mathbf{B} = -\nabla\theta \times \nabla\psi , \quad (2.23)$$

where θ is the azimuthal angle and ψ is the flux function. The flows are parallel to the field and $\mathbf{E} \times \mathbf{B}$ drifts are across the field. Thus, the flow \mathbf{u} and the electrostatic potential in steady state are related by

$$\nabla\phi = \mathbf{u} \times \mathbf{B} . \quad (2.24)$$

By noting that $\mathbf{B} \cdot \nabla \phi = 0$, we have $\phi = \phi(\psi)$. The flow can be expressed as $\mathbf{u} = u_{\parallel} \hat{b} + u_{\theta} \hat{\theta}$ where $u_{\theta} = r \phi'(\psi) \hat{\theta}$, with r as the radial coordinate. By taking the \hat{b} component of Eq.(2.19), in equilibrium, we have

$$B \partial_l (M n u_{\parallel}^2 / B) = -T \partial_l n - \alpha_{cx} M n N (u_{\parallel} - U_{\parallel}) + \alpha_i M N n U_{\parallel} + (M n / 2) \partial_l u_{\theta}^2, \quad (2.25)$$

where l is the distance along the B-field line. The last term of Eq.(2.25) is the centrifugal confinement force. It constitutes a force in the r direction with a component along the field line. In other words, the force only exists when there is a curvature in the field line. The neutrals are oblivious to the field line. We will use field line geometry for the neutrals also as, later, we will use a straight field model. We then have a set of equations, which is essentially 1-D along the field. In steady state, this set is

$$\partial_l (n u) = \alpha_i N n, \quad (2.26)$$

$$B \partial_l (M n u^2 / B) = -T \partial_l n - \alpha_{cx} M n N (u - U) + \alpha_i M N n U + M n g, \quad (2.27)$$

$$\partial_l (N u) = -\alpha_i N n, \quad (2.28)$$

$$\partial_l (M N u^2) = -T \partial_l N - \alpha_{cx} M n N (U - u) - \alpha_i M N n U, \quad (2.29)$$

where the function $g \equiv (u_{\theta}^2 / 2)'$, and the primes denote derivatives with respect to the distance l along the field lines. We have also simplified the parallel flow variables by removing their subscripts. This system of four equations is for the four unknowns n , N , u and U .

We can now normalize the system to its natural units. By normalizing the densities to the plasma core density n_{core} , time rate of change to the core ionization

rate $\alpha_i n_{core}$, and length to the scale

$$l_0 = (T/M\alpha_i\alpha_{cx}n_{core}^2)^{1/2} , \quad (2.30)$$

we have

$$(nu)' = Nn , \quad (2.31)$$

$$\hat{\alpha}n' = -\hat{\alpha}nN(u - U) + NnU + n\hat{g} , \quad (2.32)$$

$$(NU)' = -Nn , \quad (2.33)$$

$$\hat{\alpha}N' = \hat{\alpha}nN(u - U) - NnU , \quad (2.34)$$

where we have ignored the inertia terms. Note that the only two free parameters are now $\hat{\alpha} \equiv \alpha_{cx}/\alpha_i$ and $\hat{g} \equiv \partial_\zeta(u_\theta^2/2)$, where we denote ζ as the normalized length l/l_0 , with the velocity normalized to $u_0 \equiv \alpha_i n_{core} l_0 = (T/M\hat{\alpha})^{1/2} = \hat{\alpha}^{-1/2} c_s$. The prime denotes derivative with respect to ζ . It is of interest to note that the scale length l_0 originates from the CX and ionization interactions. Indeed l_0 equals the geometric average of the CX and ionization mean-free-paths, i.e. $l_0 \sim (\lambda_{cx}\lambda_i)^{1/2}$ where $\lambda_{cx} \sim c_s/n\alpha_{cx}$ and $\lambda_i \sim c_s/n\alpha_i$. The numerical value of l_0 in MCX is about 3 cm for a plasma with density 10^{20} m^{-3} and temperature 15 eV. Also for MCX, $u_\theta = \hat{\alpha}^{1/2} M_s$. In that case, the effective gravitational field $\hat{g} \sim \hat{\alpha} M_s^2 / \zeta_B$, where ζ_B is the normalized length scale of curvature of the B-field lines. It should also be noted that the validity for fluid theory depends on the assumption that the CX scale length is much smaller than the smallest macroscopic scale length. Thus, $\lambda_{cx} \sim c_s/n\alpha_{cx} \ll l_0$. This is satisfied if $\hat{\alpha}^{1/2} \gg 1$. In what follows, we will assume that $\hat{\alpha} \gg 1$, to justify the fluid limit. Where appropriate, we will assess the failure of the fluid limit(DEGAS and UEDGE code[15, 14]).

2.2.2 Baseline case: No Centrifugal Confinement

In this section, we will consider the simple case where there is no centrifugal confinement, i.e. $\hat{g} = 0$. This is a baseline of the more general confinement system. The system is then simplified to

$$(nu)' = Nn , \quad (2.35)$$

$$n' = -nN(u - U) \quad (2.36)$$

$$(NU)' = -Nn , \quad (2.37)$$

$$N' = -nN(U - u) , \quad (2.38)$$

where we have used $\hat{\alpha} \gg 1$. This set of equations describes a plasma-neutral system in which the two species interact through ionization and CX drags parallel to the magnetic field. It is the counterpart of the crossfield system as given in Goldston and Rutherford[19]. Adding Eq.(2.35) and (2.37) and assuming perfect recycling at the wall, we get

$$nu + NU = 0 . \quad (2.39)$$

Adding Eq.(2.36) and (2.38) we get

$$n + N = 1 , \quad (2.40)$$

where we have assumed the the neutral density at the center of the plasma, N_{core} vanishes. Using the last two equations, with Eq.(2.38), we have

$$N' = -NU . \quad (2.41)$$

Taking the derivative of both sides once more and using Eq.(2.37), we have a non-linear differential equation for N ,

$$N'' = N(1 - N) . \quad (2.42)$$

Integrating and using the boundary conditions that N and N' vanish at large ζ , we have

$$N' = - \left(N^2 - \frac{2}{3}N^3 \right)^{1/2} , \quad (2.43)$$

and,

$$N = \frac{3}{2} \operatorname{sech}^2 \left[\frac{\zeta}{2} + \operatorname{sech}^{-1} \left(\frac{2N_w}{3} \right)^{1/2} \right] , \quad (2.44)$$

where ζ is the normalized distance measured from the wall and N_w is the neutral density value at the wall. Note also that we are only interested in the $N' \leq 0$ solution. In order to solve the system completely, we still need a boundary condition at the wall. There are two commonly used choices, namely $n(0) = 0$, which is usually used in low temperature ($T \leq 10$ eV) “diffusion”-like regime, and the equality form of the Bohm criterion[16] for higher electron temperature, namely that the plasma flow at the wall equals sound speed, which corresponds to $u_w = -\hat{\alpha}^{1/2}$ in our units. For simplicity, we will use $n(0) = 0$ in this section and the use of the Bohm condition will be presented in Appendix A.1. Indeed, it can be shown[16] that for a system with strong CX drag the latter boundary condition is consistent with $n(0) \ll 1$. For the choice of $n(0) = 0$, we have $N_w = 1$ from Eq.(2.40). Thus $N(\zeta)$ is now known. Fig. 2.1 shows the resulting plasma and neutral density profiles. The calculation in this section is parallel to that of Ref.[19]. The N and n profiles we obtain are qualitatively similar to the crossfield problem of Goldston and Rutherford[19] except

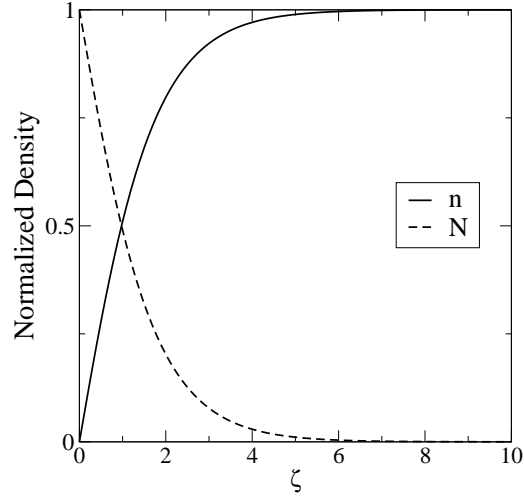


Figure 2.1: Normalized plasma and neutral densities profiles along the field for no centrifugal confinement. Distance along the field line, ζ , is normalized to l_0 , the neutral penetration depth. Perfect recycling wall is assumed at $l = 0$

$1 \gg N(0)/n_{core}$ in the crossfield case. The neutral penetration depth, however, differs between the cases only by a factor close to unity. For the Goldston and Rutherford calculation[19], $N(0)/n_{core} \approx D/2D_N \ll 1$ where D and D_N are the crossfield diffusion coefficients for the plasma and neutrals, respectively. If we take this result as a general principle and apply it to the parallel calculation, the density ratio in the parallel case should be of order unity because the plasma diffusion mechanism is exactly the same as that of the neutral in the parallel direction, namely due to the drag between the two species.

2.2.3 Finite Centrifugal Confinement

In this section, we extend the result of the above baseline case by including the gravitational confinement term. The system, for $\hat{\alpha} \gg 1$, is then governed by

$$(nu)' = Nn , \quad (2.45)$$

$$n' = -nN(u - U) + n\tilde{g} \quad (2.46)$$

$$(NU)' = -Nn , \quad (2.47)$$

$$N' = nN(u - U) , \quad (2.48)$$

where $\tilde{g} \equiv \hat{g}/\hat{\alpha} = (l_0/2)\partial_t M_s^2 = (1/2)\partial_\zeta M_s^2$. Again, with perfect recycling condition at the wall, we can simplify the system to the following three equations

$$n' + N' = n\tilde{g} , \quad (2.49)$$

$$N' = \Gamma(n + N) , \quad (2.50)$$

$$\Gamma' = nN , \quad (2.51)$$

with three unknowns n , N and $\Gamma \equiv nu$. In general, $\tilde{g} = \tilde{g}(\zeta)$ and a general solution is difficult. We thus assume for simplicity that the function \tilde{g} takes the Dirac delta functional form:

$$\tilde{g}(\zeta) = \tilde{g}_0 \delta(\zeta - \zeta_1) , \quad (2.52)$$

where \tilde{g}_0 is a constant and ζ_1 is some distance from the wall. We will assume that ζ_1 is of order unity. In MCX, ζ_1 could be of order 2 – 4. This particular form of \tilde{g} means that the rotational flow profile is a step function in which the flow change from zero to a finite size at $\zeta = \zeta_1$. This prescription for \tilde{g} introduces a discontinuity

in n but not in N and Γ . Integrations of Eq.(2.49) in the two regions separated by ζ_1 yield

$$N + n = \begin{cases} 1, & \text{for } \zeta \geq \zeta_1 \\ A_w, & \text{for } \zeta \leq \zeta_1 \end{cases}, \quad (2.53)$$

where $A_w \equiv n_w + N_w$ is a constant. Note that since n is discontinuous at ζ_1 while N is continuous, $n + N$ is double-valued at $\zeta = \zeta_1$. By differentiating Eq.(2.50), with the help of Eqs.(2.53) and (2.51), we arrive at

$$N'' = \frac{d}{dN} \frac{(N')^2}{2} = \begin{cases} N(1 - N), & \text{for } \zeta \geq \zeta_1 \\ NA_w(A_w - N), & \text{for } \zeta \leq \zeta_1 \end{cases}, \quad (2.54)$$

Integrating once with respect to N , we have

$$N' = \begin{cases} -[N^2 - (2/3)N^3 + C_>]^{1/2}, & \text{for } \zeta \geq \zeta_1 \\ -[A_w^2 N^2 - (2/3)A_w N^3 + C_<]^{1/2}, & \text{for } \zeta \leq \zeta_1 \end{cases}, \quad (2.55)$$

where $C_>$ and $C_<$ are constants and N is assumed to be monotonically decreasing from the wall. Also note that N' and N'' are discontinuous at $\zeta = \zeta_1$. For $\zeta_1 \leq \zeta$, the system and boundary conditions are identical to that of Sec.2.2.2 (the no confinement case). Thus, the solution for $\zeta_1 \leq \zeta$ can be written down immediately from Eq.(2.44) as

$$N(\zeta \geq \zeta_1) = \frac{3}{2} \operatorname{sech}^2 \left[\frac{\zeta - \zeta_1}{2} + \operatorname{sech}^{-1} \left(\frac{2N_1}{3} \right)^{1/2} \right], \quad (2.56)$$

where N_w in Eq.(2.44) has been replaced by N_1 , the undetermined neutral density at $\zeta = \zeta_1$. The solution for $\zeta \leq \zeta_1$ upon integrating Eq.(2.55) is

$$- \int_{N_w}^N \frac{dN}{[A_w^2 N^2 - (2/3)A_w N^3 + C_<]^{1/2}} = \zeta(N), \quad (2.57)$$

with the condition

$$-\int_{N_w}^{N_1} \frac{dN}{[A_w^2 N^2 - (2/3)A_w N^3 + C_{<}]^{1/2}} = \zeta_1 , \quad (2.58)$$

that must be applied so that $N(\zeta_1) = N_1$, defined earlier. Our goal now is to express $C_{<}$, N_1 and A_w in terms of N_w so that Eq.(2.58) can be used to solve for N_w . Once this is done, the system is solved.

To proceed, we need jump conditions at ζ_1 . We divide Eq.(2.49) by n , integrate both sides from $\zeta_1 - \delta$ to $\zeta_1 + \delta$, and take the limit $\delta \rightarrow 0$. These yield

$$[\ln n] = \tilde{g}_0 , \quad (2.59)$$

where $[f]$ represents the difference between the limiting values of f at $\zeta = \zeta_1$, that is $f_+ - f_-$. This relation translates to

$$n_- = n_+ e^{-\tilde{g}_0} . \quad (2.60)$$

Combining the above relation with Eq.(2.53) at $\zeta = \zeta_+, \zeta_-$, we have

$$N_1 = \frac{A_w e^{\tilde{g}_0} - 1}{e^{\tilde{g}_0} - 1} . \quad (2.61)$$

From Eq.(2.50) and Eq.(2.53), we have $N'_+ = \Gamma_1$ and $N'_- = \Gamma_1 A_w$, which gives

$$N'_- = N'_+ A_w \quad (2.62)$$

Substituting Eq.(2.55) in Eq.(2.62), we obtain

$$C_{<} = \frac{2}{3} A_w (1 - A_w) N_1^3 . \quad (2.63)$$

Now we are left with finding the relation between N_w and A_w . This can be determined by using the boundary condition at $\zeta = 0$. For example, if $n_w = 0$, we have

$A_w = N_w$ according to Eq.(2.53) and the system can be solved by using Eq.(2.61) and (2.63) in Eq.(2.58) to obtain (numerically) N_w . By probing the values of N_w with different values of \tilde{g}_0 this way, we can obtain the relation between the neutral density at wall and the strength of the centrifugal confinement on the plasma. We first do some asymptotic limits and then present the numerical solution.

2.2.4 Strong Confinement Limit

Although we cannot solve the finite confinement system analytically, an approximate solution can be obtained in the strong confinement regime, i.e. $\hat{g}_0 \gg 1$. We do this here and discuss $\hat{g}_0 \ll 1$ in the Appendix A.2. We will assume that ζ_1 is of $\mathbf{O}(1)$. The right-hand-side of Eq.(2.58) is thus of order unity. We expect $N_1 \lesssim N \lesssim N_w$; and also expect $n_w, N_w \ll 1$ (and thus $A_w \ll 1$) for $\tilde{g} \gg 1$. Thus, for this ordering, the integrand is of order N_w^{-2} , and the integral is of $\mathbf{O}(1/N_w) \gg 1$. Thus, there cannot be a balance. The only way a balance is possible is if the integral, of order $\int_{N_w}^{N_1} dN/N^2$, itself yields a smaller result, since the RHS is $\mathbf{O}(1)$. This can happen if N_1 is very close to N_w , i.e., $N_1 \approx N_w$, in which case N is approximately constant in $[0, \zeta_1]$. If we make this ansatz, we find that the integrand approximates as

$$\begin{aligned}
\left(A_w^2 N^2 - \frac{2}{3} A_w N^3 + C_{<} \right)^{-1/2} &\approx \left(A_w^2 N^2 - \frac{2}{3} A_w N^3 + \frac{2}{3} A_w N_1^3 \right)^{-1/2} \\
&= \left[A_w^2 N^2 \left(1 - \frac{2}{3} \frac{N^3 - N_1^3}{A_w N^2} \right) \right]^{-1/2} \\
&\approx (A_w N)^{-1} ,
\end{aligned} \tag{2.64}$$

where we have used $C_< \approx (2/3)A_w N_1^3$ according to Eq.(2.63). By using the above approximation in Eq.(2.57), we can perform the integral and find

$$N(\zeta \leq \zeta_1) \approx N_w e^{-A_w \zeta} . \quad (2.65)$$

Also, from Eq.(2.50) and (2.53), we have

$$N'(\zeta \leq \zeta_1) = A_w \Gamma . \quad (2.66)$$

We immediately get from the Eq.(2.65) and (2.66) that,

$$\Gamma \approx -N , \quad (2.67)$$

for $\zeta \leq \zeta_1$. Using the Bohm boundary condition, that is, $u_w = -\hat{\alpha}^{1/2}$, and Eq.(2.67), we have

$$n_w \approx \frac{N_w}{\hat{\alpha}^{1/2}} . \quad (2.68)$$

Using Eq.(2.61) at large \tilde{g}_0 limit, Eq.(2.65) at $\zeta = \zeta_1$ with $A_w \zeta_1 \ll 1$ and $A_w = N_w(1 + 1/\hat{\alpha}^{1/2})$ obtained from Eq.(2.68) and (2.53), we arrive at

$$\frac{N_w}{\hat{\alpha}^{1/2}} \approx e^{-\tilde{g}_0} - N_w^2 \zeta_1 \left(1 + \frac{1}{\hat{\alpha}^{1/2}}\right) , \quad (2.69)$$

Taking once again the approximation, $N_w \zeta_1 \ll 1$, the second term in the bracket can be ignored compared with the LHS, we obtain an quadratic equation in N_w , namely

$$\zeta_1 N_w^2 + \frac{N_w}{\hat{\alpha}^{1/2}} - e^{-\tilde{g}_0} \approx 0 . \quad (2.70)$$

For $1 \ll \hat{\alpha} e^{-\tilde{g}_0}$, we have

$$N_w \approx \frac{e^{-\tilde{g}_0/2}}{\zeta_1^{1/2}} , \quad (2.71)$$

while for the more realistic case $\hat{\alpha}e^{-\tilde{g}_0} \ll 1$, we have

$$N_w \approx \hat{\alpha}^{1/2} e^{-\tilde{g}_0} . \quad (2.72)$$

in the leading order. The scaling in Eq.(2.71) can also be obtained with the $n_w = 0$ boundary condition. Thus, we obtain N_w as exponentially decreasing with increasing \tilde{g}_0 . For $\zeta < \zeta_1$, $N \approx N_w$. The ansatz $N \approx N_w$ is checked by noting that $(N_w^3 - N_1^3)/N_w N_1^2 \approx 3(1 + 1/\hat{\alpha}^{1/2})N_w \zeta_1 \ll 1$. Eqs.(2.71) and (2.72) agree with the numerical results obtained directly from Eq.(2.49)-(2.51) (see Fig. 2.4). It can also be shown that $N_w/n_- \lesssim \hat{\alpha}^{1/2}$.

We note that in the strong confinement limit, n_w gets very small and λ_{cx} exceeds the scale of the magnetic curvature. Thus, fluid theory for neutrals fails. [The ratio of $\lambda_{cx}/(\text{scale size})$ in our units is about $(n_{core}/n_w)/\hat{\alpha}^{1/2}\zeta_1$ which is larger than unity.] In effect, the pressure term ($T\nabla_{\parallel}N$) is overestimated. However, we find N to be very flat which is what is expected from kinetic theory (see DEGAS[15]). Thus, the qualitative conclusions on $N(\zeta)$ profile are reasonable and adequate for our purposes.

2.2.5 Numerical Results

For present experiments, the MCX parameters are $u_{\theta} \approx 100$ km/s with a mirror ratio of about 7 effected on an axial scale of less than a meter. Plasma temperature is estimated to be about 30 eV. For these parameters, \tilde{g}_0 can be calculated to be ≈ 1.7 . Since \tilde{g}_0 is of order unity, we solve our equations numerically to get a reasonable comparison with experiment. Fig. 2.2 shows the plasma and neutral den-

sity profiles calculated numerically using Eqs.(2.49)-(2.51) with two different values of \tilde{g}_0 . The confinement force is defined as \tilde{g}_0 multiplied by a normalized Gaussian with width of order unity and $\zeta_1 = 10$. The solution is obtained by the commercial differential equation solver, Mathematica (Trademark)[34]. The first point to note is the decrease in N_w as confinement increases. This agrees with the notion that N_w is proportional to the ratio of the diffusion of plasma towards the wall to the diffusion of the neutrals towards the core. In this case, because of the confinement being increased, the plasma diffusion is decreased which in turn reduces N_w since the neutral diffusion stays the same. However, it is more interesting to observe that the neutral penetration length is larger in the case of stronger confinement, as the dashed curve indicate. This can be understood from our simple model: the neutral penetration scale length $l_0 = (T/M\alpha_i\alpha_{cx}n_{core}^2) \propto 1/n_{core}$ is larger for strong confinement because the effective n_{core} (that is the density to the left of the delta function) is lower by an exponential factor. In Fig. 2.3, we show the neutral drag resisting the plasma from hitting the wall for the same two confinement strengths. There is a qualitative difference between the two cases. For the stronger confinement case, there is a small bump in the neutral drag deep inside the plasma. This happens because the neutrals penetrate deeper.

In Fig. 2.4, we show the numerical and analytic asymptotic solutions for $\ln N_w$ vs \tilde{g}_0 with two different boundary conditions: (i) $n_w = 0$ and (ii) the Bohm equality, u_w equals sound speed. The numerical solutions represented by circular and triangular points are obtained by solving Eqs.(2.49)-(2.51) given that $\tilde{g}(\zeta) = \tilde{g}_0(1/2\pi)^{1/2} \exp[-(\zeta - 10)^2/2]$, with boundary conditions (i) and (ii) respectively.

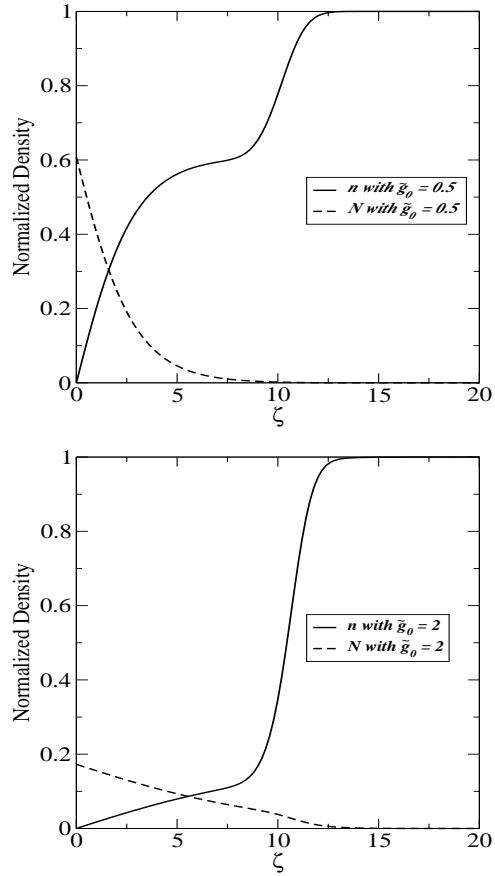


Figure 2.2: Numerical solutions of the normalized plasma and neutral densities versus parallel length for the case of centrifugal confinement. A gaussian profile is assumed for effective confinement force, centered at $\zeta = 10$. Two different strengths of confinement, \tilde{g}_0 , are shown. The penetration length for the neutrals is increased in the higher confinement case due to the decrease in plasma density around the wall.

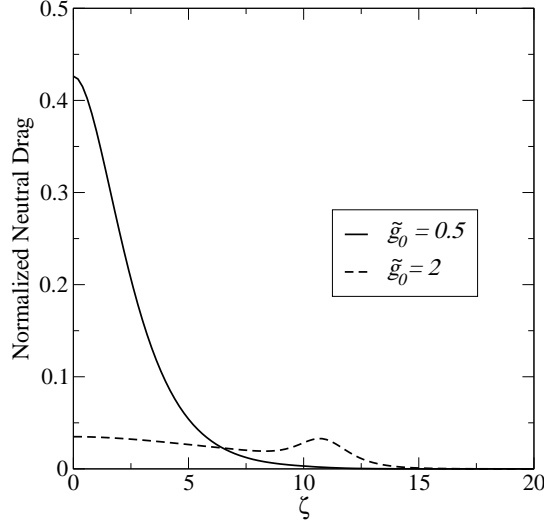


Figure 2.3: Neutral drag on the plasma, $-nN(u - U)$ for the two cases shown in Fig. 2.2. The small bump for the higher confinement case results from greater neutral penetration.

We see that the asymptotic solutions given by Eq.(2.71) (dash-line) and (2.72) (solid line) are excellent approximations to the corresponding numerical results for large \tilde{g}_0 . In any case, the N_w is decaying exponentially with \tilde{g}_0 for large \tilde{g}_0 . Here, we can also justify the use of the simplified system Eqs.(2.49)-(2.51), which is obtained under the assumption that the inertia term can be ignored. Indeed, Fig. 2.4 also shows that the numerical solution (dots) given by the “full system”, Eqs.(2.26)-(2.29), with boundary condition (ii), agrees very well with the solution given by the simplified equations (triangular points). This shows that N_w is not sensitive to the inertial terms.

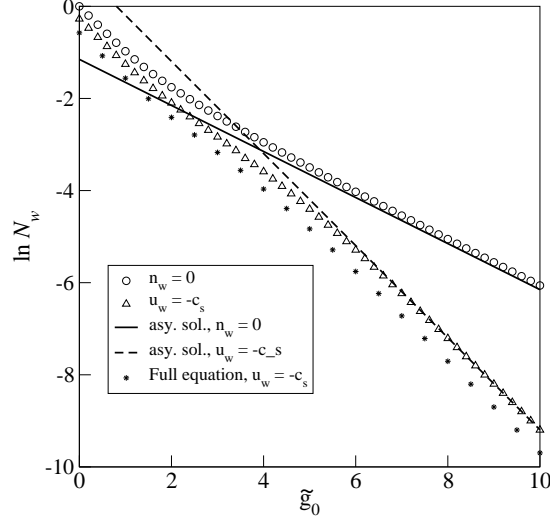


Figure 2.4: Log-linear plot for normalized neutral density vs confinement strength. The circles are the numerical solution with the $n_w = 0$ boundary condition. The triangles are for the Bohm equality boundary condition, i.e. u_w equals sound speed. Solid line and dash line are for the asymptotic solutions with the Bohm equality boundary conditions for the two different limits, $1 \ll \hat{\alpha}e^{-\tilde{g}_0}$ (which corresponds to $n_w = 0$ in the limit $\hat{\alpha} \rightarrow \infty$) and $1 \gg \hat{\alpha}e^{-\tilde{g}_0}$, respectively. The squares are for the numerical solution of the full system Eqs.(2.26)-(2.29) with Bohm equality boundary condition. Asymptotic decay rates for large \tilde{g}_0 are shown to be 0.50 and 1.0 for the two different boundary conditions respectively. Also note that decay rate for weak confinement (small \tilde{g}_0 region) has also been calculated for the $0 \leq \tilde{g}_0 \leq 0.001$ (Not shown here). The result agrees with the approximation given by Eq.(A.14).

2.3 Summary and Conclusion

Plasma-neutral interactions along the magnetic field are considered for a centrifugally confined plasma wherein a crossfield plasma rotation inhibits plasma escape along the magnetic field. Analytic and numerical solutions from a simple one-dimensional isothermal model are obtained. It is shown that for perfect recycling the neutral density at the wall is exponentially smaller than the central plasma density for strong centrifugal confinement compared to the case of no confinement for which the neutral wall density equals the central plasma density. Eqs.(2.71) and (2.72) show the exponential factors in the limits, $\hat{\alpha}e^{-\tilde{g}_0} \gg 1$ and $\hat{\alpha}e^{-\tilde{g}_0} \ll 1$, respectively, where $\hat{\alpha}$ is the ratio of the CX to ionization cross-sections and \tilde{g}_0 corresponds to $M_s^2/2$ where M_s is the sonic Mach number of the rotational speed.

The effective neutral penetration depth along the field, of the same order as the crossfield penetration depth in the zero confinement limit, increases exponentially in the strong confinement case. This penetration length increase is due to the decrease in local plasma density (and thus CX interaction) which allows more fast moving neutrals to reach the outer core. However, kinetic theory has to be used for quantitative description when plasma density becomes too small so that λ_{cx} is larger than macroscopic scales.

Our results suggest that the neutral density at the MCX insulator may be smaller or larger than the neutral density at the radial walls, depending on parameters. The neutral density at the insulator scales as $\hat{\alpha}^{1/2}e^{-M_s^2/2}n_{core}$, while crossfield neutral density scales[19] as $Dn_{core}/(2l_0^2\gamma_i)$ [using Eq.(2.4) with some algebra] where

l_0 is defined in Eq.(2.30), $\gamma_i \equiv \alpha_i n_{core}$ is the ionization rate and D is probably dominated by non-classical effects. In principle, D is the crossfield classical particle diffusion coefficient. If we use this classical result and $l_0 \approx 5\text{cm}$ for MCX, N_{\parallel} and N_{\perp} are equal if $M_s = [2 \ln(2l_0^2 \gamma_i \hat{\alpha}^{1/2} / D)]^{1/2}$. Thus, the critical $M_s \approx 4.6$ for $T = 30\text{ eV}$, $B = 0.2\text{ Tesla}$ and $n = 10^{14}\text{ cm}^{-3}$. MCX generally operates for M_s in the range 2 to 3.5. Thus, our result indicates that MCX is presently running in the high end-wall neutral density region, assuming classical diffusion. However, since D is likely to be larger, the general operation may span both the cases of high end-wall neutral density and high side-wall neutral density.

Chapter 3

Two Dimensional Simulation

In this chapter, in order to find the plasma-neutral equilibria, we will model the MCX system in two dimensions, i.e. in the (x, z) -plane. Since MCX is an azimuthally symmetric device, investigating the equilibrium states in the two non-trivial dimensions as our next step should present us with a reasonably good approximation to the real system. It should also be noted that these two dimensions are fundamentally different from the plasma physics point of view and this makes it interesting for investigation.

To motivate, assuming the case without confinement, in the parallel to B-field direction (i.e. z -direction), plasma can move in the sonic/subsonic scale. Indeed, due to the existence of the end wall (which is perpendicular to the B-field lines) which acts as a sink of plasma particles (see [16]), the plasma will hit the wall with sound speed (i.e., the Bohm criteria). As it approaches the end wall, the plasma density will drop in the l_0 length scale defined in previous chapter. In terms of momentum consideration, the recycled neutral particles will undergo charge-exchange interactions with the plasma and this is the dominant force which balances the plasma thermal outward pressure originated from the density gradient. We can also think of it as the thermal pressure balances between the plasma and neutrals. It can be seen by adding the momentum equations of the two species together. That

is exactly the reason why the neutral density at the end wall without confinement is of the same order as the plasma core density. However, for the perpendicular to B-field direction (we call it x -direction), the plasma pressure is mainly balanced by the Lorenz force $\mathbf{J} \times \mathbf{B}$, rather than the charge-exchange with the neutrals. This actually is the celebrated idea of plasma magnetic confinement. In this situation, the neutral pressure and the charge-exchange interaction is minimal (comparing with the plasma pressure). The neutral density is therefore very small.

Now let us consider the case that we have the centrifugal confinement (i.e., turn on the plasma rotation in a mirror field) and the confinement occurs somewhere away from the end wall, that is, away for a distance larger than l_0 . In the z -direction, the force balance is different. There is the centrifugal force which pulls the plasma toward the core (or away from the end wall). In the core, the plasma density increases. The main plasma gradient occurs where the confinement force is and the pressure it produces is balanced by this force, which indeed drives this gradient. However, in the region between the end wall and the confinement force effective location, the plasma density is being lowered. Now when plasma gets close to the wall, its density drops, as in the no-confinement case. However, the gradient is much smaller now. In this region, neutral thermal pressure balances with plasma pressure (because there is no other “dominant” force available). But due to the fact that the plasma gradient is being smaller, the neutral gradient should also be smaller. In turn, the neutral density at the wall need not be large to maintain such a pressure. This is exactly what Eq.(2.71) tells us. Indeed, we will show that the neutral density at the end wall drops with confinement strength, exponentially. In

the x -direction, two things changes comparing with the no-confinement case. The first being directly due to the confinement force having a x -component. However, this could be assumed to be small if $c_s \ll V_A$. The second change is that the core plasma density is increased. Due to the fact that the side wall neutrals density N_\perp is proportional to n_{core} to some power, N_\perp would also increases.

Therefore, we now come to an very interesting scenario. Without confinement, in 1D, $N_\parallel \sim n_{core}$ and $N_\perp \ll n_{core}$. What would change in 2D? Would there be any neutral “re-distribution”, because neutrals are not affected by B-field directly? Furthermore, when the confinement is on, $N_{//}$ drops (exponentially with Mach number square), n_{core} increases and thus N_\perp increases. Would $N_\perp > N_{//}$ at some point as M_s increases? What about the interaction parameter nN distribution? Would the prominent frictional dissipation region change from the end plate to the side wall? How does it change the rotational momentum confinement time scale? Before we can answer these questions, we first need to solve the two dimensional equilibrium problem numerically. Scape-off-layer[16] modeling of Tokamak devices have been studied for long[35], however, edge investigation on centrifugal confinement device is still lacking. Thus, the effort in this chapter is to attain a basic understanding of such device. Note also that instability analysis will not be considered here. Huang *et al.*[7, 36, 37, 38, 39] studied the stabilization of this system by shear flow extensively. Lehnert[40] investigated the neutral effects on the ballooning and flute modes. Tokar[41] recently described the self-sustained oscillations analytically in a plasma-wall system.

In the remainder of this chapter, we discuss our numerical model, validation of

the code and simulation results for a simplified MCX geometry.

3.1 The Numerical Model

We solve the 2D plasma-neutral system numerically with a two-fluid model by treating the neutrals as a separate fluid¹. A detailed description of the algorithm used can be found in Guzdar[44]. The governing equations are as follows:

$$\frac{\partial n}{\partial t} + \nabla \cdot (n\mathbf{u}) = \alpha_i n N - \alpha_r n^2 \quad (3.1)$$

$$\frac{\partial N}{\partial t} + \nabla \cdot (N\mathbf{U}) = -\alpha_i n N + \alpha_r n^2 \quad (3.2)$$

$$\begin{aligned} \frac{\partial (nM\mathbf{u})}{\partial t} + \nabla \cdot (nM\mathbf{u}\mathbf{u}) = & - 2T\nabla n - \nabla \left(\frac{B^2}{8\pi} \right) + \frac{\mathbf{B}}{4\pi} \cdot \nabla \mathbf{B} \\ & - \alpha_{cx} n N M (\mathbf{u} - \mathbf{U}) \\ & + (\alpha_i n N - \alpha_r n^2) M \mathbf{U} \\ & + n g \hat{\mathbf{z}} \\ & + \mu \nabla \cdot (nM\nabla \mathbf{u}) \end{aligned} \quad (3.3)$$

$$\begin{aligned} \frac{\partial (NM\mathbf{U})}{\partial t} + \nabla \cdot (NM\mathbf{U}\mathbf{U}) = & - T\nabla N + \alpha_{cx} n N M (\mathbf{u} - \mathbf{U}) \\ & + (\alpha_r n^2 - \alpha_i n N) M \mathbf{U} \\ & + \mu_N \nabla \cdot (NM\nabla \mathbf{U}) \end{aligned} \quad (3.4)$$

$$\frac{\partial \mathbf{B}}{\partial t} = \nabla \times (\mathbf{u} \times \mathbf{B}) + \frac{c^2 \eta}{4\pi} \nabla^2 \mathbf{B} , \quad (3.5)$$

where the products $\alpha_i n$, $\alpha_r n$ and $\alpha_{cx} n$ are the ionization, recombination and charge-exchange (CX) rates respectively. The term $n g \hat{\mathbf{z}}$ is a model for the centrifugal confinement force. The origin of this term is the combined effect of a mirror magnetic

¹Some researchers treat the neutral species with a diffusion model[42, 43]

field and the azimuthal rotation. Details of derivation of this term can be seen in Chapter 2. Thus, in this chapter, by adding the centrifugal confinement model term, we replace the external magnetic mirror field by an external strong B-field in z -direction. The constants μ and μ_N are the ion and neutral viscosity coefficients respectively. All the others are usual notation. The equations are now normalized. B-field is normalized to some reference B_0 , length is normalized to system width a , plasma density is normalized to some n_0 . Thus the velocity is normalized to the Alfvén speed, $V_{A,0} = (B_0^2/4M\pi n_0)^{1/2}$, time is normalized to $a/V_{A,0}$, α 's are normalized to $V_{A,0}/an_0$, μ 's are normalized to $aV_{A,0}$ and η is normalized to $4\pi aV_{A,0}/c^2$. The normalized equations are

$$\frac{\partial n}{\partial t} + \nabla \cdot (n\mathbf{u}) = \alpha_i n N - \alpha_r n^2 \quad (3.6)$$

$$\frac{\partial N}{\partial t} + \nabla \cdot (N\mathbf{U}) = -\alpha_i n N + \alpha_r n^2 \quad (3.7)$$

$$\begin{aligned} \frac{\partial (n\mathbf{u})}{\partial t} + \nabla \cdot (n\mathbf{u}\mathbf{u}) = & - 2T\nabla n + \nabla \left(\frac{B^2}{2} \right) + \mathbf{B} \cdot \nabla \mathbf{B} \\ & - \alpha_{cx} n N (\mathbf{u} - \mathbf{U}) \\ & + (\alpha_i n N - \alpha_r n^2) \mathbf{U} \\ & + ng\hat{\mathbf{z}} \\ & + \mu \nabla \cdot (n\nabla \mathbf{u}) \end{aligned} \quad (3.8)$$

$$\begin{aligned} \frac{\partial (N\mathbf{U})}{\partial t} + \nabla \cdot (N\mathbf{U}\mathbf{U}) = & - T\nabla N + \alpha_{cx} n N (\mathbf{u} - \mathbf{U}) \\ & + (\alpha_r n^2 - \alpha_i n N) \mathbf{U} \\ & + \mu_N \nabla \cdot (N\nabla \mathbf{U}) \end{aligned} \quad (3.9)$$

$$\frac{\partial \mathbf{B}}{\partial t} = \nabla \times (\mathbf{u} \times \mathbf{B}) + \eta \nabla^2 \mathbf{B} . \quad (3.10)$$

As one can note in the above equations, we limited ourselves to the isothermal assumption with the temperature of the ions, electrons and neutrals the same. In the actual simulation, we also assume α_{cx} , μ and μ_N to be constant. Spatial dependences of α_i and α_r , however, are allowed (The reason for this will be made clear when we will discuss boundary condition.) For the purpose of our present chapter, we are only interested in the equilibrium state in a two dimensional slab geometry, that is, the (x,z) -plane with y the symmetric direction. The equilibrium state is found by relaxation. We input a certain “trivial” initial condition and allow time for the numerical result to reach steady state.² The time scale for reaching equilibrium from an arbitrary initial condition is the B-flux relaxation time.

3.2 The Wall Boundary Conditions

It is necessary to specify the boundary conditions before we proceed. It is especially important for problems involving walls. We need to specify the boundary conditions for all the variables, n , N , $\mathbf{p} = n\mathbf{u}$, $\mathbf{P} = N\mathbf{U}$ and \mathbf{B} for, both the insulating end-wall and conducting side-wall.

Before proceeding to discuss the side-wall and parallel-wall boundary conditions in details, we shall explain the method we used to simulate the boundary. In the simplest case, for the cross-field boundary (side-wall), we imposed the following conducting hard-wall boundary conditions:

²Note that it is recently found by Guzdar *et al.*[45] that there is possible bifurcation when there is rotation up to certain Mach number which might explain the experimentally observed “HO-transition” [5].

Antisymmetric condition: $\mathbf{p}, \mathbf{P}, B_x$

Symmetric condition: n, N, B_z .

As we known, these boundary conditions preserve mass and magnetic flux. To conserve particles, we need antisymmetric boundary condition for \mathbf{P} also. However, imposing these hard-wall boundary conditions result in a trivial solution with flat density profiles and zero flows. From a physics point of view, a much smaller plasma density at the wall compared with the core density is expected (due to higher recombination rate at the lower temperature wall). Therefore, one could fix the boundary n to a small value to reflect this physics. This can be done by imposing boundary conditions on the other variables consistent with the asymptotic form of the cross-field components of Eqs.(3.6)-(3.10). However, it is found that doing so produces a lot of noise in the resultant simulation profiles and thus fixing n to a prescribed value is not a satisfactory condition numerically. After a series of trials and errors with different sets of boundary conditions, we finally found a way to allow a small plasma density at the wall without fixing it to a certain value by introducing a “recombination layer” (RL). We will introduce this method in the next subsection. Then, we will continue to discuss the end-wall and side-wall boundary conditions in more details.

3.2.1 The Recombination Layer: Spatial dependence of α_r

Around the material wall, we should expect a lot of recombination to occur because of its lower temperature compared with the interior plasma. We define

a recombination layer (RL) as a layer at the surface of the wall in which the recombination coefficient α_r that appears in Eqs.(3.6)-(3.9) becomes “large”. The recombination layer proposed here is a convenient and physically intuitive way of creating the necessary density gradient in the cross-field direction. In order to have a consistent picture for both the end-wall and side-wall, we also allow a similar spatial dependence on α_r for the end-wall (although for parallel dynamics an RL is not needed for numerical reasons).

There are two parameters that we need to set for the recombination layer(RL): the width and the height. In order not to interfere with the scale length of the plasma-neutral structure [i.e. l_0 in Eq.(2.30)] and other macroscopic length scale, we would like to have a small RL width relative to l_0 . On the other hand, we also want to have a numerically reasonable number of grid points which can resolve such a RL width. To establish a standard for systematic investigations, we would like to fix the width for all the simulations. We choose (RL Width) $\approx l_0/8$ to $l_0/4$. In a typical plasma device, in the core of the plasma, the value of α_r is extremely small compared with α_i or α_{cx} . Therefore, the interior value of α_r in our simulations is zero. Inside the RL, α_r starts to take off and attain a maximum at the wall. For illustration, considering only the one dimensional variation of α_r across the B-field, we have

$$\alpha_r(x) = \begin{cases} 0, & \text{for } x \leq x_{RL} \\ \alpha_{r,0} \tanh [k^2(x - x_{RL})^2], & \text{for } x_{RL} \leq x \leq x_w \end{cases} \quad (3.11)$$

where the constant k is chosen in such a way that the value of α_r just reaches a value significantly close to $\alpha_{r,0}$ at the wall (x_w) and $(x_w - x_{RL})$ is the RL width.

The remaining parameter for the RL is $\alpha_{r,0}$. It is found that simulation results do not change significantly after $\alpha_{r,0}$ increases beyond a certain level. In particular, the boundary value of n in cross-field simulation decreases with increasing $\alpha_{r,0}$ initially and roughly saturates as $\alpha_{r,0}$ increases further. This can be seen from Fig. (3.1). In practice, increasing $\alpha_{r,0}$ indefinitely would generate numerical instability, thus we choose to fix the value of $\alpha_{r,0} = 5$ as a standard value. The neutral boundary density is shown in Fig. (3.2). As a final remark for this subsection, the value of $\alpha_r(x, z)$ in two dimensional simulation is shown in Fig. (3.3).

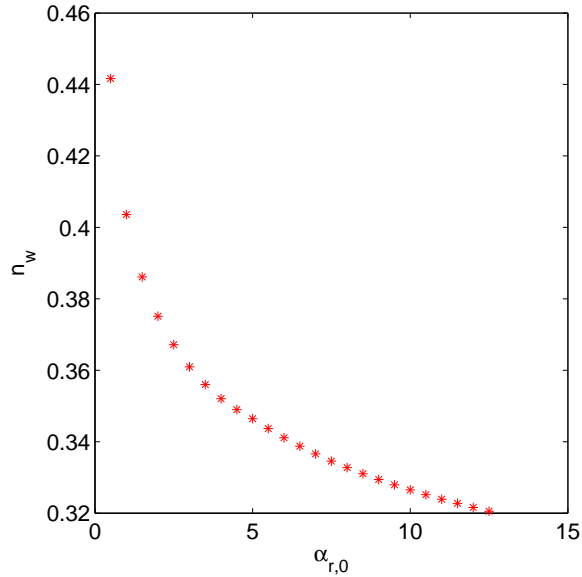


Figure 3.1: Normalized plasma boundary density, $n(x_{RL})$ vs. recombination layer strength, $\alpha_{r,0}$ in one dimensional cross-field simulation. Note that n value is chosen at x_{RL} (start of RL) rather than x_w .

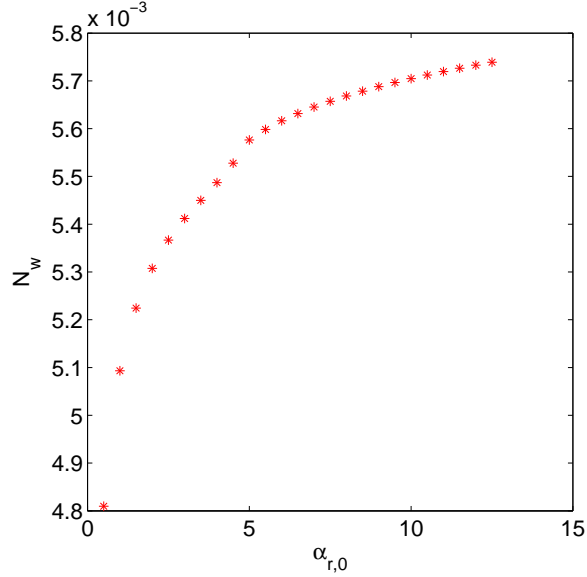


Figure 3.2: Normalized neutral boundary density, $N(x_{RL})$ vs. recombination layer strength, $\alpha_{r,0}$ in one dimensional cross-field simulation. Note that N value is chosen at x_{RL} (start of RL) rather than x_w .

3.2.2 The Insulating End-Wall

At the electrically insulating end-wall, at which the B-field is almost normal to the material surface, it is well known that the Bohm condition[16] should be used for the outward plasma flow, that is setting u_z to sound speed. (Note that we will make a little modification on this point when we introduce the recombination layer.) By specifying the flow boundary condition this way, the plasma density at the wall would be adjusted self-consistently by the system. Thus, we could extrapolate the boundary values of n from the interior points. In order to attain steady state without having particle sources, we would like to set perfect recycling condition for the outgoing plasma flux and incoming neutral flux, that is $P_z = -p_z$. Again, the neutral density is then determined self-consistently by the equations and

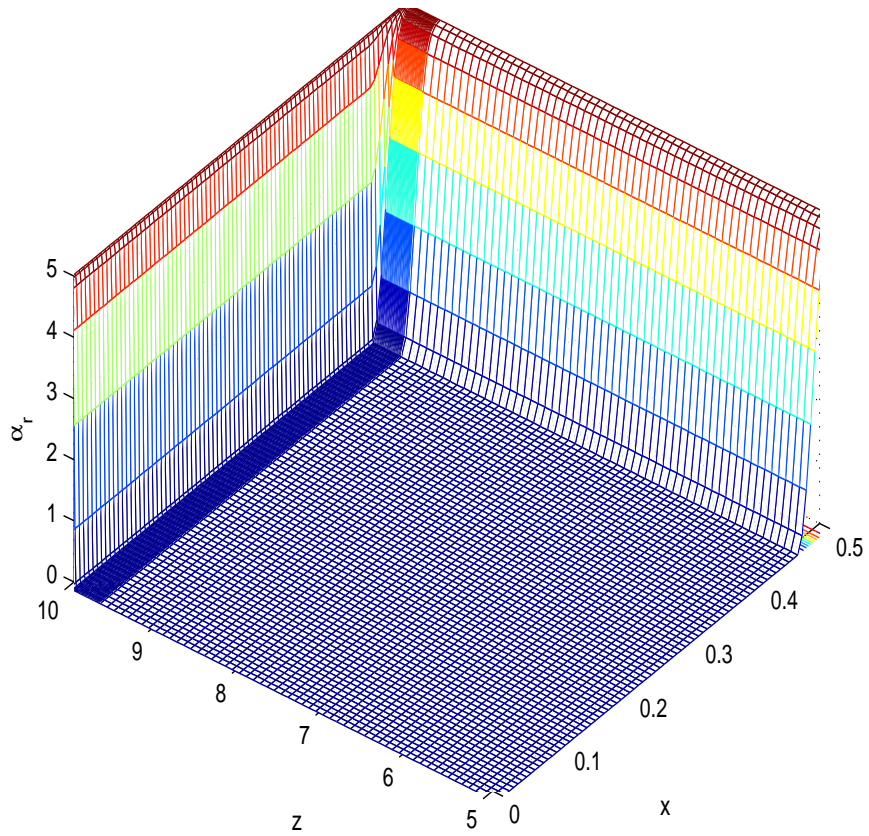


Figure 3.3: Recombination coefficient, α_r as a function of x and z . It shows the recombination layer at both of the side-wall and end-wall. Note x and z variables are not in the same scale. System size in z -direction is much longer than that in x -direction.

extrapolation is an appropriate condition. Since the normal component of the B-field is continuous for any boundary, $\partial_z B_z = 0$ is set at the end-wall. Assuming no surface current at the end-wall, B_x vanishes there. We are left with p_x and P_x at the end-wall. The usual treatment for these two variables (when the B-field is exactly normal to the wall), is to set them to be zero, that is the no-slip boundary condition. Yet, there are still other researchers who refer putting the parallel-to-surface flow to be free-slip ($\partial_z u_x = 0$) instead. Indeed, these two boundary conditions would not have any real significance in almost the entire spatial domain if the surface flow is relatively small (compared to sound speed). We decide to have free-slip for u_x but no-slip for U_x . The reasons for our choice are as follows. First, we would only consider small cross-field flow in this chapter, which is caused by the relatively small classical diffusion. As mentioned above, in this case, no-slip and free-slip boundary conditions would not give any significantly different results in almost the entire domain. Second, the boundary conditions we choose seem to be more self-consistent. It is because we have assumed that once the plasma ions hit the wall (or the sheath), they would not come back as plasma ions, but as neutral particles. Therefore, there is no way for the plasma ion to communicate the “wall information” with the plasma ions behind it through the direct plasma-plasma interactions (the viscosity term in MHD equation), which is the basis of the no-slip wall boundary condition. Thus, we think a free-slip boundary condition for the plasma is more suitable for this picture. However, the situation of the neutral particles is different. There is no reason to believe that the cross-field momentum of the plasma ion after it hits the wall would be conserved through the newly recycled neutral particle. Since the wall is fixed, a

no-slip boundary condition for the neutral particle might be more appropriate. It is to be noted that until this point, all the boundary conditions for the end-wall seem to be perfectly set. However, in order to attain consistency with the side-wall boundary we describe in the next paragraph, we will use the recombination layer as described in the last subsection. We also modify the boundary condition for u_z . We will not fix it to be sound speed, but allow it to be adjusted self-consistently and enforce the condition $u_z \leq c_s$ only. We summarize the boundary conditions at the z -wall here:

Antisymmetric condition: P_x, B_x

Symmetric condition: u_x, B_z

Extrapolation: n, N

Bohm equality condition: $p_z \leq nc_s, P_z = -p_z$

3.2.3 The Conducting Side-Wall

We now discuss the boundary condition at the conducting side-wall. Let us take a look at the cross-field component (x -component) of the induction equation Eq.(3.10),

$$\partial_x (u_x B_z) = \eta \partial_x^2 B_z. \quad (3.12)$$

It implies,

$$u_x B_z = \eta \partial_x B_z, \quad (3.13)$$

where the constant of integration vanishes because $u_{x,core} = 0$ and $\partial_x B_z|_{core} = 0$ due to symmetry. Since we expect the plasma classically diffuses outward, $u_x > 0$ for $x > x_{core} = 0$. The cross-field flow convects the B_z -flux outward with it as

can be seen from the LHS of the above equation. Since the side-wall is assumed to be perfectly conducting, no B-flux can penetrate into it. The result of the plasma diffusion is the accumulation of B_z around the side-wall and a positive x -gradient of B_z is developed. This gradient would then diffuse the B_z -flux inward to the plasma core (RHS of the above equation) and would eventually balance the outward B_z -flux brought about by the plasma flow.

There are two main components for the above scenario to work. The first is that there exists an outward flow and the second is the conducting wall that does not allow any B-flux penetration. We will discuss these cases one by one. For the flow, it is found that imposing a negative plasma density gradient ensures classical outward diffusion. It is also consistent with our intuition that the plasma density should drop as the plasma approaches the wall. The plasma density gradient can be achieved by enforcing a large ion-electron recombination rate around the boundary. That is, we will impose a recombination layer discussed in the previous subsection at the boundary. For the conducting wall condition, we set $u_x = 0$ at the boundary to prevent any loss of B_z -flux. It means that the diffusing flow is to be stopped as it reaches the boundary³

From Eq.(3.13), for $u_x = 0$, we have $\partial_x B_z = 0$. Also, to conserve particles,

³One can also prevent the loss of flux by putting a flux source at the boundary which exactly cancels the outward convecting flux, WITHOUT having to set the “hardwall” ($u_x = 0$) condition. However, simulations show that applying this automatically kills the plasma flow at the boundary. Thus, this boundary condition is almost the same as having the hardwall condition, while being more difficult to be achieved exactly.

$P_x = 0$ is set because $p_x = 0$ at the wall. Again, $B_x = 0$ because normal component of \mathbf{B} has to be continuous and there is no B-field inside a conductor. We adapt no-slip condition for u_z and U_z . To summarize the boundary condition at the side-wall, we write

$$\text{Antisymmetric condition: } \mathbf{p}, \mathbf{P}, B_x$$

$$\text{Symmetric condition: } n, N, B_z$$

A recombination layer (α_r is “large” around the wall) is also imposed.

3.3 Code Validation: One Dimensional Results Comparisons

In this section, we would like to compare the one dimensional analytical results with the numerical simulations results. This procedure serves the purpose of validating both of the analytical calculations and the numerical code. It is especially important to verify that the recombination layer boundary conditions we described in the last section are not changing the physics in the plasma core. We would then have confidence in two dimensional simulation results carried out by the code in later sections.

To be more specific, for the numerical simulation, we will do the cross-field and parallel-to-field simulations separately. That is, the simulations will also be one dimensional. This can be done by setting periodic boundary condition for the “non-interesting” direction. All other boundary conditions are the same as described in the last section. Also the factor of 2 in the plasma pressure term in Eq.(3.8) will be taken out for the purpose of this section because cold ion approximation has been taken in the analytical calculations.

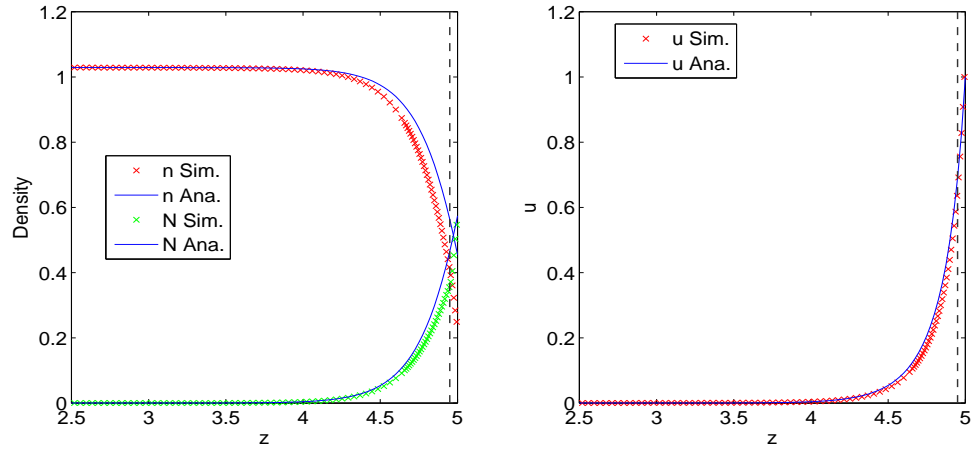


Figure 3.4: Comparisons of analytical [Sect. 2] and simulation results for the case without confinement. The left plot shows the plasma and neutral densities. The right plot shows the plasma flow. Wall is located at $z = 5$. Recombination layer starts at $z = 4.95$ (shown by vertical dash-line). In units of the numerical code, $T = 0.01$, $\alpha_i = \alpha_{cx} = 0.5$ and average of total density $\langle n + N \rangle = 1$. Neutral penetration length l_0 is about 0.2.

Fig. (3.4) shows the comparisons for parallel-to-field calculations. In the unit of the numerical code, $T = 0.01$, $\alpha_i = 0.5$, $\alpha_{cx} = 0.5$, $L_z = 2.5$ (for half space in z), the average of total particles density, i.e. $\langle n + N \rangle$ is unity. Based on these parameters, the neutral profile scale length is $l_0 = (T/M\alpha_i\alpha_{cx}n_{core}^2)^{1/2} \approx 0.2$ (note that $M = 1$ in the code units). The recombination layer width is 0.05, starting from $z = 4.95$. The left plot in Fig. (3.4) shows the plasma and neutrals densities for the analytical [see Eq.(2.44)] and the simulation results. For the analytical calculation, the only boundary condition we imposed is the Bohm equality, i.e., the plasma flow equals sound speed at the wall. By Eq.(A.2), N_w is about 0.558 when u_w equals sound speed. The first observation is that the two methods in calculating the profiles are in good agreement. The difference should be attributed to the fact that the numerical code contains more physics than that of the analytical calculation. They are the inertial terms and viscosity. The second point to note is that the neutral penetration length agrees with l_0 . The right plot of Fig. (3.4) shows that the agreement between the plasma flows calculated from the two methods is even better. Note that the flows are normalized to sound speed (and the Bohm equality boundary condition is shown explicitly.)

For the cross-field direction, due to symmetry, a half-space in x simulation suffices. Thus, the domain size is 0.5 by definition (note that length in the numerical code is normalized to the system size in the cross-field direction, a). Other physical parameters are the same as that of the parallel-to-field case. It should be noted that the system size in this direction is comparable to the “natural” neutral penetration length (≈ 0.2). However, the analytical solution Eq.(2.8), which assumes

the system size to be infinite, cannot be blindly applied here and used to compare with the simulation result. An alternative to using Eq.(2.8) is to numerical solving the Eq.(2.12), which is the origin of Eq.(2.8) without assuming infinite domain size. Therefore, shooting method is applied to Eq.(2.12) with the same domain as the numerical code. It is necessary to describe more clearly on how the boundary conditions are set for the shooting method. Eq.(2.12) is a third order nonlinear differential equation, thus we need three boundary conditions. The first two are $n_{shooting}(0) = n_{simulation}(0)$ and $n'_{shooting}(0) = 0$. The third one is to “shoot” the solution by adjusting $n''_{shooting}(0)$ such that $n_{shooting}(x_{RL}) = n_{simulation}(x_{RL})$. After solving for $n_{shooting}(x)$, we can get all the other quantities with the input constant $C = n_{simulation}(0)T + B_{simulation}(0)^2/2$ from the simulation by using Eq.(2.13)-(2.16). Fig. 3.5 shows that the plasma density profiles almost exactly match, even extending inside the RL until n reaches a very small value. Fig. (3.6) shows the N , u_x , U_x and B_z profiles. It is evident that the simulation gives very reasonable results in the interior region ($x < x_{RL}$). Whether the data points inside the RL reflect the real physics which is not considered in the simple analytical model is an interesting topic. However, we could only have a better understanding of it until we have experimental data at the vicinity of the material wall.

3.4 Simulation Results

We now turn to the two dimensional simulation results, with and without the centrifugal confinement. The numerical model is described in Sect. 3.1. The

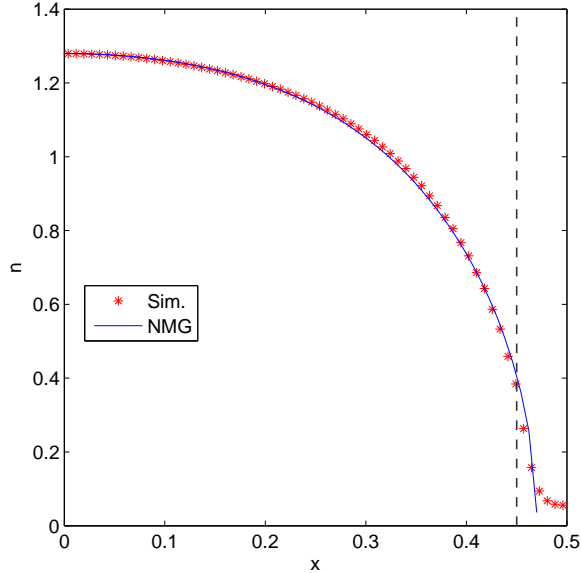


Figure 3.5: Comparison of simulation and numerical modified Goldston (NMG) calculation, Eq.(2.12) for plasma density along the crossfield direction. The NMG result is obtained by shooting method. For details see the text.

physical system to be simulated is a two dimensional slab geometry in the (x, z) -plane. The aspect ratio is chosen to emulate the aspect ratio of the MCX. Thus we have $L_z/L_x = 10$. A strong external B-field is pointing along the z -direction. As already discussed, the end-wall (at $z = 10$) is an insulator and the side-wall (at $x = 0.5$) is a conductor. Due to symmetry, simulation carried out in the half-space domain, i.e. $5 \leq z \leq 10$ and $0 \leq x \leq 0.5$, is sufficient for our purpose. Boundary conditions are described in Sect. 3.2. Parameters used are shown in Appendix F except when written explicitly otherwise.

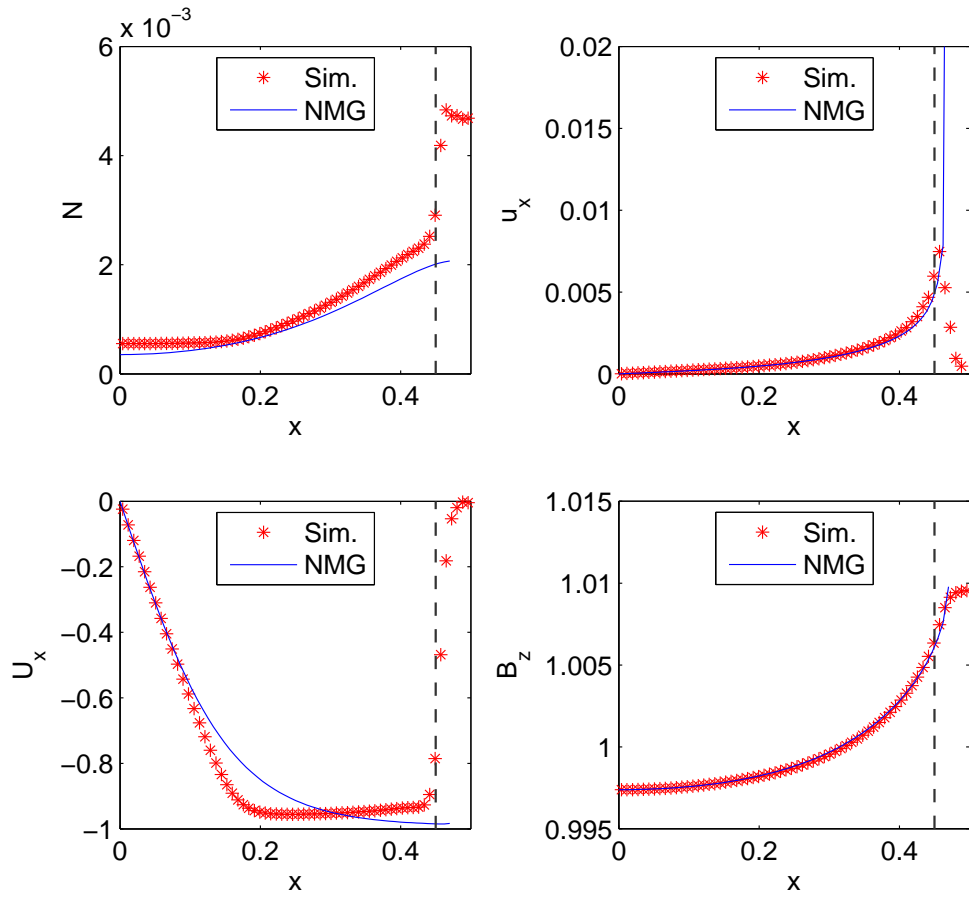


Figure 3.6: Same as Fig. 3.5, except that N , u_x , U_x and B_z are plotted.

3.4.1 Plasma neutral system without confinement

The first 2D configuration we investigate is the one without centrifugal confinement force. It is essentially a plasma-neutral system in a box, with a strong straight B-field parallel to the side-walls, connected to the end-walls. It is of interest to see whether our conjecture on the neutral “re-distribution” occurs. That is we would like to study if neutral density at the side-wall increases (and in turn the ratio N_{\perp}/N_{\parallel} increases) due to the 2D dynamics. The idea behind this re-equilibria is based on the fact that there presumably exists a neutral gradient between the two regions, and neutrals are not bounded by B-field. Thus, a neutral at the end-wall is “freely” moved to the side-wall. Yet, the neutral density at the end-wall has to be maintained to balance the plasma parallel-to-field pressure. The result is an increased neutral density at the side-wall, while the end-wall neutral density does not change much. It should be noted that while the neutral density at the side-wall increases, the change in the momentum balance in the crossfield is minimal. This is because the neutral pressure force is only a secondary force in the crossfield momentum equation and the primary competition is between the plasma and magnetic pressures.

We now test the conjecture proposed above, namely,

$$\left(\frac{N_{\perp}}{N_{\parallel}}\right)_{1D} \leq \left(\frac{N_{\perp}}{N_{\parallel}}\right)_{2D} . \quad (3.14)$$

In order to check this, we set up three simulations. They are i) 1D parallel-to-field, ii) 1D crossfield and iii) 2D simulations. The corresponding box sizes and other parameters are the same for all simulations. We then compare the two sides of the

above inequality⁴. Before showing the test result, we would like to present sample 2D simulation profiles for n and N in Figs. 3.7 and 3.8. The first observation is that the plasma density drops when approaching the walls, on a scale that agrees with l_0 (The neutral density also increases when approaching the walls in this scale). The second point to note is the difference in the neutral densities at the end- and side-walls. It is shown that without confinement, the side-wall neutral density is still much smaller than the end-wall density in 2D simulations. The third point is that the neutral density is almost one dimensional. There is a large gradient in the z -direction but very small gradient in the x -direction. Cross-sectional plots along the x -direction indeed shows a neutral density gradient, yet it is too small to be seen in the 2D profiles. All the three observations on the 2D simulation agree with the one dimensional behaviors (both crossfield and parallel-to-field) in the corresponding direction qualitatively. This reveals that separate one dimensional descriptions of the neutral densities might still be good approximation in 2D. We will come back

⁴It should be noted that in order to have a meaningful comparison of the ratios, we should show that the increase in N_{\perp} is not due to the increase in the core plasma density, n_{core} . In other words, we want to show that the increase in N_{\perp} is due to the 2D dynamics. However, since in our simulations, we fix the average total density $\langle n + N \rangle$ instead of n_{core} . n_{core} is not guaranteed to be the same in different simulations. One might think that normalizing all the neutral densities with respect to n_{core} (in each simulation) suffices. It is only true for N_{\parallel} because this is proportional to n_{core} linearly. From the last chapter, we know that N_{\perp} depends on n_{core} nonlinearly. In order to eliminate the effect of n_{core} on N_{\perp} , we examined $\tilde{N}_{\perp} = N_{\perp}/n_{core}^w$ where w is integer from 0 to 5. Results show that \tilde{N}_{\perp} is always larger in the 2D cases than that in the corresponding 1D cases. The results shown in the main text is for $w = 1$ for simplicity.

to this point when we discuss the 2D simulations with confinement.

Now let us return to the second point above. Although the side-wall neutral density is still much smaller than the end-wall density, it does increased compared with the 1D crossfield case. Fig. 3.9 shows the comparison of the neutral density ratios N_{\perp}/N_{\parallel} [the two sides of Eq.(3.14)] for various η (which controls D_{\perp}). It shows that the 2D ratios are significantly larger than the 1D ratios for all η . In particular, when η approach zero, the y -intercept of the 1D ratios almost vanishes while there is residual N_{\perp} in 2D. We attribute this residual N_{\perp} to the 2D dynamics. As final note for this section, the leftmost plot of Fig. 3.18 shows the neutral flow with $\eta = 0.005$. It can be seen that there is significant crossfield neutral flow from the end-wall to the side at about $z = 9.5$ (Note that while the velocity is being shown, because neutral density is large at end-wall, neutral flux is also significant). This gives another evidence of the 2D effect on the side-wall neutral density.

3.4.2 Plasma neutral system with various confinement strengths

In this section, we study the 2D simulation result with different confinement strengths. In other words, g in Eq.(3.7) is allowed to be non-zero. In order to model the centrifugal confinement force, we define g as a Gaussian function in z . The functional form of g is

$$g(z, x) = g_0 H(x) \exp [-(z - z_1)^2] , \quad (3.15)$$

where g_0 is a parameter indicating the confinement strength, z_1 is the mid-point between the mid-plane and the end-wall and $H(x) \equiv 1 - \alpha_r(x, z_{core})/\alpha_r(x_w, z_{core})$

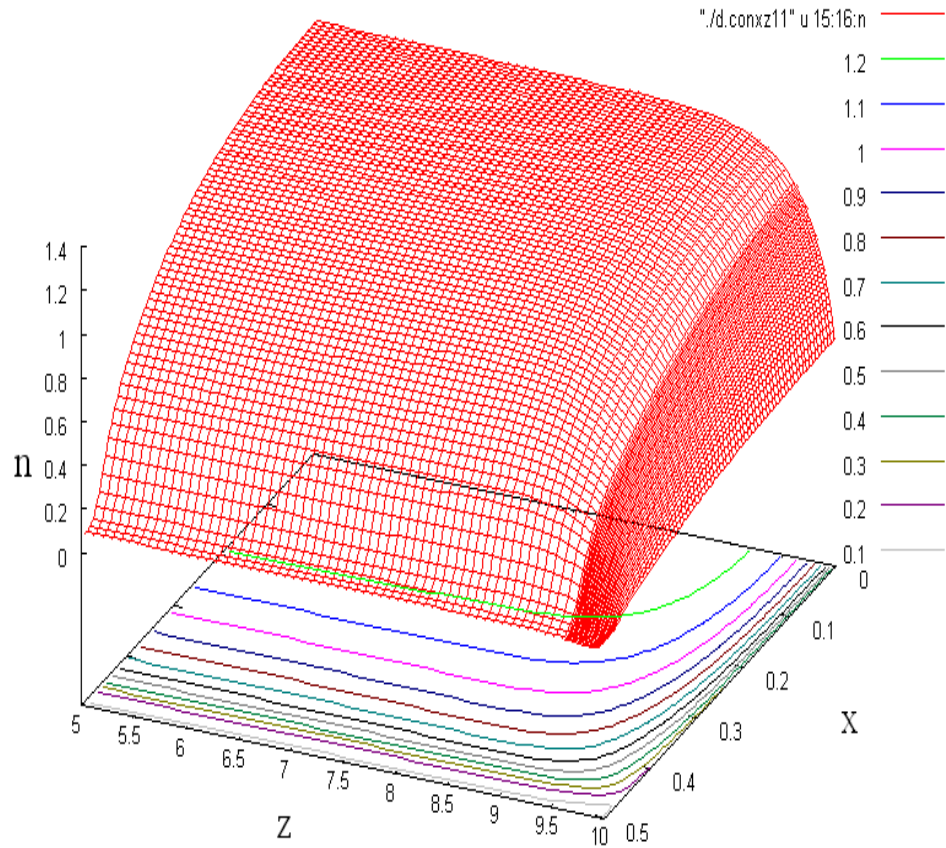


Figure 3.7: 2-D plasma density profile without confinement. x is the cross-field direction and z is the parallel to field direction. Due to symmetry in x and z directions, simulation is carried out only the half-domain of both of x and z directions. Walls are located at $z = 10$ and $x = 0.5$.

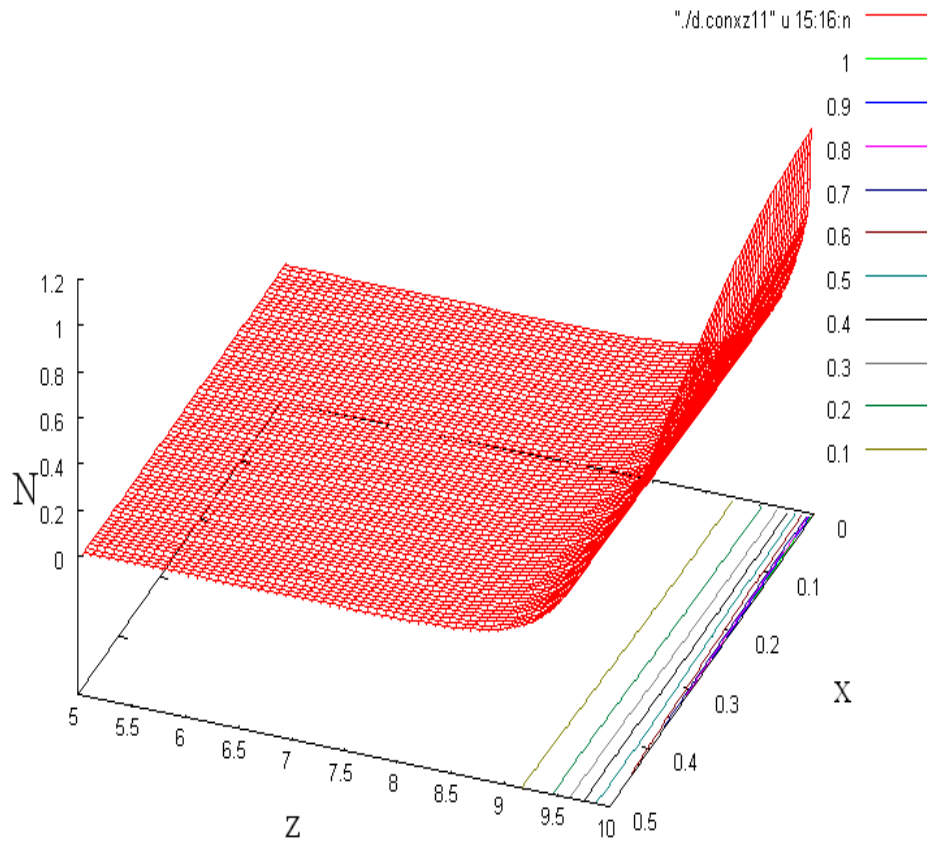


Figure 3.8: Same simulation as Fig. 3.7 but with neutral density profile plotted.

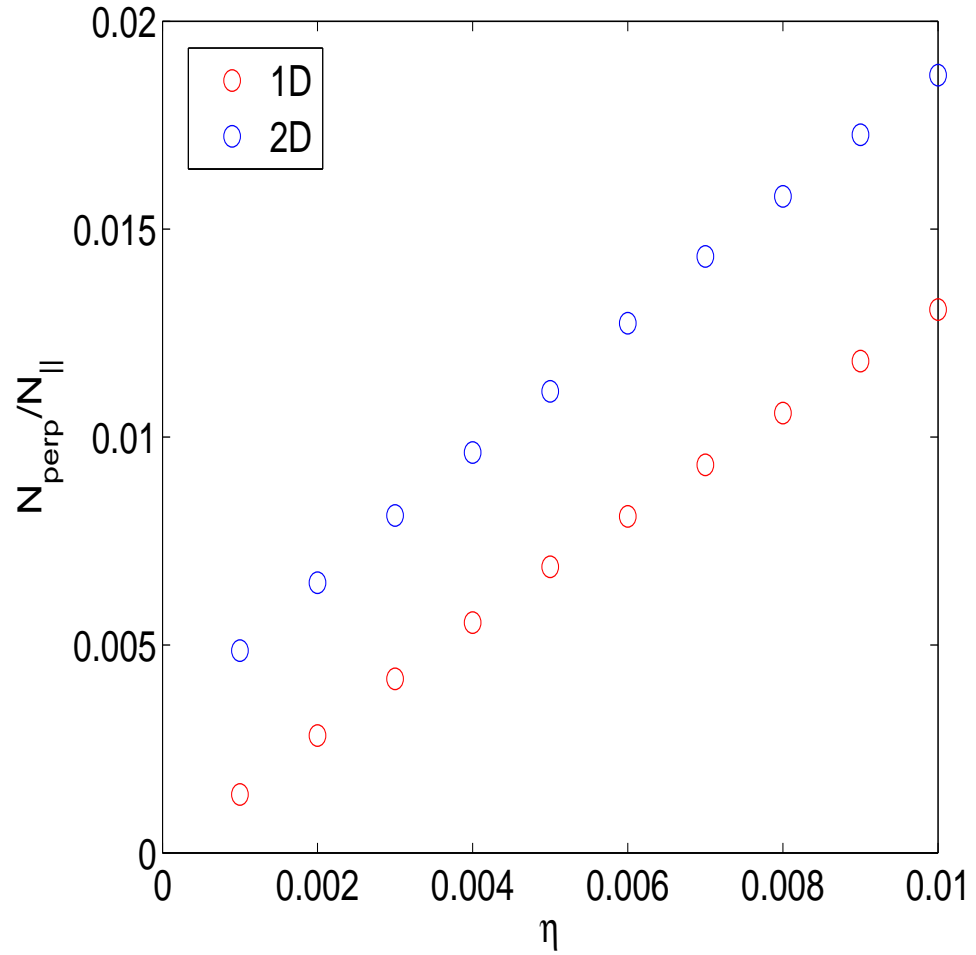


Figure 3.9: Comparison of the normalized neutral wall density ratio, N_{\perp}/N_{\parallel} , between the 2D simulation and the separated 1D results [see Eq.(3.14)]. No centrifugal confinement is applied.

takes care of the recombination layer region. This form of g gives quite a realistic model of the confinement force provided by a mirror field with azimuthal rotation. See Appendix B for details and connection between g_0 and the rotation Mach number M_s . Note also that in order to emulate the MCX mirror field curvature closely, the confinement force scale in Eq.(3.15) is set to 1. The value of g_0 in the simulations ranges from 0 to 0.16 corresponding to the rotation Mach numbers from $M_s = 0$ to about 3.7. It is found that the code starts to become unstable when $g_0 > 0.18$. Therefore, we only present the result up to $g_0 = 0.16$ (i.e. $M_s = 3.7$).

Figs. 3.10 to 3.12 show the plasma density contours for $M_s = 0, 2.7$ and 3.7 respectively. It can be seen that for these parameters, the plasma is transitioning from an unconfined to a well-confined regime. Core plasma density is also increased by about 3-fold. Figs. 3.13 to 3.15 show the corresponding neutral density contours. Three interesting points are noted. First, $N_{||,w}$ is decreased dramatically. It is expected from the 1D theory presented in Chapter 2. Second, the neutral penetration length is increased as M_s increases. As explained in Chapter 2, the decrease in plasma density around the wall region increases the “effective” neutral penetration length $l_0 = \sqrt{T/M\alpha_i\alpha_{cx}n^2}$.

Third, the side-wall neutral density is smaller than the end-wall neutral density for small M_s , but the opposite happens when M_s increases. Indeed, we could estimate the $M_{s,crit}$ at which point $N_{||,w}$ and $N_{\perp,w}$ are equal, from the 1D theory presented in Chapter 2. Appendix C shows the calculations and we found

$$M_{s,crit} = \left[2 \ln \left(\frac{3B^2}{\sqrt{\alpha_{cx}\alpha_i}\eta n_{core}^2} \right) \right]^{1/2}. \quad (3.16)$$

For the parameters that we used for the 2D simulation, $M_{s,crit}$ is found to be about 3.1 if $n_{core} = 3$ is picked (The value of n_{core} is chosen to be about what the 2D simulation shows when the transition happens). Fig. 3.16 shows the neutral wall densities, N_{\perp} and N_{\parallel} , versus M_s . It shows that the transition occurs at about $M_s = 3.6$ which is a little larger than the estimation given above but not far off. The direction of the discrepancy can be explained as follows. It should be noted that we used the cold ion assumption in 1D theory and therefore $M_{s,crit}$ is restricted by this assumption. However, in the 2D simulation, ions have the same temperature as the electrons and neutral gas. In other words, we should expect a larger loss of plasma particles and therefore a larger neutral end-wall density in the 2D simulation. In order to make the transition, a larger confinement force and thus M_s is needed in the 2D simulation⁵. We would like to make a final note of $M_{s,crit}$. If this is a good approximation even for a 2D simulation, it implies that the 2D dynamics can be largely described by the combination of the crossfield and parallel-to-field 1D calculation. It greatly enhances our understanding of the 2D system.

Figs. 3.17 and 3.18 show the vector plots of the plasma and neutral flows (\mathbf{u} and \mathbf{U}) at different values of M_s . For the plasma flow, it does not seem to be a lot different for the different confinement cases. The only change is the flow hitting the wall decreases. The reason is that we have set $u_z \leq c_s$ and the flow is created by the recombination layer. When there is lesser outflow tendency because of higher confinement, the flow speed decrease is expected. The neutral flow vector

⁵One might adjust $M_{s,crit}$ by multiplying it by $\sqrt{2}$ as $c_s \propto \sqrt{T}$. It gives $M'_{s,crit} = 4.4$ and there the 2D simulation result is bounded by these two estimation.

plots show that, as mentioned earlier, when there is no confinement (left-most plot in Fig. 3.17), a significant neutral side-ward neutral flow is seen. However, it is interesting to see that this side-ward flow becomes smaller as confinement increases (middle and right-most plots in Fig. 3.17). This can be explained by the fact that as confinement increases, the neutral gradient between the end-wall and side-wall regions decreases. In that case, smaller and smaller neutral flow is required to balanced the pressure gradient. Another point to note is the increased neutral flow inward across the B-field in the lower region for the higher confinement cases. It is another way to see the the neutral side-wall density is increased as M_s increases.

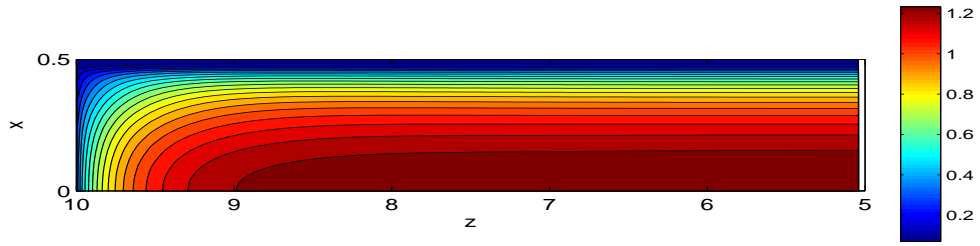


Figure 3.10: Plasma density for $M_s = 0$

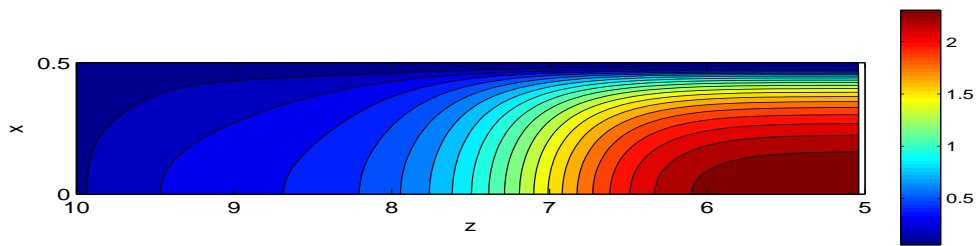


Figure 3.11: Plasma density for $M_s = 2.7$

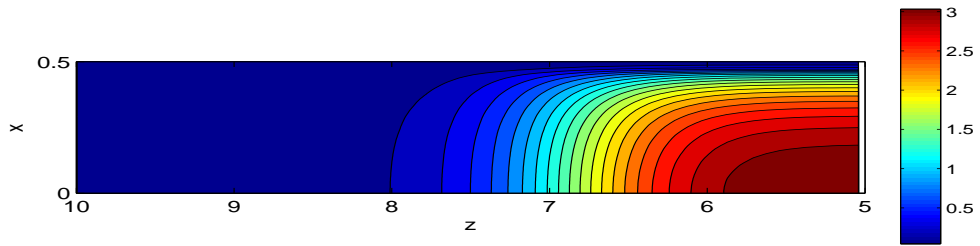


Figure 3.12: Plasma density for $M_s = 3.7$

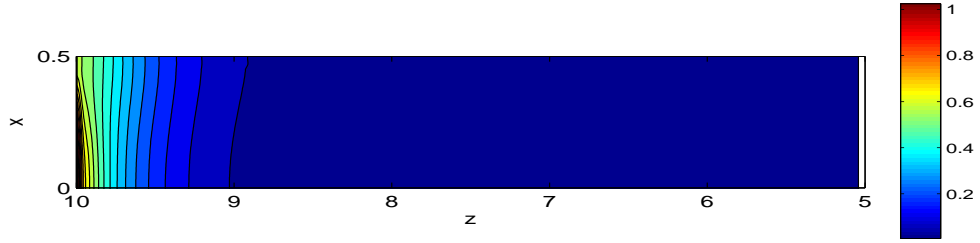


Figure 3.13: Neutral density for $M_s = 0$

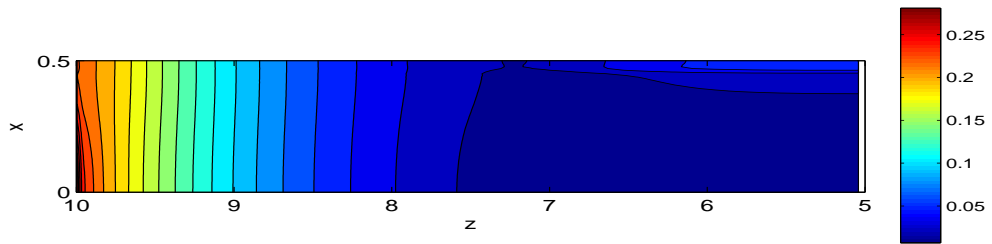


Figure 3.14: Neutral density for $M_s = 2.7$

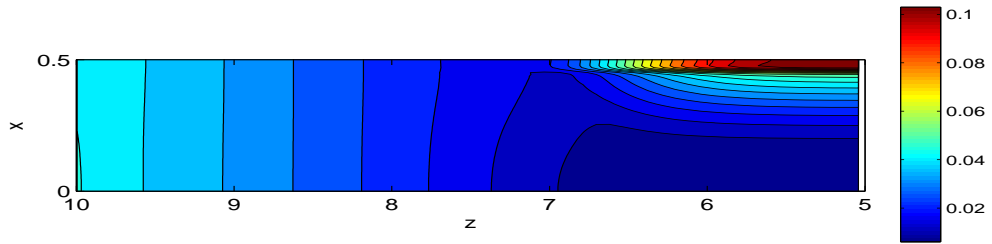


Figure 3.15: Neutral density for $M_s = 3.7$

3.5 Experimental Implication

An important quantity in our model is the product nN , which might be useful in experimental measurement. This is the interaction parameter in our model.

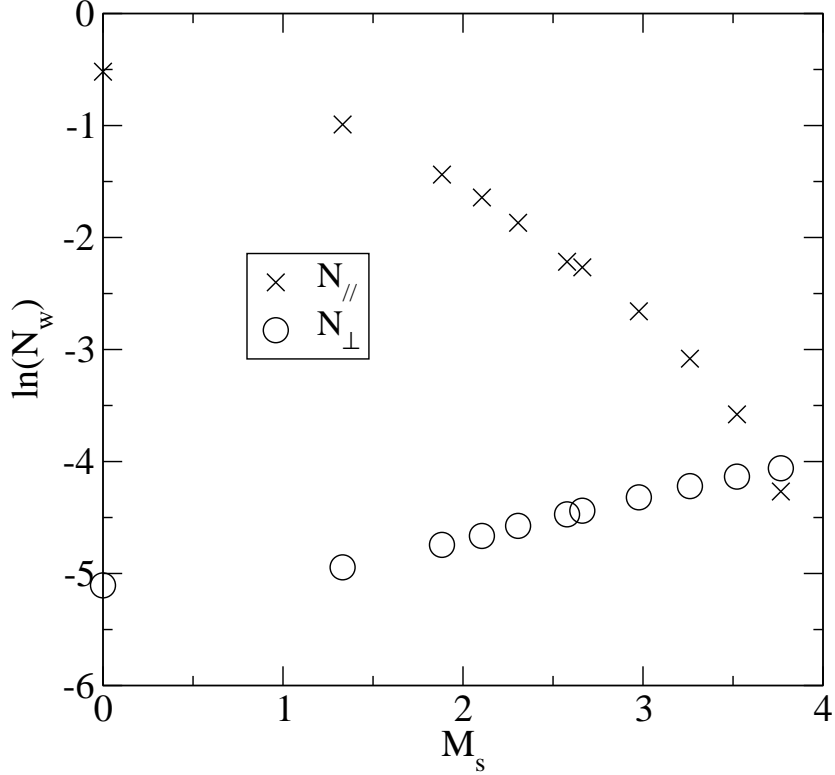


Figure 3.16: Plots of neutral wall densities, $N_{//}$ and N_{\perp} , which are measured at (x_{core}, z_{RL}) and (x_{RL}, z_{core}) respectively, versus confinement strength (i.e. modeled rotational Mach number). Confinement is imposed through an additional ng -term defined by the gaussian function $g(z, x) = g_0 H(x) \exp[-(z - z_1)^2]$, to the momentum equation in z -direction, where $H(x) \equiv 1 - \alpha_r(x, z_{core})/\alpha_r(x_w, z_{core})$, z_1 is midpoint between the mid-plane and end-wall. The Mach number can be converted from g_0 by using Eq.(B.8). We have used $T = 0.04$, $\alpha_i = 0.5$ and $\alpha_{cx} = 0.5$.

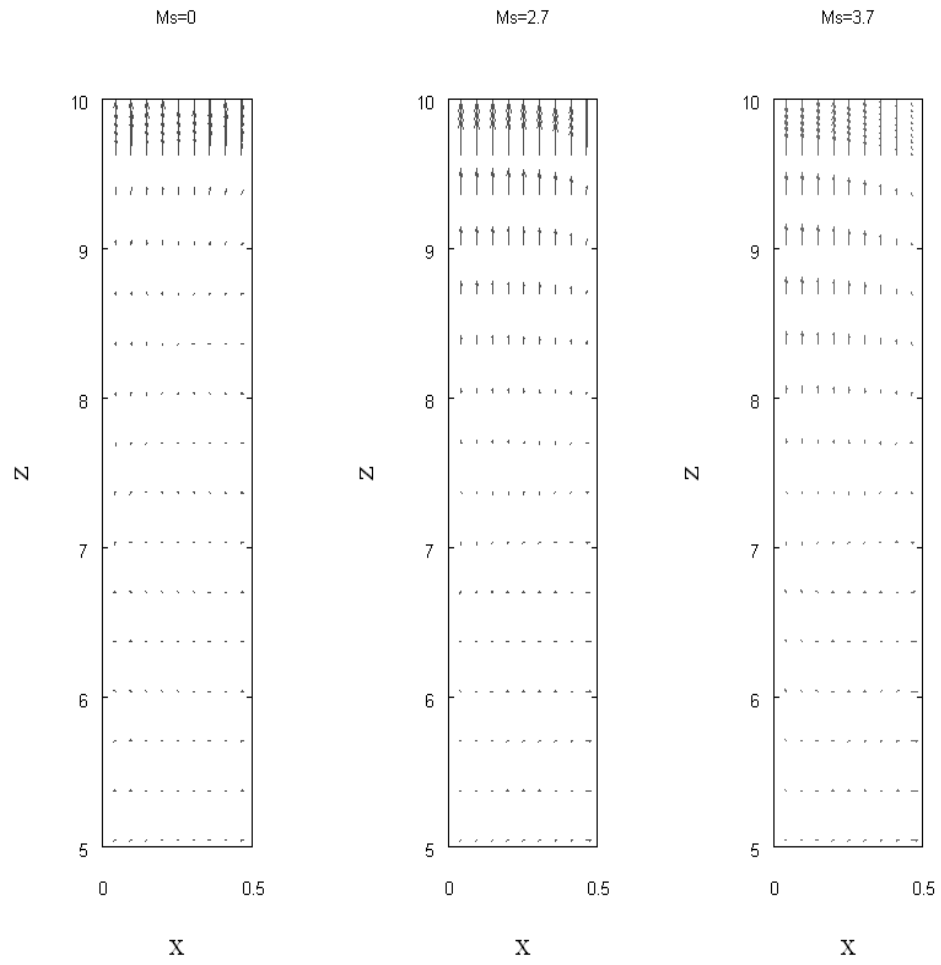


Figure 3.17: Vector plots of plasma flow for different confinement strengths. Left: $M_s = 0$, Middle: $M_s = 2.7$, Right: $M_s = 3.7$

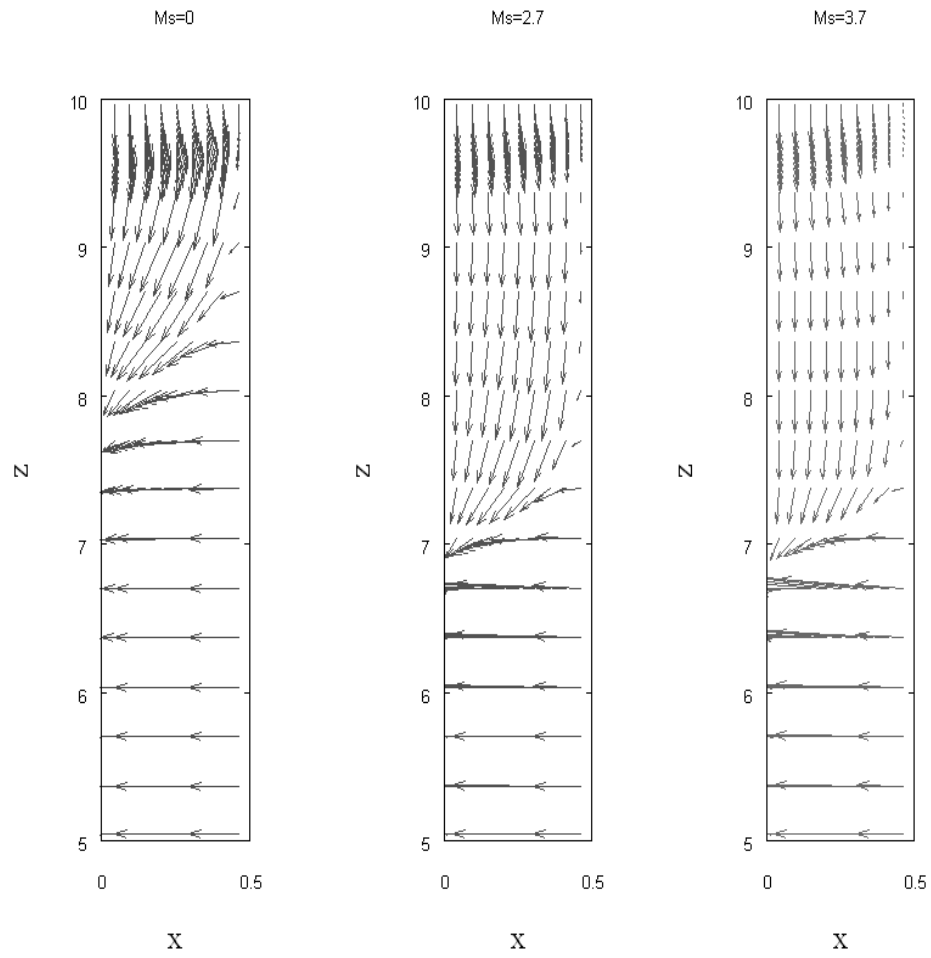


Figure 3.18: Vector plots of neutral flow for different confinement strengths. Left: $M_s = 0$, Middle: $M_s = 2.7$, Right: $M_s = 3.7$

It indicates the strength of ionization and CX (also recombination) interactions. Therefore, ionization measurements (e.g. through radiation measurement) might be affected by this parameters greatly. Figs. 3.19-3.21 show the contour plots of the interaction parameters for different values of M_s . It shows that the dominant interaction region shifts from the end-wall to the side-wall as confinement get better. Fig. 3.22 shows the values of the interaction parameters at the end-wall $n_{||,w}N_{||,w}$ and side-wall $n_{\perp,w}N_{\perp,w}$ versus M_s . It is shown that the dominant interaction region transition (from the end-wall to the side-wall) occurs at $M_s \approx 2.8$. If nN is really a good parameters for the ionization rate, we should expect some signature in the experimental measurements.

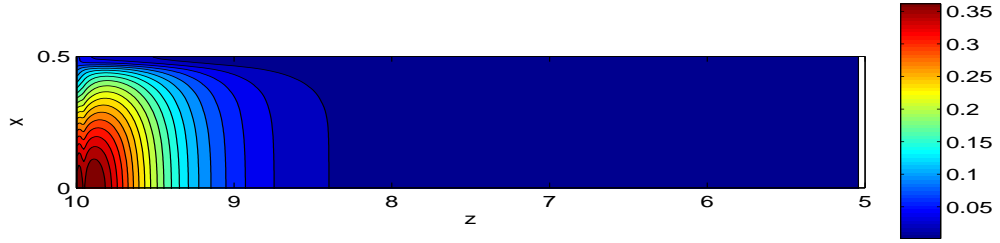


Figure 3.19: Interaction parameters nN for $M_s = 0$

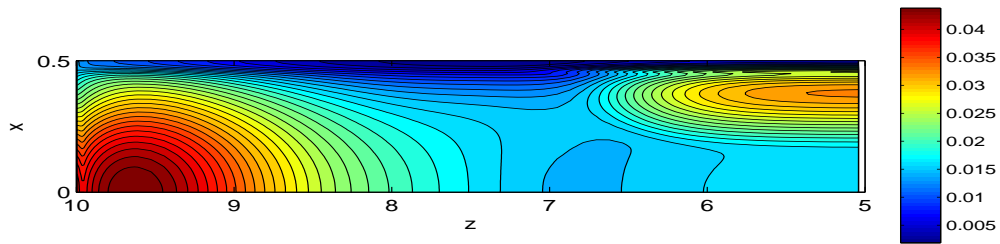


Figure 3.20: Interaction parameters nN for $M_s = 2.7$

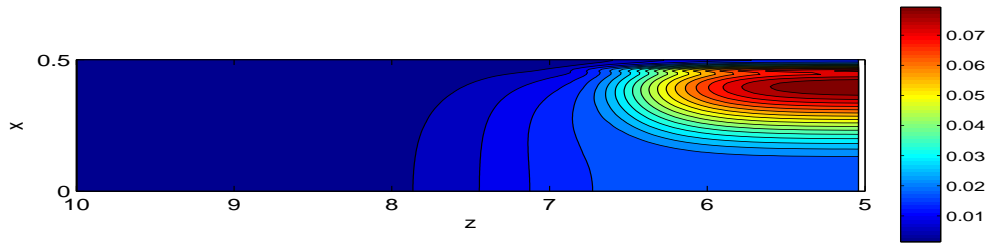


Figure 3.21: Interaction parameters nN for $M_s = 3.7$

3.6 Conclusion

We have extended an existing plasma MHD code to a 2D isothermal plasma-neutral fluid code. It is used to study the centrifugally confined plasma, in particular

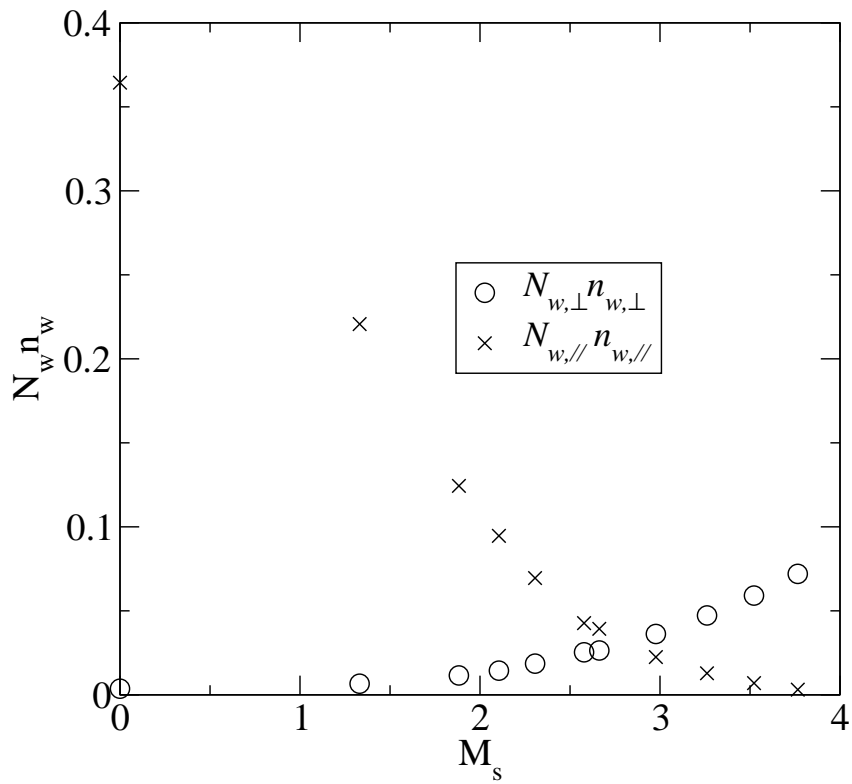


Figure 3.22: Plots of the interaction parameter nN at the center of the side and end walls versus confinement strengths. Simulation details are the same as Fig. (3.16).

MCX. A reasonable artificial force term in the plasma momentum equation is used to model the confinement force. Boundary conditions are carefully taken care of and well tested, to deal with the wall boundaries. Close to realistic parameters are used. Result shows that neutral density “re-distribution” occurs significantly when confinement is weak. Simulation also shows that within realistic operation range of MCX, neutral wall-density could be higher in the end-wall or in the side-wall, depending on M_s . Transition between high and low end-wall neutral density regime is occurs for M_s at about 3.7. It is observed that even in 2D configuration, the system behaves as if it is a semi-1D system. One may conclude that parallel-to-field and crossfield balances are only related directly through the core plasma density level. This can be seen from the fact that the $M_{s,crit}$ estimated using 1D results is not far off from the 2D calculation (considering the fact that cold ion approximation is used in the 1D calculations). However, it must be noted that this decoupling may be linked with the simple slab geometry that we are using. In real MCX geometry, 2D dynamics should play a bigger role. Yet, if our model is a good approximation, the interaction parameter nN should be a good indication of ionization/CX rate. Therefore, comparisons with experimental measurements on such rates should greatly benefit both the code improvement and experimental understanding.

Chapter 4

Hartmann Physics in Centrifugally Confined Plasma

In the previous two chapters, we have developed a simple theory and a two-dimensional numerical code for studying the neutral and plasma interaction in MCX. In particular, we obtained the neutral distribution. However, in these calculations, there is no real azimuthal flow which is the basic ingredient for centrifugal confinement. Rather, we modeled the centrifugal confinement by a gravity-like force along the B-field. As we have pointed out, this provides a qualitative understanding of the system. However, the MCX mirror field shape is different from the slab geometry we have assumed. Detailed difference in the flow pattern is expected. We therefore would like to simulate the MCX system with mirror field geometry and the azimuthal flow implemented. This also allows a better estimation of the momentum confinement time. However, it turns out that we need to have a better understanding of the Hartmann problem[18] before proceeding to direct simulation of the MCX with azimuthal flow.

The Hartmann problem is the problem of magnetized flow past a material surface with B-field lines cutting the surface (see Jackson[46]). There is an incompatibility between the frozen-in theorem and no-slip or conducting wall boundary conditions in this problem. The classical Hartmann results suggest that it would be very difficult to drive the MCX azimuthal flow, as has been pointed out by

Huang[47]. Also in the classical Hartmann solution, very thin boundary layers in the u_θ and B_θ profiles exist around the wall. To straighten this out numerically in the MCX regime is very difficult because multiple length scales are involved. Therefore, a simple analysis of the nature of the Hartmann problem is required before proceeding. This chapter extends the basic studies started by Huang[47]. In particular, it reports on the importance of the Hall effect on Hartmann flow.

In general, the viscosity on a plasma fluid has spatial dependence, which might due to the variation of plasma and neutral densities. More explicitly, we take MCX as an example. Fig. 4.1 shows the dominant azimuthal flow in MCX. This rotational flow is across the strong external mirror B-field which ends at the insulating end-wall. If μ is large only around the side-wall, the core rotation would only be affected through fluid collision drag. However, if μ is large at the end-wall instead, the core crossfield flow would be hindered by both of the fluid collision drag and the magnetic field line strength, in a combined manner¹. Hartmann was the first to describe this later mechanism in 1937[18] when he studied liquid metal flow across magnetic field. After that, different geometries and boundary conditions system were studied. In particular, two dimensional boundary layer analysis of rectangular channel flow was studied by Hunt[51]. Wilhelm and Hong[52] solved analytically a cylindrical plasma system with azimuthal flow. For numerical study of a MCX-related circular annulus channel flow, see Huang[47].

¹There is another concern called Alfvén ionization[48] for the limitation of flow in plasma. However, this is out of our scope. Interested reader may consult Lehnert’s paper[49] and recent MCX experimental results[50].

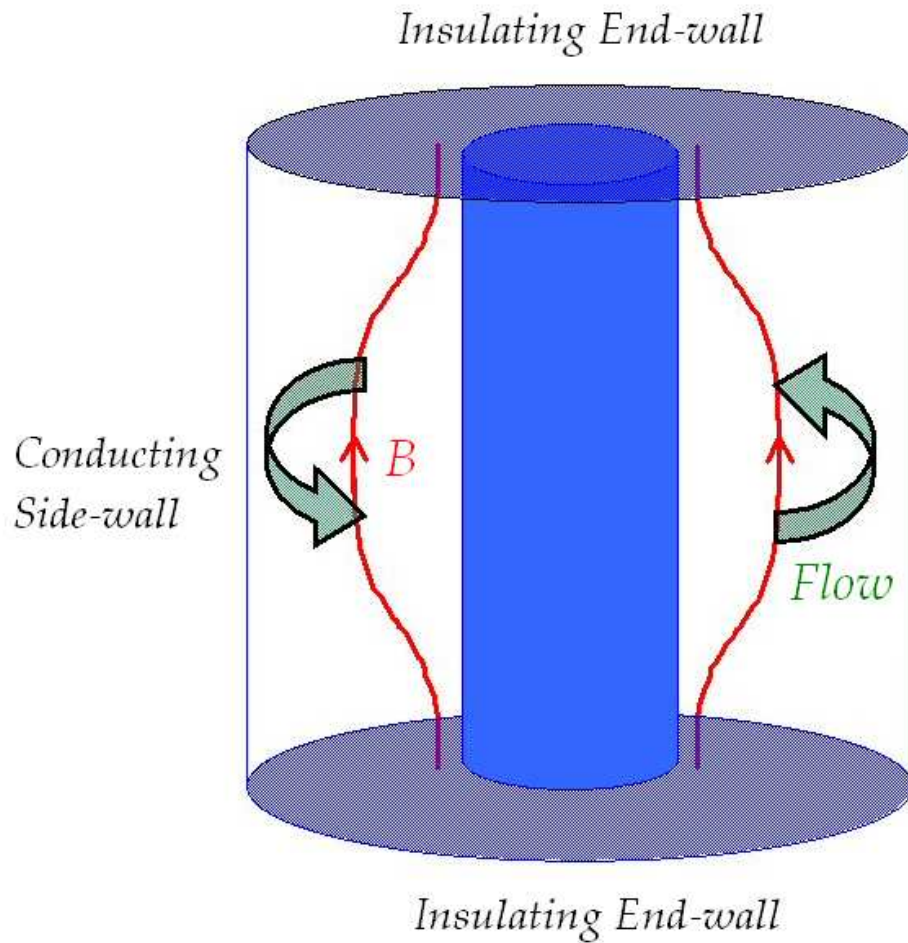


Figure 4.1: In MCX, the dominant azimuthal rotation across the strong external field which ends at the insulating end-plate. Hartmann physics is a therefore a concern.

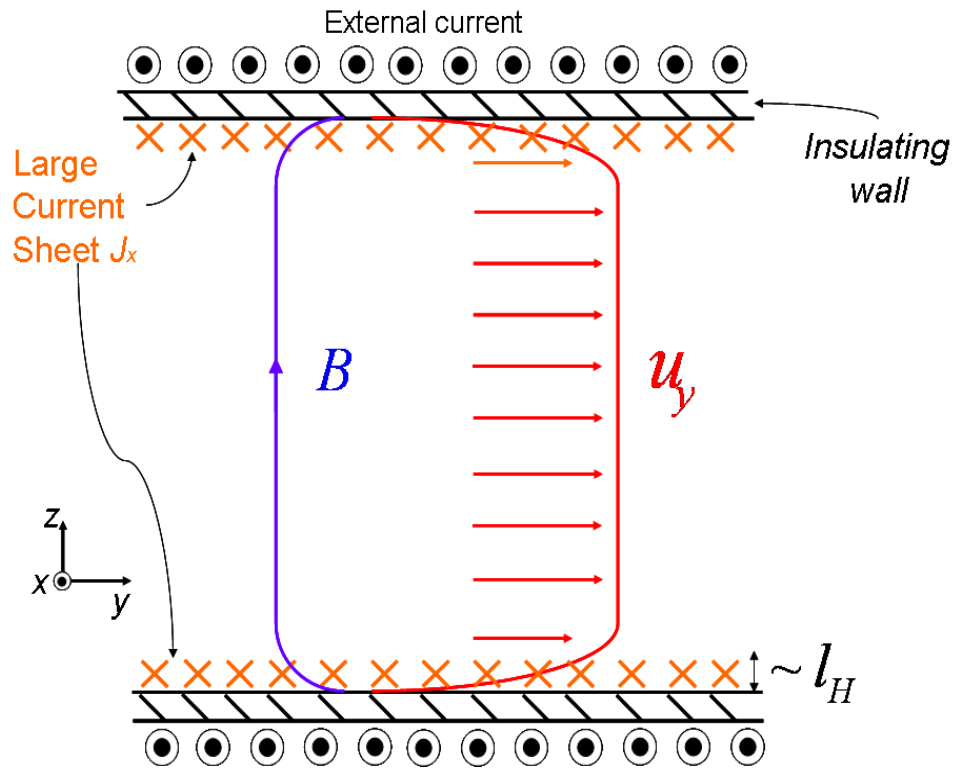


Figure 4.2: A one dimensional classical Hartmann flow of a liquid metal between insulating plates. In this example, current in the (negative) x -direction is used to drive the flow in y -direction across a strong external B -field in the z -direction.

However, care has to be taken when applying the original Hartmann solution to a fusion grade plasma instead of liquid metal. There are three main reasons for the concern in the original Hartmann assumptions. First, the no-slip flow boundary condition assumption is not clearly known for a plasma. Second, the assumption of constant viscosity is questionable for a plasma, in particular in the wall boundary region. Third, resistivity but not Hall physics was considered in the original problem.

For the first point, we think that if plasma-neutral interaction is large around the wall, no-slip condition for the plasma is also arguably reasonable when no-slip condition is applied to the neutrals. Thus, we would also take the no-slip condition throughout this chapter. For the second point, we will point out in Appendix D that the variation in the viscosity, for example due to change in plasma density, should not be overlooked in discussing boundary flow problem. The main discussion of this chapter will focus on the third point. In the following section, we would like to review the classical Hartmann in the simplest possible geometry. That is a one-dimensional system (variation in z) in which a net total current in the x -direction drives a plasma flow in the y -direction across an strong external B-field in the z -direction between two insulating plates extending infinitely in the (x, y) -plane (see Fig. 4.2). (For two dimensional channel geometries in liquid metal applications see [53]). Then we will add the Hall physics to this problem and solve it analytically. We will see how the Hall effect could help to increase the momentum confinement time.

4.1 Classical Hartmann Problem Review

4.1.1 Flow Across a Homogeneous Magnetic Field and the Solution

In this section, we review the classical Hartmann problem. It suffices to illustrate the Hartmann physics in a simple geometry. In this geometry, both x and y are symmetric directions, that is variables are only dependent on z and we will look for steady state solution with flow in y direction only. The flow is driven by external current in the x direction (For a similar calculation using mechanical force in the y -direction to drive the flow, see Jackson[46]. The scaling of the results are the same in both cases.) The liquid metal is bounded by two insulating walls (infinitely extended in (x, y) -plane) located at $z = -L/2, L/2$. The system is assumed symmetric about $z = 0$. A strong external B-field is applied along z . Flows are no-slip at the boundaries. The fluid is assumed to be incompressible. With resistivity and viscosity, the system follows, in steady state,

$$\nabla p = \frac{1}{c} \mathbf{J} \times \mathbf{B} + \mu \nabla^2 \mathbf{u} \quad (4.1)$$

$$\nabla \times \mathbf{E} = 0 \quad (4.2)$$

$$\mathbf{E} = -\frac{1}{c} \mathbf{u} \times \mathbf{B} + \eta \mathbf{J} \quad (4.3)$$

$$\mathbf{J} = \frac{c}{4\pi} \nabla \times \mathbf{B} \quad (4.4)$$

$$\nabla \cdot \mathbf{B} = 0 \quad (4.5)$$

where the inertial term in Eq.(4.1) vanishes because the flow direction (y) is symmetrical. From Eq.(4.5) and the fact that $\partial_x = \partial_y = 0$, we have

$$B_z = B_0, \quad (4.6)$$

From Eq.(4.4), we have

$$\mathbf{J} = -\frac{c}{4\pi} (B'_y \hat{x} - B'_x \hat{y}) , \quad (4.7)$$

where the prime denotes derivative respect to z . Taking $\hat{y} \cdot \nabla \times$ (4.3) and using Eq.(4.2) and (4.7), we have

$$B_0 u'_y = -\frac{\eta c^2}{4\pi} B''_y . \quad (4.8)$$

Now taking the y component of Eq.(4.1), we have

$$\frac{B_0}{4\pi} B'_y = -\mu u''_y . \quad (4.9)$$

Now Eqs.(4.8) and (4.9) form a system of equations for the two unknowns u_y and B_y . From Eq.(4.7), we have $J_z = 0$. Since we are looking for $u_x = 0$ solution, the x component of Eq.(4.1) gives $J_y = 0$ and thus Eq.(4.7) gives $B'_x = 0$. Since $B_x(0) = 0$ due to symmetry, $B_x = 0$ everywhere. Also, Eq.(4.3) shows that the E-field only has an x component. However, with Eq.(4.2), we know that E_x must be a constant. To summarize, the only non-vanishing quantities are $u_y(z)$, $B_y(z)$, $J_x(z)$, $E_x = E_0$ and $B_z = B_0$. Eq.(4.8) and (4.9) determine u_y and B_y and then J_x can be determined by Eq.(4.7). $E_x = E_0$ is determined by the x -component of Eq.(4.3), namely,

$$E_0 = E_x = -\frac{1}{c} u_y B_z + \eta J_x , \quad (4.10)$$

while $B_z = B_0$ is a parameter of the system.

Eq.(4.7) gives $J_x = -(c/4\pi)B'_y$ with $B_x = 0$ shown before. Consider the total

force density in the y -direction given by the integral,

$$\begin{aligned}
-\int_{-L/2}^{L/2} \frac{1}{c} J_x B_0 \hat{y} dz &= -\frac{2B_0}{c} \int_0^{L/2} J_x dz \hat{y} \\
&= \frac{B_0}{2\pi} [B_y(L/2) - B_y(0)] \hat{y} \\
&= \frac{B_0}{2\pi} B_y(L/2) \hat{y} ,
\end{aligned} \tag{4.11}$$

where the first and third equalities are due to symmetry about $z = 0$. It shows that the boundary condition on B_y determines the driving force for the flow (as well as the total current in the x -direction) in the system². Before proceeding, we would like to normalize the equations. B-field is normalized to B_0 , length is normalized to L , flow is normalized to $V_a = B_0^2/4\pi n_0 M$, where $n_0 M$ is the mass density of the liquid, J is normalized to $cB_0/4\pi L$, E is normalized to $V_a B_0/c$, η is normalized to $4\pi L V_a/c^2$ and μ is normalized to $n_0 M L V_a$. The normalized equations are

$$u'_y = -\eta B''_y \tag{4.12}$$

$$B'_y = -\mu u''_y \tag{4.13}$$

$$J_x = -B'_y \tag{4.14}$$

$$E_x = -u_y + \eta J_x \tag{4.15}$$

where the prime denote derivative respective to $\zeta \equiv z/L$. The only two free parameters are η and μ . We impose the following boundary conditions:

$$B_y(\pm\frac{1}{2}) = \pm K \tag{4.16}$$

$$u_y(\pm\frac{1}{2}) = 0 ,$$

²Note that we could have a mechanical force term F_y added to the momentum equation, Eq.(4.1), to drive the flow and specify $B_y(L) = 0$. However, we would like to make an analog with MCX's driving mechanism, in which the total driving current is non-zero, specifying a non-zero $B_y(L)$ is more suitable in this chapter.

where K is a constant indicating the strength of the driving (surface) current. (We could have set $K = 1$ because the equations are linear, but we would like to emphasize that K is much smaller than unity (i.e. $B_y \ll B_0$) in most applications.) Note also that the system is assumed to be symmetric about $z = 0$. Solution can be easily obtained for u_y and B_y from Eq.(4.12) and (4.13),

$$\begin{aligned} B_y(\zeta) &= K \frac{\sinh(H_a \zeta)}{\sinh(H_a/2)} \\ u_y(\zeta) &= K \sqrt{\frac{\eta}{\mu}} \frac{\cosh(H_a/2) - \cosh(H_a \zeta)}{\sinh(H_a/2)}, \end{aligned} \quad (4.17)$$

where $H_a \equiv 1/\sqrt{\mu\eta}$ (In dimensional unit $H_a = \sqrt{B_0^2 L^2 / \mu\eta c^2}$, yet H_a is still dimensionless.) is the Hartmann number. The solution for J_x and E_x follows:

$$\begin{aligned} J_x(\zeta) &= -K H_a \frac{\cosh(H_a \zeta)}{\sinh(H_a/2)} \\ E_x &= -K \sqrt{\frac{\eta}{\mu}} \coth(H_a/2) \end{aligned} \quad (4.18)$$

Fig. 4.3 show the classical Hartmann solution for B_y/K , u_y/K and J_x/K along ζ . Parameters used are $\eta = 0.01$, $\mu = 0.04$ and thus $H_a = 50$.

4.1.2 Observations and Implications

There are several points to note on the analytic solution given in Eq.(4.17) and (4.18). First, the Hartmann number is typically very large in a plasma device due to the largeness of B_0 and smallness of μ and η , for example, for MCX, H_a is of the order of 10^4 . Second, very thin boundary layers exist. It is explicitly shown in Fig. 4.3. They are called Hartmann layers and its width can be deduced from the analytic solution as $1/H_a = \sqrt{\eta\mu}$. Next, the maximum flow occurs at $\zeta = 0$ as

$$u_{y,max} \approx K \sqrt{\frac{\eta}{\mu}}, \quad (4.19)$$

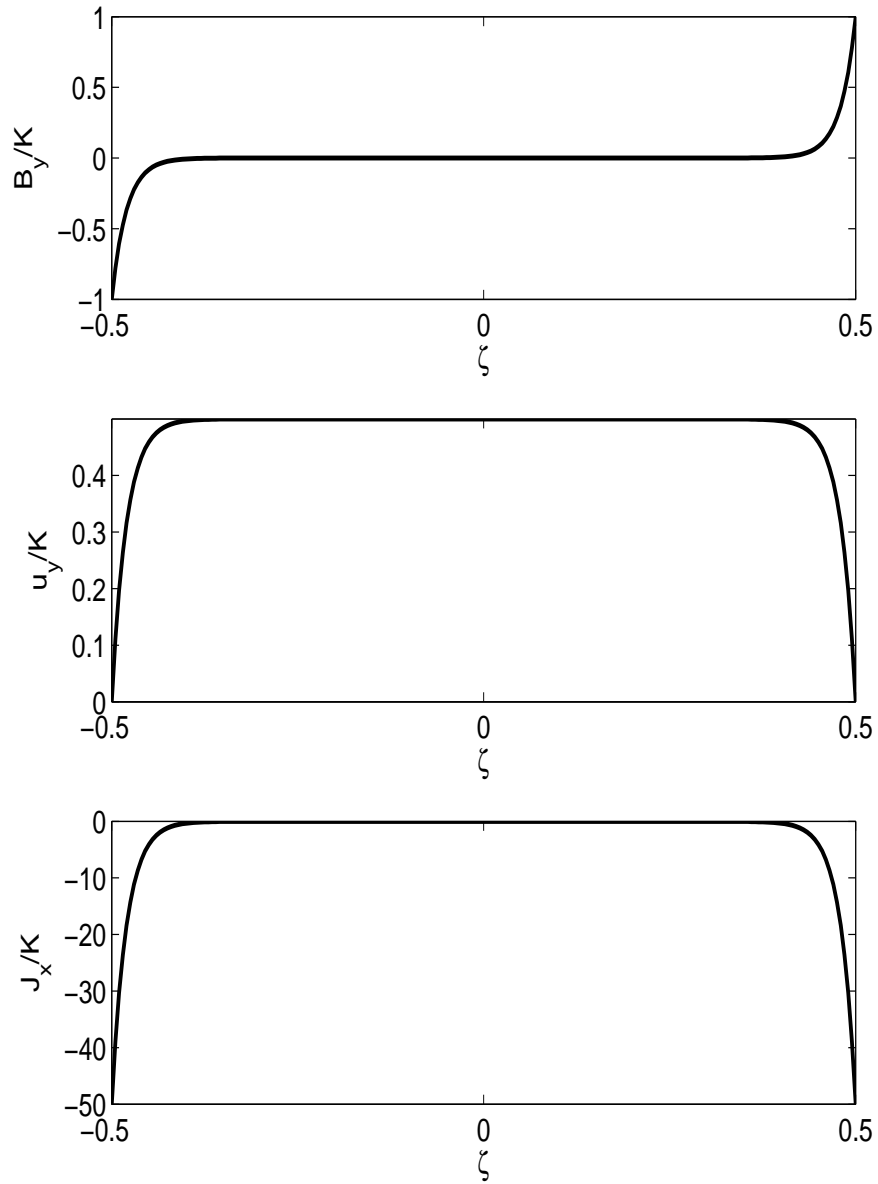


Figure 4.3: A solution of classical Hartmann problem for the normalized B_y/K , u_y/K and J_x/K along ζ . $(\mu, \eta, \varepsilon) = (0.04, 0.01, 0)$ is used. The Hartmann number H_a is therefore 50.

for large H_a . For fusion plasmas, η is very small. It means that it is very difficult to drive a crossfield flow in such plasmas. We define the momentum confinement time as

$$\tau_{mom} \equiv \frac{u_{y,max}}{K} . \quad (4.20)$$

(Note that $2K$ for the denominator should be used if τ_{mom} is strictly defined as “momentum per unit force”, accounting for the fact that there are two driving current terms, one from the top and one from the bottom boundaries. Yet, we prefer to skip the factor of 2 for simplicity.) The classical Hartmann momentum confinement time is then

$$\tau_{mom,\eta} = \sqrt{\frac{\eta}{\mu}} = \frac{\tau_{mom,\mu}}{H_a} , \quad (4.21)$$

where $\tau_{mom,\mu} \equiv 1/\mu$ is the confinement time due to classical viscous damping. (Note that the momentum confinement time is normalized to the Alfvénic time $\tau_a \equiv L/V_a$ according to our normalization). If MCX parameters are used, this classical Hartmann momentum confinement time is found to be about $2 \mu\text{s}$, which is not in agreement with current experimental data.

The final remark is that the Hartmann layer is typically very thin. Using MCX parameters, it could be as small as $l_H \sim 10^{-3}$ cm. There are two concerns. Firstly, l_H is much smaller than the ion skin depth c/ω_{pi} , which is about 2 cm. Secondly, for fixed external current (fix K), the total current across the plasma is fixed. But since Hartmann solution restricts almost all these current to be localized within the Hartmann layer, it produces a large current sheet. Both of the above two points brings up the consideration of the the Hall effect. We will consider it in the next

section.

4.2 Analytical Solution for the Resistive-Hall Hartmann Problem

Since we notice that there is a large crossfield current within the Hartmann layer, the Hall term, which is ignored in the last section might be important. In this section we would solve the same system as in the last section analytically with the Hall terms added. The only modification to the system, Eqs.(4.1)-(4.5), is Eq.(4.3).

We write the new system as follows:

$$\nabla p = \frac{1}{c} \mathbf{J} \times \mathbf{B} + \mu \nabla^2 \mathbf{u} \quad (4.22)$$

$$\nabla \times \mathbf{E} = 0 \quad (4.23)$$

$$\mathbf{E} = -\frac{1}{c} \mathbf{u} \times \mathbf{B} + \eta \mathbf{J} + \frac{1}{n_0 e c} \mathbf{J} \times \mathbf{B} - \frac{\nabla p_e}{n_0 e} \quad (4.24)$$

$$\mathbf{J} = \frac{c}{4\pi} \nabla \times \mathbf{B} \quad (4.25)$$

$$\nabla \cdot \mathbf{B} = 0. \quad (4.26)$$

Incompressibility, symmetry about $z = 0$ and $\partial_x = \partial_y = 0$ still hold. Carrying out similar procedures, we have the normalized equations, for \mathbf{u} and \mathbf{B} ,

$$u'_y = -\eta B''_y + \varepsilon B''_x \quad (4.27)$$

$$u'_x = -\eta B''_x - \varepsilon B''_y \quad (4.28)$$

$$B'_y = -\mu u''_y \quad (4.29)$$

$$B'_x = -\mu u''_x, \quad (4.30)$$

where $\varepsilon \equiv c/\omega_{pi}L$ is the Hall parameter and it is the new Hall physics we add in this section. The system above solves for B_x , B_y , u_x and u_y . The assertion $B_z = B_0$ is

still correct according to Eq.(4.26). The current density \mathbf{J} and electric field \mathbf{E} can be determined using Eq.(4.24) and Eq.(4.25) after obtaining \mathbf{u} and \mathbf{B} . By defining the variables,

$$\begin{aligned}\tilde{u} &\equiv u_y + iu_x \\ \tilde{B} &\equiv B_y + iB_x ,\end{aligned}\tag{4.31}$$

and the parameters $\tilde{\eta} \equiv \eta + i\varepsilon$, where $i = \sqrt{-1}$ is the purely imaginary number, we reduce Eqs.(4.27)-(4.30) to the system

$$\begin{aligned}\tilde{u}' &= -\tilde{\eta}\tilde{B}'' \\ \tilde{B}' &= -\mu\tilde{u}'' .\end{aligned}\tag{4.32}$$

These appear as exactly the same form as Eqs.(4.12) and (4.13). Since we still assume that the driving current is in the x -direction only and the flows are no-slip at the boundaries, we have the boundary conditions, $\tilde{B}(\pm 1/2) = \pm K$ and $\tilde{u}(\pm 1/2) = 0$. The solution is readily obtained by referencing to the last section.

After decomposing the solution into components, we have

$$\begin{aligned}u_x(\zeta) &= K\text{Im} \left\{ \sqrt{\frac{\tilde{\eta}}{\mu}} \frac{[\cosh(Q/2) - \cosh(Q\zeta)]}{\sinh(Q/2)} \right\} \\ u_y(\zeta) &= K\text{Re} \left\{ \sqrt{\frac{\tilde{\eta}}{\mu}} \frac{[\cosh(Q/2) - \cosh(Q\zeta)]}{\sinh(Q/2)} \right\} \\ B_x(\zeta) &= K\text{Im} \left\{ \frac{\sinh(Q\zeta)}{\sinh(Q/2)} \right\} \\ B_y(\zeta) &= K\text{Re} \left\{ \frac{\sinh(Q\zeta)}{\sinh(Q/2)} \right\} ,\end{aligned}\tag{4.33}$$

where $Q = 1/\sqrt{\mu\tilde{\eta}}$. It can be shown that when $\varepsilon = 0$, this solution is reduced to the classical Hartmann solution. There are two main points to be noted in this solution when comparing it with the classical Hartmann solution, Eq.(4.17).

First, flow in the x -direction and current density in the y -direction are generated. The origin of the secondary flow can be understood as follows. From Eq.(4.24),

the Hall term produce an y -component because of the J_x and B_z . However, E_y can only be a constant because of Eq.(4.23). Therefore, the variational part of the y -component of the Hall term has to be balanced by the first two terms on the RHS of Eq.(4.24). This results in the generation of J_y and u_x .

Second, the Hartmann number is essentially modified by replacing η with $\tilde{\eta} = \eta + i\varepsilon$. Fig. 4.4 and 4.5 show sample plots of a solution. Comparing these plots with Fig.4.3 we found that the Hartmann layer is broadened and $u_y(0)$ is larger, for the same η and μ . Therefore, ε indeed increases the “effective” resistivity in some way. Since the resistive-Hall Hartmann solution given above is quite complicated for analysis of the Hall effect. We will take the non-resistive limit, $\eta = 0$, in the next section.

4.2.1 The Non-resistive (Hall-only) Limit

Note that the Hall-Hartmann solution have been investigated for a while in the liquid metal community for different geometries, for example [54], however, as far as the author know, no one has discussed the solution of non-resistive (“Hall-only”) Hartmann flow problem. In this section, we give the solution for this case. By solving the Eqs.(4.27)-(4.30) with $\eta = 0$ [or taking the $\eta = 0$ limit for the solution

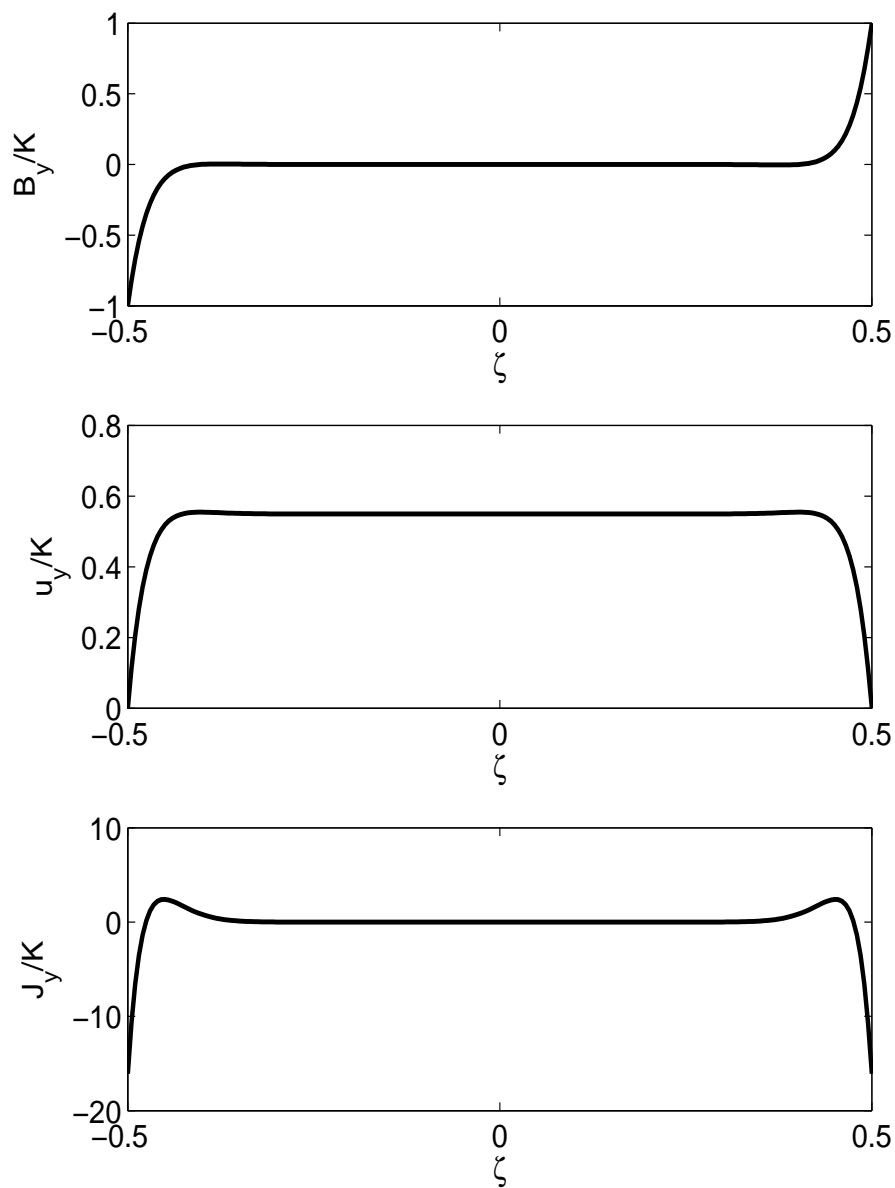


Figure 4.4: A solution of the Resistive-Hall Hartmann problem for the normalized B_y/K , u_y/K and J_y/K along ζ . $(\mu, \eta, \varepsilon) = (0.04, 0.01, 0.01)$ is used. Hartmann-Hall number $Q = 1/\sqrt{\mu(\eta + i\varepsilon)}$ is therefore $39 - 16i$.

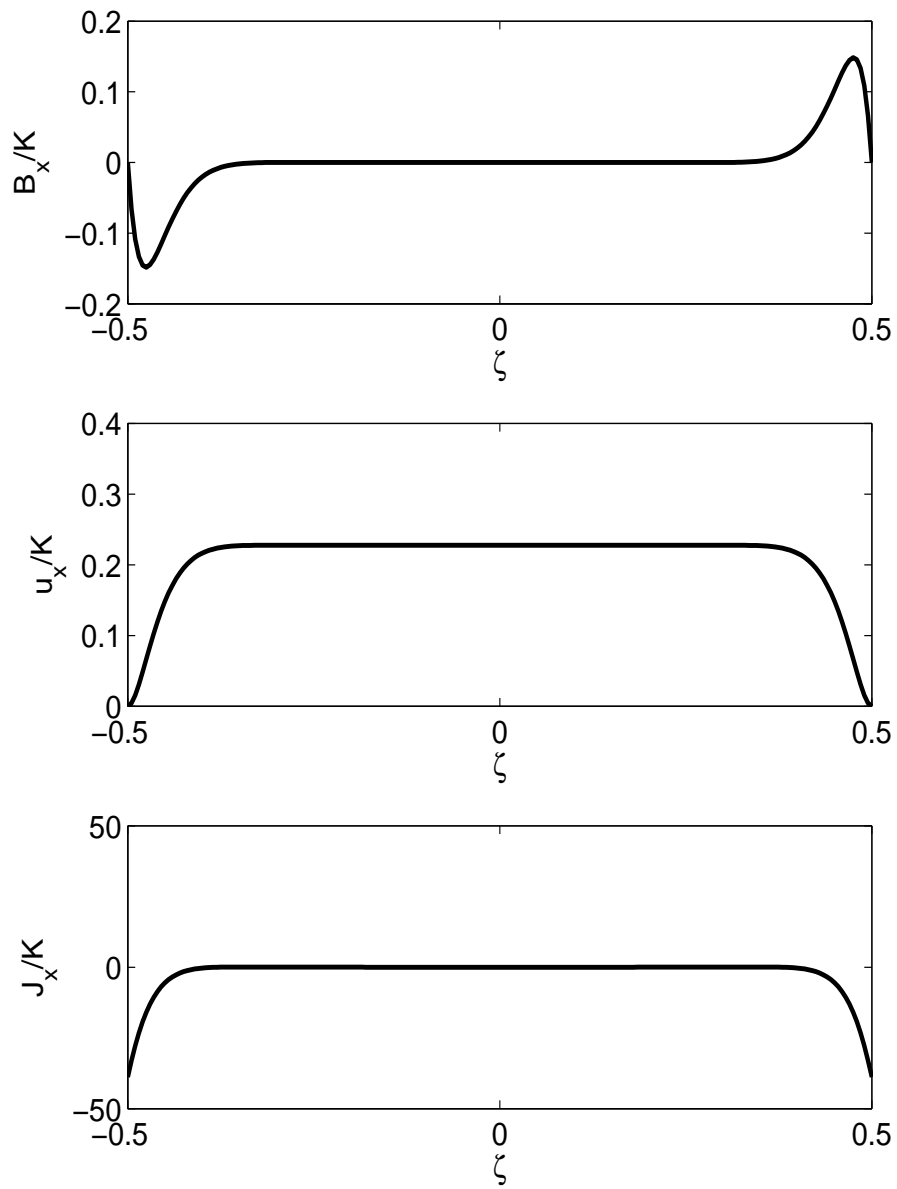


Figure 4.5: A solution of the Resistive-Hall Hartmann problem for the normalized B_x/K , u_x/K and J_x/K along ζ . $(\mu, \eta, \varepsilon) = (0.04, 0.01, 0.01)$ is used. Hartmann-Hall number $Q = 1/\sqrt{\mu(\eta + i\varepsilon)}$ is therefore $39 - 16i$.

Eq.(4.33)], we obtain the Hall-only solution:

$$\begin{aligned}
B_x &= \frac{2K}{\cosh q - \cos q} [\cosh(q/2) \sin(q/2) \sinh(qz) \cos(qz) \\
&\quad - \sinh(q/2) \cos(q/2) \cosh(qz) \sin(qz)] \\
B_y &= \frac{2K}{\cosh q - \cos q} [\cosh(q/2) \sin(q/2) \cosh(qz) \sin(qz) \\
&\quad + \sinh(q/2) \cos(q/2) \sinh(qz) \cos(qz)] \\
u_x &= \frac{2Kq\varepsilon}{\cosh q - \cos q} \{ - [\cosh(q/2) \sin(q/2) + \sinh(q/2) \cos(q/2)] \\
&\quad \times [\cosh(qz) \cos(qz) - \cosh(q/2) \cos(q/2)] \\
&\quad - [\cosh(q/2) \sin(q/2) - \sinh(q/2) \cos(q/2)] \\
&\quad \times [\sinh(qz) \sin(qz) - \sinh(q/2) \sin(q/2)] \} \\
u_y &= \frac{2Kq\varepsilon}{\cosh q - \cos q} \{ [\cosh(q/2) \sin(q/2) - \sinh(q/2) \cos(q/2)] \\
&\quad \times [\cosh(qz) \cos(qz) - \cosh(q/2) \cos(q/2)] \\
&\quad - [\cosh(q/2) \sin(q/2) + \sinh(q/2) \cos(q/2)] \\
&\quad \times [\sinh(qz) \sin(qz) - \sinh(q/2) \sin(q/2)] \} ,
\end{aligned} \tag{4.34}$$

where $q = 1/\sqrt{2\mu\varepsilon}$. We will discuss the solution qualitatively in the next section.

4.2.2 Implication and Discussion

As we have seen earlier when we discuss the solution for the resistive-Hall case, we see from the solution, Eq.(4.34) that the flows and B-field are two-dimensional rather than single dimension as in the classical Hartmann solution. Another point to note is that the Hall term contributes ‘‘harmonicity’’ to the solution, i.e., the oscillations given by the sine and cosine terms on top of the hyperbolic sine/cosine terms. Graphical solutions for the case $(\mu, \eta, \varepsilon) = (0.04, 0, 0.01)$ are shown

in Fig. 4.6 and 4.7. The oscillatory behaviors, which are absent in the classical Hartmann solution, is obvious. Also, the Hartmann layer width with Hall physics is of the order of $L_{H,\varepsilon} \sim 1/q \sim \sqrt{\mu\varepsilon}$. This point is very important in fusion device. It is because in a fusion grade plasma, $\varepsilon \gg \eta$, that means the Hartmann layer is broadened when we consider the Hall effect. Thus, we have

$$\frac{L_{H,\varepsilon}}{L_{H,\eta}} \sim \sqrt{\frac{\varepsilon}{\eta}} \gg 1 . \quad (4.35)$$

An even more important quantity to observe is the core flows that can be attained for a given driving current K . The core flow in y is given by

$$\begin{aligned} u_y(0) &= \varepsilon q K \frac{\sinh(q/2) + \sin(q/2)}{\cosh(q/2) + \cos(q/2)} \\ &\approx \varepsilon q K , \quad \text{for } q \gg 1 . \end{aligned} \quad (4.36)$$

Thus, the momentum confinement time is, for large q ,

$$\tau_{mom,\varepsilon} = \varepsilon q = \sqrt{\frac{\varepsilon}{2\mu}} . \quad (4.37)$$

Therefore, if $\varepsilon \gg \eta$, the momentum confinement with Hall effect being considered is much larger than the classical Hartmann confinement time. More explicitly, we have

$$\frac{\tau_{mom,\varepsilon}}{\tau_{mom,\eta}} = \sqrt{\frac{\varepsilon}{2\eta}} \gg 1 . \quad (4.38)$$

The factor of 2 in the denominator in Eqs.(4.37) and (4.38) can be explained by the fact that half of the momentum is transferred to the flow in the x -direction when Hall effect is operative. To see this, we calculate $u_x(0)$ for large q . We have

$$\begin{aligned} u_x(0) &= \varepsilon q K \frac{\sinh(q/2) - \sin(q/2)}{\cosh(q/2) + \cos(q/2)} \\ &\approx \varepsilon q K , \quad \text{for } q \gg 1 , \end{aligned} \quad (4.39)$$

which is the same as $u_y(0)$. In short, the Hall effect broadens the Hartmann layer and increases the momentum confinement time compared to the classical Hartmann result, by a factor of $\sqrt{\varepsilon/\eta}$. For MCX, this factor is about 20. For fusion grade plasma, this could be 10^3 to 10^4 .

We will make the last remark here. It should be noted that the origin of the difficulty in driving the (classical or not) Hartmann flow is the “almost” frozen-in condition. When a plasma is being forced (by a current or mechanical force) to flow across a strong B-field, the B-field would try to “freeze” the plasma in place and hinder the flow. It is well known that resistivity can break this frozen-in condition. The larger the flow can be for a given driving current for a larger resistivity. In this section, we have demonstrated that even without resistivity, it is still possible to break the frozen-in condition when the Hall effect is considered.

4.3 Summary

In this chapter, we reviewed a one dimensional classical Hartmann problem in which a resistive liquid metal flows (in y), across a strong external B-field, B_0 (along z), driven by current (in x). It is found that when the Hartmann number $H_a = \sqrt{B_0^2 L^2 / \mu \eta c^2}$, where L is the system size, μ is the viscosity coefficient and η is the resistivity, is large, it is very difficult to drive the flow. In other words, the momentum confinement time is very short compared with the case without the external B-field. The Hartmann momentum confinement time is inversely proportional to H_a . Also a Hartmann boundary layer exists with width also inversely

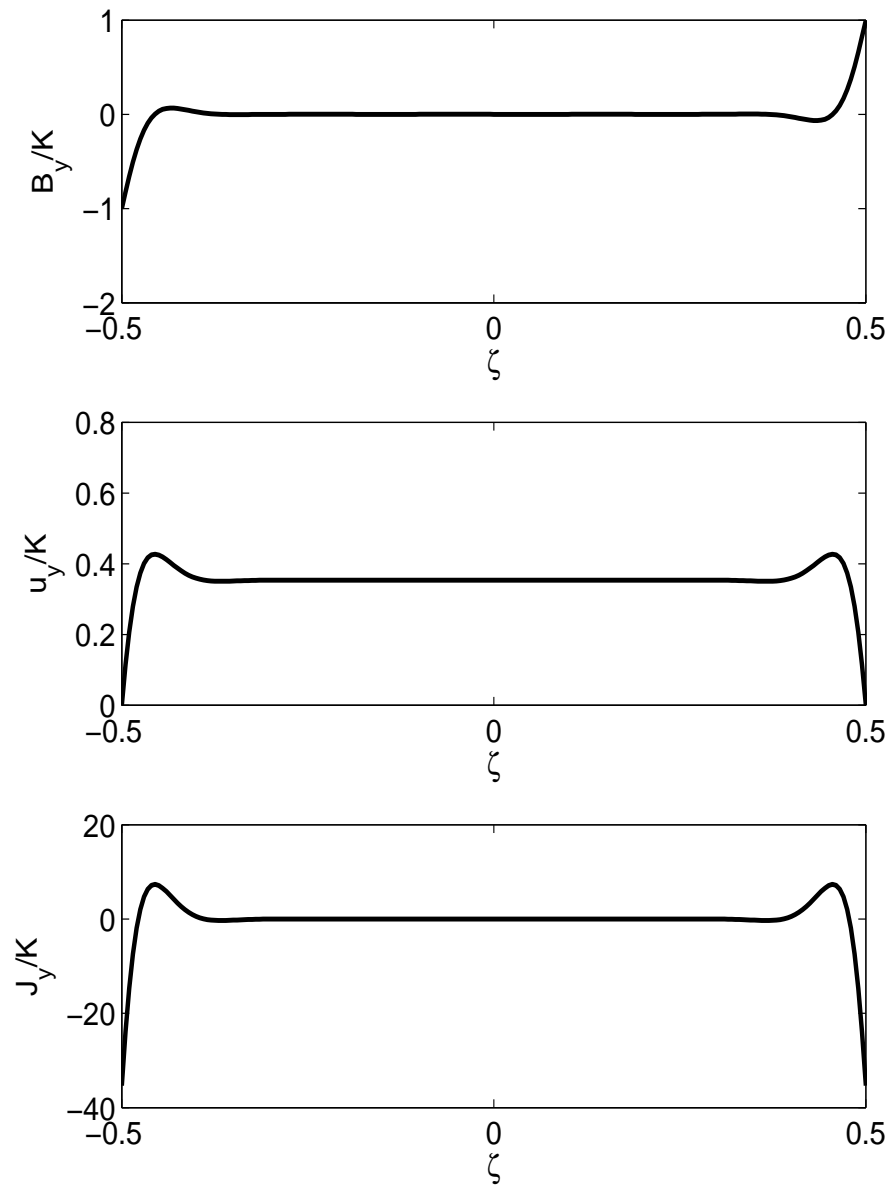


Figure 4.6: A solution for the Non-resistive Hartmann problem for the normalized B_y/K , u_y/K and J_y/K along ζ . $(\mu, \eta, \varepsilon) = (0.04, 0, 0.01)$ is used. Hall number $q = 1/\sqrt{2\mu\varepsilon}$ is therefore 35.

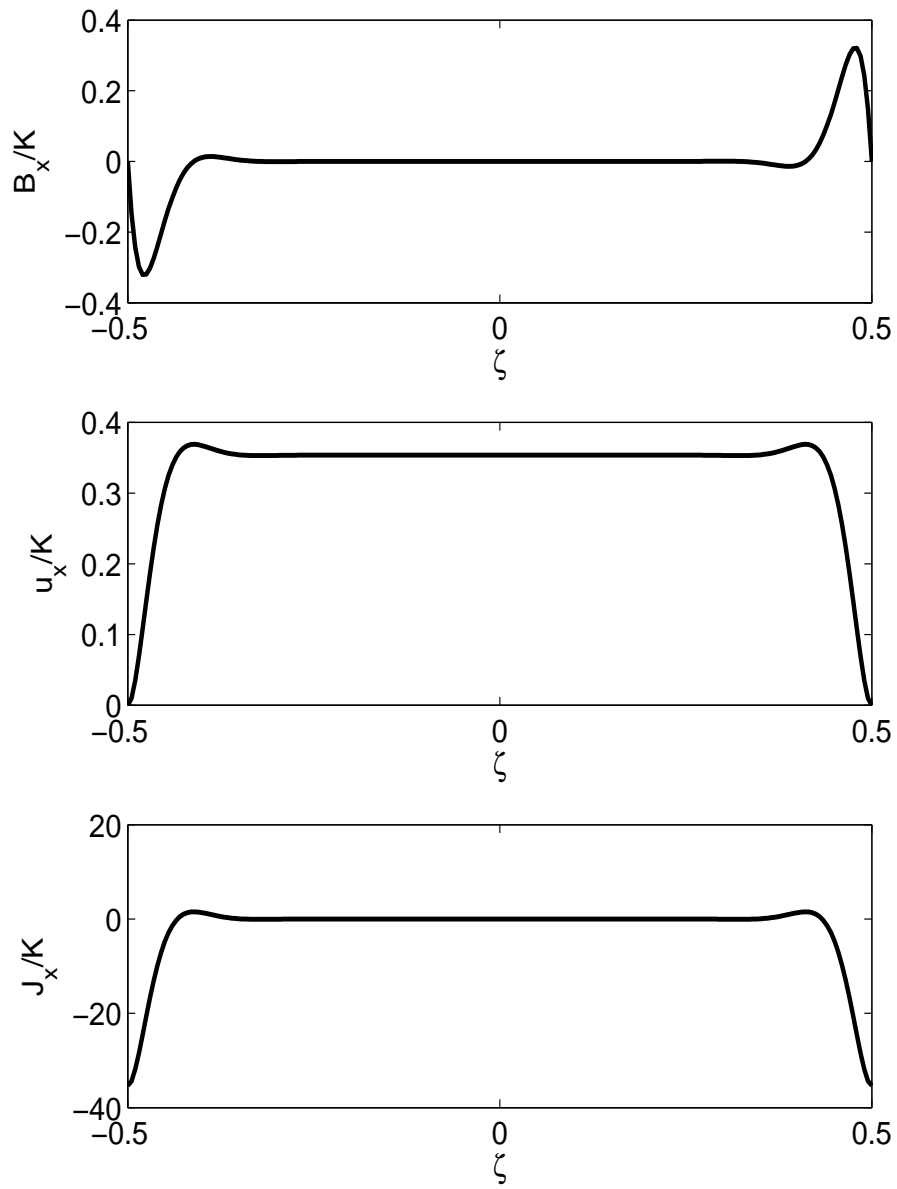


Figure 4.7: A solution for the Non-resistive Hartmann problem for the normalized B_x/K , u_x/K and J_x/K along ζ . $(\mu, \eta, \varepsilon) = (0.04, 0, 0.01)$ is used. Hall number $q = 1/\sqrt{2\mu\varepsilon}$ is therefore 35.

proportional to H_a . Due to the existence of a current within the thin Hartmann layer, we extended the original calculation by retaining the Hall terms in the electron momentum equation. An analytic solution is found. It shows that the role of the Hall physics is essentially represented by replacing the resistivity η by $\eta + i\varepsilon$, where $\varepsilon = c/\omega_{pi}L$ is the Hall parameter, in the original solution. Since $\varepsilon \gg \eta$ in fusion grade plasma, if this solution is applicable to a plasma also, we expect the Hall effect should be dominant and that the momentum confinement time would be much longer while the Hartmann layer would be broadened. Table 4.1 compares the momentum confinement times for current operating parameters of MCX and a fusion grade plasma, due to the viscous damping, resistive-Hartmann and Hall-Hartmann physics. One should also note that in the Hall-Hartmann solution, a flow(current) perpendicular to both of the external B-field and the original flow(current) is created, and its size is comparable to the original flow for large “effective” Hartmann number. If we take a large inner radius limit in MCX, the geometry would be the same the one we considered here. That is, (x, y, z) corresponds to (r, ϕ, z) . The implication on MCX is that, the secondary flow due to Hall effect might be radially inward or outward depending on whether the driving current is radially outward or inward. In a plasma-neutral system, this net divergence of plasma, in steady state, should be compensated by the neutral flux into the core. Yet, a full MCX analysis in this regard is out of the scope of the present study. Finally, it is found that the “frozen-in” condition can be broken without resistivity, by merely including the Hall effect.

Mom. Conf. Time	MCX	Fusion Parameters
$\tau_{cl.vis.}$ (Viscous)	28 ms	4.4×10^4 s
$\tau_{H,\eta}$ (Resistive)	$1.7 \mu s$	$0.8 \mu s$
$\tau_{H,\varepsilon}$ (Hall)	$26 \mu s$	22 ms

Table 4.1: Momentum confinement times for MCX and fusion grade plasma due to different physics. First row: Classical viscous damping. Second row: Resistive Hartmann flow. Third row: Hall Hartmann flow.

Chapter 5

Conclusion

In Chapter 2, plasma-neutral interactions across the field line and along the magnetic field line are considered for a centrifugally confined plasma. The main focus is the parallel confinement in a system wherein a crossfield plasma rotation inhibits plasma escape along the magnetic field. Analytic and numerical solutions from a simple one-dimensional isothermal model are obtained. It is shown that for perfect recycling the neutral density at the wall is exponentially smaller than the central plasma density for strong centrifugal confinement compared to the case of no confinement for which the neutral wall density equals the central plasma density. Eqs.(2.71) and (2.72) show the exponential factors in the limits, $1 \ll \hat{\alpha}e^{-\tilde{g}_0}$ and $1 \gg \hat{\alpha}e^{-\tilde{g}_0}$, respectively, where $\hat{\alpha}$ is the ratio of the CX to ionization cross-sections and \tilde{g}_0 corresponds to $M_s^2/2$ where M_s is the sonic Mach number of the rotational speed.

The effective neutral penetration depth along the field, of the same order as the crossfield penetration depth in the zero confinement limit, increases exponentially in the strong confinement case. This penetration length increase is due to the decrease in local plasma density (and thus CX interaction) which allows more fast moving neutrals to reach the core edge. However, kinetic theory has to be used for quantitative description when plasma density becomes too small so that λ_{cx} is larger

than macroscopic scales.

Our results suggest that the neutral density at the MCX insulator may be smaller or larger than the neutral density at the radial walls, depending on parameters. The neutral density at the insulator scales as $\hat{\alpha}^{1/2}e^{-M_s^2/2}n_{core}$, while crossfield neutral density scales[19] as $Dn_{core}/(2l_0^2\gamma_i)$ [using Eq.(2.4) with some algebra] where l_0 is defined in Eq.(2.30), $\gamma_i \equiv \alpha_i n_{core}$ is the ionization rate and D is probably dominated by non-classical effects. In principle, D is the crossfield classical particle diffusion coefficient. If we use this classical result and $l_0 \approx 5\text{cm}$ for MCX, $N_{||}$ and N_{\perp} are equal if $M_s = [2 \ln (2l_0^2\gamma_i\hat{\alpha}^{1/2}/D)]^{1/2}$. Thus, the critical $M_s \approx 4.6$ for $T = 30\text{ eV}$, $B = 0.2\text{ Tesla}$ and $n = 10^{14}\text{ cm}^{-3}$. MCX generally operates for M_s in the range 2 to 3.5. Thus, our result indicates that MCX is presently running in the high end-wall neutral density region, assuming classical diffusion. However, since D is likely to be larger, the general operation may span both the cases of high end-wall neutral density and high side-wall neutral density.

In Chapter 3, we have extended an existing plasma fluid code to a 2D isothermal plasma-neutral fluid code. It is used to study the centrifugally confined plasma, in particular MCX. A reasonable artificial force term in the plasma momentum equation is used to model the confinement force. Boundary conditions are carefully taking care of and well tested, to deal with the wall boundaries. Close to realistic parameters are used. Result shows that neutral density “re-equilibrate” occurs significantly when confinement is weak. Simulation also shows that within realistic operation range of MCX, neutral wall-density could be higher in the end-wall or in the side-wall, depending on M_s . Transition could occurs for M_s between 3 to 4.

If our model is a good approximation, the interaction parameter nN should be a good indication of ionization/CX rate. Therefore, comparisons with experimental measurements on such rates should greatly benefit both of the code improvement and experimental understanding.

In order to understand how frictional force is limiting the momentum confinement time, in Chapter 4, we reviewed a one dimensional classical Hartmann problem. It describes a resistive liquid metal flows (in y), across a strong external B-field, B_0 (along z), driven by current (in x). It is found that when the Hartmann number $H_a = \sqrt{B_0^2 L^2 / \mu \eta c^2}$, where L is the system size, μ is the viscosity coefficient and η is the resistivity, is large, it is very difficult to drive the flow. In other words, the momentum confinement time is very short compared with the case without the external B-field. The Hartmann momentum confinement time is inversely proportional to H_a . Also a Hartmann boundary layer exists with width also inversely proportional to H_a . Due to the existence of a current within the thin Hartmann layer, we extended the original calculation by retaining the Hall terms in the electron momentum equation. Analytic solution is found. It shows that the role of the Hall physics is essentially represented by replacing the resistivity η by $\eta + i\varepsilon$, where $\varepsilon = c/\omega_{pi}L$ is the Hall parameter, in the original solution. Since $\varepsilon \gg \eta$ in fusion grade plasma, if this solution is applicable to a plasma also, we expect the Hall effect should be dominant and that the momentum confinement time would be much longer while the Hartmann layer would be broadened. One should also note that in the new solution, a flow(current) perpendicular to both of the external B-field and the original flow(current) is created, and its size is comparable to the original

flow for large “effective” Hartmann number. If we take a large inner radius limit in MCX, the geometry would be the same the one we considered here. That is, (x, y, z) corresponds to (r, ϕ, z) . The implication on MCX is that, the secondary flow due to Hall effect might be radially inward or outward depending on whether the driving current is radially outward or inward. Finally, it is found that the magnetic field line can be broken without resistivity, by merely considering the Hall effect.

In order to have a more complete physics picture, some future studies should be done. First, we need to investigate whether kinetic theoretical analysis[24, 25] is necessary in the one-dimensional analytic and two-dimensional numerical[15] calculations. Kinetic theory might be needed because in the boundary region, especially when confinement is strong, the plasma density drop resulting in long charge-exchange and ionization mean free paths. If these interaction scales are comparable or longer than the macroscopic scale length(s), e.g. system sizes or the distance from the wall to the B-field curvature region, fluid theory in principle should fail. Although, previous experiences from other researchers[16] suggest that fluid theory still gives reasonably good results in these “illegal” regimes, care has to be taken.

Second, the 2D simulations we have done is in a slab geometry. Our results show that even in such a 2D configuration, the behavior in two perpendicular directions are almost decoupled. However, we should expect more interesting dynamics in the mirror field geometry that is actually operating in MCX. For a full MCX geometry analysis, we need to understand more about the boundary conditions because field lines are tilted at some parts of the boundary. Also the Hartmann flow physics enforces a relatively thin boundary layer without considering Hall physics.

These are difficult to deal with numerically in the present stage. Yet, in Appendix E, we provide a preliminary MCX simulation result, by bypassing these questions.

Our Hartmann problem investigation reveals that Hall effects might be important and even constructive to the MCX momentum confinement time. However, a secondary flow in the radial direction might be a concern. Some questions have to be asked. Would the secondary flow destroy the confinement? Would a reverse driving current save the situation? Does steady state even exist as net divergence of plasma is predicted. Could neutral recycling be the solution? These are all interesting questions. A full system analysis with neutral physics should be considered with both analytical and numerical methods.

Appendix A

Parallel-to-field Plasma-Neutral Equilibria Asymptotic Calculations

A.1 1D Solution with Bohm equality as the boundary condition

In this section, we will solve the same problem as in Sect.2.2.2, but we now change the boundary condition from $n_w = 0$ to one that fixes the plasma flow u_w to the (negative) sound speed (or $u_w = -\hat{\alpha}^{1/2}$ condition in the present unit system). This is the equality form of the well-known Bohm criteria[16]. All the equations starting from Eq.(2.35) to Eq.(2.44) are still correct but the value of N_w in Eq.(2.44) is not unity any more for a finite u_w . In Sect.2.2.2, $n_w = 0$ effectively means u_w goes to (negative) infinity for a finite flux hitting the wall. Thus our goal here is to find N_w given finite u_w . From Eqs.(2.39)-(2.41), we have $N' = nu$. Thus, we have at the wall, by using Eq.(2.40) again,

$$N_w = 1 - \frac{N'_w}{u_w} . \quad (\text{A.1})$$

By taking a derivative of Eq.(2.44) w.r.t. ζ at $\zeta = 0$ and substituting it in Eq.(A.1), we get a third order polynomial equation for N_w , namely,

$$2/(3u_w^2)N_w^3 + (1 - 1/u_w^2)N_w^2 - 2N_w + 1 = 0 . \quad (\text{A.2})$$

Note that the only acceptable values of N_w should be between 0 and unity for a cold ion system which we have assumed throughout the present article. For large $\hat{\alpha}$

which we have assumed throughout, N_w and n_w can be approximated as

$$\begin{aligned} N_w &\approx 1 - \frac{1}{(3u_w^2)^{1/2}} = 1 - \frac{1}{(3\hat{\alpha})^{1/2}} , \\ n_w &\approx \frac{1}{(3\hat{\alpha})^{1/2}} \end{aligned} \tag{A.3}$$

for $\hat{\alpha} \gg 1$. This result has been verified, for example, numerically solving Eqs.(2.49-2.51) gives $N_w = 0.874$ and $n_w = 0.126$ for $\hat{\alpha} = 20$. From this approximation, we can deduce that the plasma particle flux hitting the wall would be, in real units, $|\Gamma_w| \approx n_{core} c_s (3\hat{\alpha})^{-1/2}$, which suggests a decrease in plasma flux when the drag due to CX cross-section increases, that is $\hat{\alpha} (\equiv \alpha_{cx}/\alpha_i)$ increases. As pointed out by Stangeby [16], when considering the plasma dynamics in the ‘‘elastic collision zone’’ (no ionization occurs within which), this result should be expected. What we added here is the importance of the relative cross-section of CX and ionization. Note also that when $\hat{\alpha} \rightarrow \infty$, this result is the same as the one shown in Sect.2.2.2 with $n_w = 0$ as boundary condition.

A.2 Weak Confinement Approximation with Bohm Equality Boundary Condition

In this section, we will find an approximate solution for N_w in the weak confinement regime, $\tilde{g}_0 \ll 1$ with the Bohm equality boundary condition, that is $u_w = -\hat{\alpha}^{1/2}$, imposed. Assuming $\zeta_1 \sim O(1)$, for small \tilde{g}_0 , this would imply $N_1 \sim O(1)$. Let’s assume this is the case, to be checked later. From Eq.(2.61), we have, for $\tilde{g}_0 \ll 1$,

$$N_1 \approx A_w - \frac{1 - A_w}{\tilde{g}_0} . \tag{A.4}$$

Since we assume that N_1 is of order unity, we now let

$$1 - A_w = \gamma \tilde{g}_0 , \quad (\text{A.5})$$

where γ is of order unity. Therefore we have

$$N_1 \approx 1 - \gamma - \gamma \tilde{g}_0 \approx 1 - \gamma . \quad (\text{A.6})$$

From Eq.(2.63), we have

$$C_{<} \approx \frac{2}{3} \gamma \tilde{g}_0 (1 - \gamma)^3 . \quad (\text{A.7})$$

It can be seen from Eq.(2.55) that the term $C_{<}$ can be neglected, because both N_w and N_1 are order of unity but $C_{<}$ is proportional to \tilde{g}_0 . Therefore, for $\zeta < \zeta_1$, we have

$$N' \approx - \left(A_w^2 N^2 - \frac{2}{3} A_w N^3 \right)^{1/2} . \quad (\text{A.8})$$

We now express n_w in terms of N_w by imposing the boundary condition. With Eq.(2.50) and (2.53), we have

$$n_w = \frac{N'_w}{A_w u_w} = - \frac{N'_w}{A_w \hat{\alpha}^{1/2}} . \quad (\text{A.9})$$

Now using Eq.(A.8) with the above equation and assuming $n_w \ll N_w$ which will be checked later, we arrive at

$$n_w \approx \frac{N_w}{(3\hat{\alpha})^{1/2}} , \quad (\text{A.10})$$

and therefore, with Eq.(2.53),

$$A_w = \beta N_w , \quad (\text{A.11})$$

where $\beta \equiv 1 + 1/(3\hat{\alpha})^{1/2}$. Integrating Eq.(A.8) from $\zeta = 0$ to $\zeta = \zeta_1$, we have

$$N_1 \approx \frac{3}{2} A_w \text{sech}^2 \left(\frac{1}{2} \zeta_1 A_w + \tanh^{-1} \sqrt{1 - \frac{2}{3\beta}} \right) . \quad (\text{A.12})$$

Since $A_w = 1 - \gamma\tilde{g}_0$, we can expand the hyperbolic secant function in the above equation by taking the term proportional to \tilde{g}_0 to be small. Defining

$$f_{\zeta_1} \equiv \tanh \left[\zeta_1/2 + \tanh^{-1}(1 - 2/3\beta)^{1/2} \right], \quad (\text{A.13})$$

and using $N_1 \approx 1 - \gamma$, we could finally get, up to the first order of \tilde{g}_0 ,

$$N_w = \frac{1}{\beta} \left[1 - \frac{\tilde{g}_0}{2}(3f_{\zeta_1}^2 - 1) \right], \quad (\text{A.14})$$

Therefore, the assumption that γ and N_1 is of order unity is checked, if $\zeta_1 \sim O(1)$.

Numerical results from Eq.(2.58) for small \tilde{g}_0 agree with this calculation to within 4%.

Appendix B

Normalized Equation for the NM CX in 1D parallel direction

For a convenient reference on how to scale the parameters in the NM CX, we would like to renormalize the equation in the code's normalization rather the normalization presented in this paper. We start with re-stating Eq.(2.25) here again,

$$B\partial_t(Mnu_{\parallel}^2/B) = -\partial_t p - \alpha_{cx}MnN(u_{\parallel} - U_{\parallel}) + \alpha_iMNnU_{\parallel} + \frac{Mn}{2}\partial_t u_{\theta}^2 . \quad (\text{B.1})$$

The normalized version is

$$B(nu_{\parallel}^2/B)' = -s\hat{T}n' - \hat{\alpha}_{cx}nN(u_{\parallel} - U_{\parallel}) + \hat{\alpha}_i nNU_{\parallel} + \frac{n}{2}(u_{\theta}^2)' , \quad (\text{B.2})$$

where variables are normalized as densities to n_0 , length to L_0 , flow speed to Alfvén speed V_A , B to B_0 and $s \equiv p/nT$, $\hat{T} \equiv T/MV_A^2 = (c_s/V_A)^2$, $\hat{\alpha}_{cx} \equiv \alpha_{cx}n_0L_0/V_A$ and $\hat{\alpha}_i \equiv \alpha_i n_0L_0/V_A$. Now Eq.(B.2) is exactly what it appears in the Fortran code (with slap geometry), when we replace the last term above by ng . That means we have

$$\frac{(u_{\theta}^2)'}{2} = \frac{1}{2} \left(\frac{c_s}{V_A} \right)^2 (M_s^2)' = \frac{\hat{T}}{2} (M_s^2)' = g , \quad (\text{B.3})$$

where M_s is the sonic Mach number of the rotation dependent on l , or

$$\int_{l_a}^{l_b} g dl = \frac{u_{\theta}^2(l_b) - u_{\theta}^2(l_a)}{2} . \quad (\text{B.4})$$

To make a connection with the result of the calculation by Ellis et al. [2] without considering neutrals interactions, we retain only the pressure and artificial confinement

terms in Eq.(B.2) and the equation becomes

$$(\ln n)' = \frac{g}{s\hat{T}} = \frac{M_s^{2'}}{2s} . \quad (\text{B.5})$$

Note that $s = 2$ in [2] and the results agree, that is

$$n = n_o e^{M_s^2/4} . \quad (\text{B.6})$$

Let us return to the Fortran Code equation, that is Eq.(B.2) with (B.3) substitution. In a mirror field, the bending of the B-field is localized and thus the function g (or M_s) should also be localized in the parallel direction. To model the mirror field, we assume g is a gaussian with the peak located at the midpoint of the bending region of the B-field line. Mathematically,

$$g = g_0 \exp [-k^2 (l - l_1)^2] , \quad (\text{B.7})$$

where the number k and l_1 model the scale and location of the the bending field respectively. Fig.B.1 shows an example of such a confinement force and the corresponding flow profile according to Eq.(B.3) by taking an integration of g along l . We are now ready to obtain the numerical value of g_0 used in the simulation. From Eq.(B.3), integrating \hat{g} from $l = 0$ to l_{core} which can be assumed to be infinite, we have

$$g_0 = \frac{k}{\sqrt{\pi}} \left(\frac{u_{\theta,\infty}^2}{2} - \frac{u_{\theta,0}^2}{2} \right) = \frac{k\hat{T}}{2\sqrt{\pi}} M_{s,\infty}^2 . \quad (\text{B.8})$$

The last equality above is obtained if we assume no-slip boundary condition for the azimuthal flow. For example, if $M_{s,\infty} = 3$, $\hat{T} = 0.04$ and $k = 1$, $g_0 \approx 0.1$.

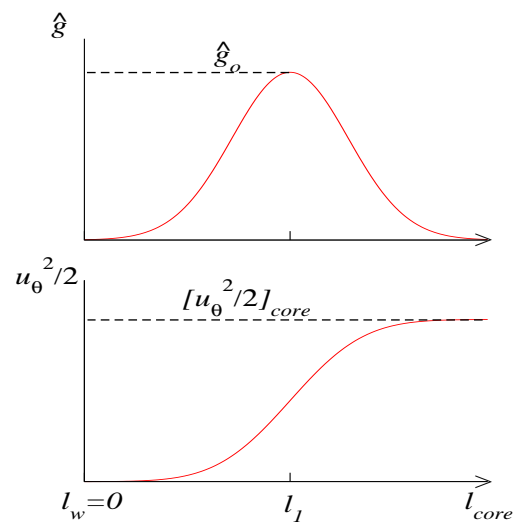


Figure B.1: Modeling of the centrifugal confinement force in simulations: Plots of the model confinement force and the corresponding rotational speed square, as a function of distance along the B-field line.

Appendix C

Estimation of $M_{s,crit}$ by combining the 1D solutions in crossfield and along the field directions

We would like to estimate at what value of the neutral wall densities at the end-wall and the side-wall equal, from the analytical results. Since we have, from Chapter 2, for large confinement (large M_s),

$$N_{\parallel,w} \approx \hat{\alpha}^{1/2} e^{-M_s^2/2} n_{core} \quad (\text{C.1})$$

and

$$N_{\perp,w} \approx \frac{\alpha_{cx}\eta}{3B^2} n_{core}^3 . \quad (\text{C.2})$$

By definition, $M_{s,crit}$ occurs at

$$\frac{N_{\perp,w}}{N_{\parallel,w}} = 1 , \quad (\text{C.3})$$

therefore, it is easily to get

$$M_{s,crit} = \left[2 \ln \left(\frac{3B^2}{\sqrt{\alpha_{cx}\alpha_i}\eta n_{core}^2} \right) \right]^{1/2} . \quad (\text{C.4})$$

Appendix D

Possible Density-Variation Effect on Hartmann Problem

In this appendix, we show that the Hartmann number or the limitation on the core flow and momentum confinement time are affected by the viscosity at the boundary rather than its value at the core. This is important when Hartmann physics is used to describe a plasma in which there is a large density variation from the core to the wall.

We see from Chapter 4 that the viscosity μ plays an essential role in slowing down crossfield flow, in the Hartmann problem. Both of the Hartmann number and momentum confinement time are proportional to $1/\sqrt{\mu}$. However, it should also be noted that μ is only operative in the Hartmann layer region. It is because only the term $\mu\nabla^2\mathbf{u}$ in the momentum equation¹ involves μ and that the flow is almost constant outside the Hartmann layer. Therefore, the solution given in Eq.(4.19) should also be good if we replace μ by μ_w , the value of viscosity at the boundary, that is

$$u_{y,c} \approx K \sqrt{\frac{\eta}{\mu_w}}. \quad (\text{D.1})$$

In the followings, we explain the above claim more explicitly. Consider only the classical Hartmann problem presented in Chapter 4. The force balance in the Hartmann

¹The distinction between $\mu\nabla^2\mathbf{u}$ and $\nabla\cdot(\mu\nabla\mathbf{u})$ is not important as long as μ is about a constant across the Hartmann layer

layer in this case, normalized according to Chapter 4, is

$$J_x = \mu u_y'' . \tag{D.2}$$

While in the core region, both sides of the above equation does not contribute any force. Therefore, to specify the Hartmann number or its momentum confinement time, we only need to know the viscosity in the boundary region.

From Chapter 2 and 3, we know that, in general, plasma density n is a function of spatial distance from the wall. As it gets closer to the wall, the plasma density gets smaller. In particular, in a centrifugally confined plasma, the ratio of the plasma wall density to the plasma core density is proportional to $\exp(-M_s^2/4)$ (see Appendix B and [2]), where M_s is the azimuthal rotation sonic Mach number. On the other hand, if we use the viscosity coefficient according to Braginskii[55], we find that μ is proportional to n^2 . If we also consider the neutral charge-exchange interaction, μ should roughly proportional to nN . Therefore, we would expect μ is a function of space and usually becomes smaller in the boundary region when n gets smaller.

Concluding the last two paragraphs, we deduce that the Hartmann problem is indeed irrelevant if the plasma density is small enough at the boundary. However, since we could not solve the Hartmann problem for a plasma system with spatial dependent density analytically. In the following, we assume that the spatial dependence of the plasma density is prescribed and that the force balance in the z direction is irrelevant to the crossfield momentum balance (That is we essentially ignore any particle and momentum balance in the z direction but assume a density

variation along z). We could then estimate the core plasma flow and momentum confinement time in this case.

We re-state the one-dimensional classical Hartmann configuration here. Two insulating infinite plates are placed at $\zeta = -1/2, 1/2$ ($z = -L/2, L/2$). A strong external magnetic field is applied in the z -direction. The total driving current flowing in the negative x -direction per unit length in y is $2K_s$, which drives a plasma flow in the y -direction. In this system, the only component of E-field is in the (negative) x -direction. In steady state, we have,

$$\nabla \times \mathbf{E} = 0 . \tag{D.3}$$

Since $\mathbf{E} = E_x \hat{x}$, we deduce that E_x is a constant. We assume Ohm's law is an accurate description for the system as in the classical Hartmann problem,

$$\mathbf{E} = -\mathbf{u} \times \hat{\mathbf{z}} + \eta \mathbf{J} . \tag{D.4}$$

It is found that the usual Hartmann result is still valid, that is, when $H_a \gg 1$, J vanishes at the core, as long as μ is slowly varying in the Hartmann layer scale. Thus, in the core region, we have

$$E_x \sim -u_{y,c} . \tag{D.5}$$

On the other hand, at the edge, we have (ignoring u_z),

$$E_x \sim \eta J_{x,w} . \tag{D.6}$$

From Eq.(D.5) and (D.6), we arrive at

$$u_{y,c} \sim -\eta J_{x,w} \tag{D.7}$$

It is known that almost all the current density of the plasma are located inside the very thin Hartmann layer close the wall. Since the total current per unit length in y is $2K_s$, we have

$$2K_s \sim -2J_{x,w}l_H , \quad (\text{D.8})$$

where l_H is the Hartmann layer width given by L/H_a where L is the size of the system in z and H_a is the Hartmann number. Using Eq.(D.7) in (D.8), we obtain

$$u_{y,c} \sim \frac{\eta K}{l_H} . \quad (\text{D.9})$$

It is very important to note, for constant current K_s and resistivity η , the core flow $u_{y,c}$ is determined by l_H which is a property defined by the edge parameters. To see the last part of this statement, we can investigate the force balance in the y -direction at the edge region. In the edge region, the flow changes from zero to a certain value ($u_{y,c}$) in a very short scale and therefore dragging force from the viscosity is very large. This dragging force is balanced by the Lorentz force produced by the thin current sheet $J_{x,w}$ cross B force. Mathematically,

$$\begin{aligned} J_{x,w} &\sim \mu_w u_y'' \\ &\sim \mu_w u_{y,c} / l_H^2 . \end{aligned} \quad (\text{D.10})$$

Note that the assumption that the viscosity is almost a constant in $\sim O(l_H)$ around the wall has been used. Using Eq.(D.7) in (D.10), we have

$$l_H \sim \sqrt{\mu_w \eta} . \quad (\text{D.11})$$

It shows that l_H decreases as μ_w decrease. Also, we obtain Eq.(D.1) as claimed.

Using the model with the viscosity given by η_1 from Braginskii[55], we have $\mu \equiv \tilde{\mu} n^2$ and thus $\mu_w \sim \tilde{\mu} n_w^2$. (Note that making μ dependent on n does not violate

the requirement that μ should be almost a constant around the wall as long as the length scale of n profile is much larger than l_H). In short, from Eq.(D.9) and (D.11), we have

$$u_{y,c} \sim \frac{1}{n_w} \sqrt{\frac{\eta}{\tilde{\mu}}} K . \quad (\text{D.12})$$

This essentially is the same equation that we derived in Chapter 4, but the point here is to clearly state the dependence of the density at the wall when density profile in the larger scale is a concern.

To estimate the momentum confinement time, we use the dimensional unit from now on. We also define an average fluid density n_{ave} as

$$n_{ave} \equiv \frac{1}{L} \int_{L/2}^{L/2} n dz . \quad (\text{D.13})$$

The core flow is then,

$$u_{y,c} \approx \frac{4\pi K_s}{cB_0} \sqrt{\frac{\tau_{\mu,w}}{\tau_\eta}} V_a \quad (\text{D.14})$$

where $\tau_\eta = 4\pi L^2/\eta c^2$, $\tau_{\mu,w} = n_{ave} M L^2/\mu_w$ and $V_a \equiv \sqrt{B_0^2/4\pi n_{ave} M}$. Note from Eq.(D.11) that $L_H \propto n_w$ which is small, thus, $u_y \approx u_{y,c}$ in almost all the region except the thin Hartmann layer. Redefine momentum confinement time to

$$\tau_{mom} = \frac{\int n M u_y dz}{f} , \quad (\text{D.15})$$

where f is the force density $K_s B_0/c$ in the y -direction. We have the modified Hartmann momentum confinement time,

$$\tau_{mom,\eta} \sim \frac{M u_{y,core} n_{ave} L}{f} \quad (\text{D.16})$$

$$= \tau_a \sqrt{\frac{\tau_{\mu,w}}{\tau_\eta}} , \quad (\text{D.17})$$

where $\tau_a \equiv L/V_a = L\sqrt{4\pi Mn_{ave}}/B_0$ and

$$\tau_{\mu,w} \equiv \sqrt{\frac{L^2 n_{ave} M}{\mu_w}} \quad (\text{D.18})$$

$$= \frac{n_{ave}}{n_w} \sqrt{\frac{L^2 n_{ave} M}{\mu_{ave}}} \quad (\text{D.19})$$

$$= \frac{n_{ave}}{n_w} \tau_{\mu,ave} . \quad (\text{D.20})$$

Therefore, the momentum confinement time is proportional to the ratio of average density to the wall density, which could be significant. Note that in a system with significant density variation in the z -direction in a large length scale (i.e $L_n \gg l_H$), Eq.(D.1) would not change, as long as the change in density is induced by mechanisms not related to the Ohm's law and the momentum in the y -direction. At least this is true for the 1D MCX model presented in Chapter 2 with an artificial gravity directing in z . For MCX, geometry effect would certainly enter the calculation above. How much it would affect the result has to be investigated.

Appendix E

Preliminary Simulation in MCX Geometry

In this appendix, we attempt to solve the plasma-neutral system in the MCX geometry by extending the methods we used in Chapter 3 and “bypassing” the Hartmann physics. The works appear in this appendix is supposed to be preliminary due to the ignorance of some known physics and the limited simulation results at this stage.

In Chapter 3, we carry out 2D simulations in a slab geometry while modeling the centrifugal confinement using a gravity-like force term in the plasma momentum equation. However, there are major differences in that system and an authentic MCX geometry. First, the gravity force in the slab geometry only emulate the parallel-to-field component of the centrifugal force. Thus, it underestimates the perpendicular loss of plasma. Second, due to the charge-exchange interaction, the neutral rotates with the plasma to a certain extent. Since neutral is not bounded by the B-field, this rotation generates centrifugal force which is almost entirely in the radial direction. This force on the neutral is not considered in the slab geometry model. Third, in chapter 3, the simulation results show “semi-1D” behavior in the slab geometry. However, it is questionable that it would be the case in the MCX geometry because a mirror field is intrinsic 2D. Therefore, an analysis in the full MCX geometry would reveal more interesting behaviors.

In order to obtain a full MCX geometry analysis, there are two major points to be noted. First, we need to understand more about the boundary conditions because some of the mirror field lines end at the boundaries at angles other than 90-degree, when we keep using a rectangular box as the simulation domain. Second, in the MCX simulation, plasma flow in the azimuthal direction should be large (compared to sound speed). That also means that Hartmann flow problem might be important. If that is the case, a relatively thin boundary layer is generated. That is numerically expensive to resolve. One might suggest to include the Hall physics to broaden the Hartmann layer as we have shown in Chapter 4. Indeed, this is a good suggestion and should be done. However, to accurately simulate the Hall physics is also expensive and difficult numerically.

To overcome the boundary conditions problem[28, 29], in a quick way, we extend the idea of recombination layer used in Chapter 3 here. Fig. E.1 shows the contour of the recombination coefficient α_r we used. The red lines are the external mirror B-field. We essentially assume the external mirror field is almost unchanged during the simulation and that recombination rate are relative high outside the “Last Flux Surface” (LFS)¹. By LFS, we mean that this is the most exterior/interior field line that is not ending at the side walls. By doing so, we remove the question of determining the boundary conditions for tilted field lines. It is because the plasma density at those region are very small, the boundary conditions are not important anymore. For the Hartmann problem, the only quick fix is not to consider it! We do

¹Note that the maximum value of α_r is smaller than that we used in chapter 3 because of stability issue

this by using free-slip boundary condition at the end-wall, i.e. $\partial_z(nu_\theta) = 0$, where n is the plasma density and u_θ is the plasma azimuthal flow velocity. However, we still keep the no-slip boundary condition for the neutral azimuthal flow, that is making NU_θ antisymmetric, where N is the neutral density and U_θ is the neutral azimuthal flow. Since there is CX drag acting on the plasma by the neutral, the Hartmann flow physics is not totally be eliminated. Yet we found that boundary scale length of u_θ is very long compared to the Hartmann layer width. The azimuthal flow is driven by

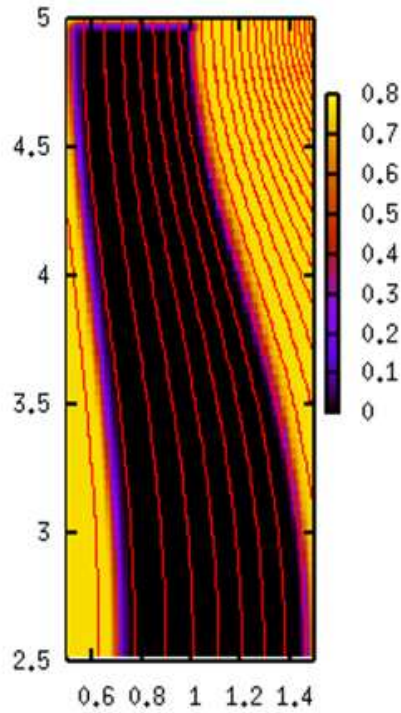


Figure E.1: Contour plot of recombination coefficient α_r in the MCX simulation. Red curves are the external mirror B-field. Recombination rate is then assumed to be high outside the “Last Flux Surface”

current. That is we set the $rB_y(z_w)$ to be a constant and extrapolate the boundary

values. This condition is obtained easily by setting the total radial current passing through the plasma be a constant and assuming azimuthal symmetry. Fig. E.2 shows the plasma density contour plots for the rotation Mach numbers at 0.8, 1.9 and 2.3. It is shown that plasma confinement is achieved as expect. Fig E.3 and E.4 show the corresponding neutral density and the product nN contour plots of the three simulations. Results suggest that the neutral density is decreasing at the end-wall and increasing at the side-wall as Mach number increases. Also, the dominant interaction region is shifting from the end-wall to the side which is along the outer LFS. It is in agreement with the result given by Chapter 3 except that the interior LFS is not a dominant interaction region. This can be explained by the fact an outward centrifugal force on the neutral is in effect due to the neutral azimuthal flow. However, different results from Chapter 3 can be seen when we look at the neutral flow vector plots. Fig. E.5 shows the 2D structures of the neutral flow. There are significant crossfield flow in front of the end-wall in all Mach numbers. It shows exactly how the neutral at the end-wall escapes to the low density region at the right-upper portion region and then approaches the core region along the side wall. Also the neutral up stream (toward mid-plane) flow is seen to be increasing as Mach number increases. The reason for this is still under investigation and thought to be related to the decreasing plasma/neutral density there. Indeed, the lowering of the plasma density there is now suspected to be the cause of numerical instability when high Mach number is attempted. Another even more important quantity that we can only explore now is the magnitude of CX frictional force acting on the plasma in the azimuthal direction. This is the value $nN(u_\theta - U_\theta)$ which is also the

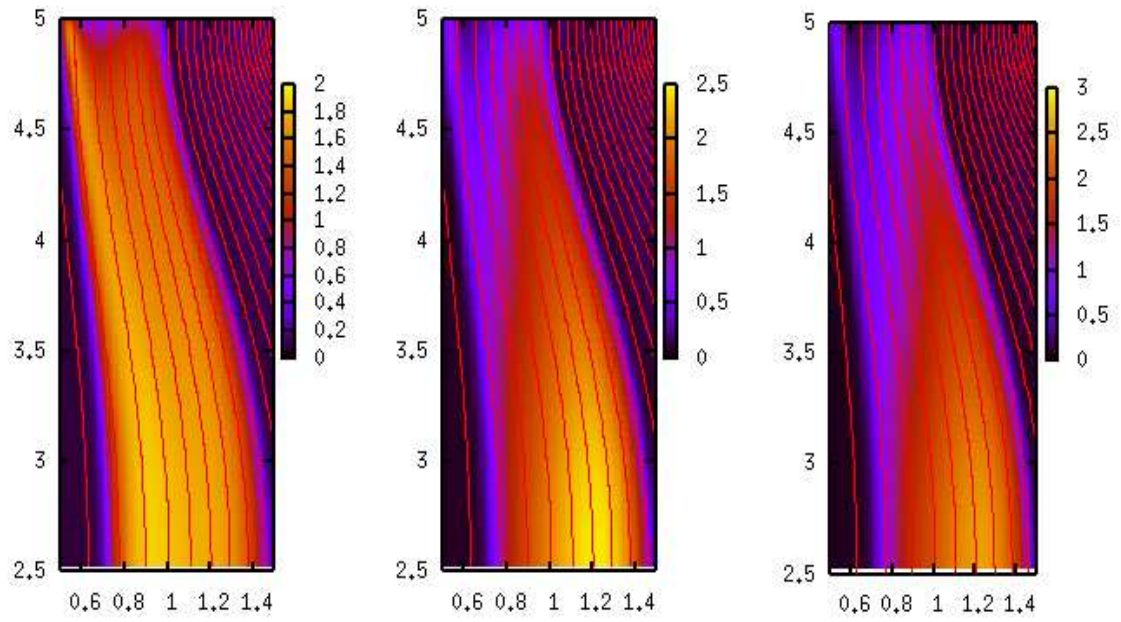


Figure E.2: Contour plots of plasma density distribution at different Mach numbers. Left: 0.8, middle: 1.9, right: 2.3. The red curve lines are the external mirror B-field lines. Centrifugal confinement is clearly demonstrated.

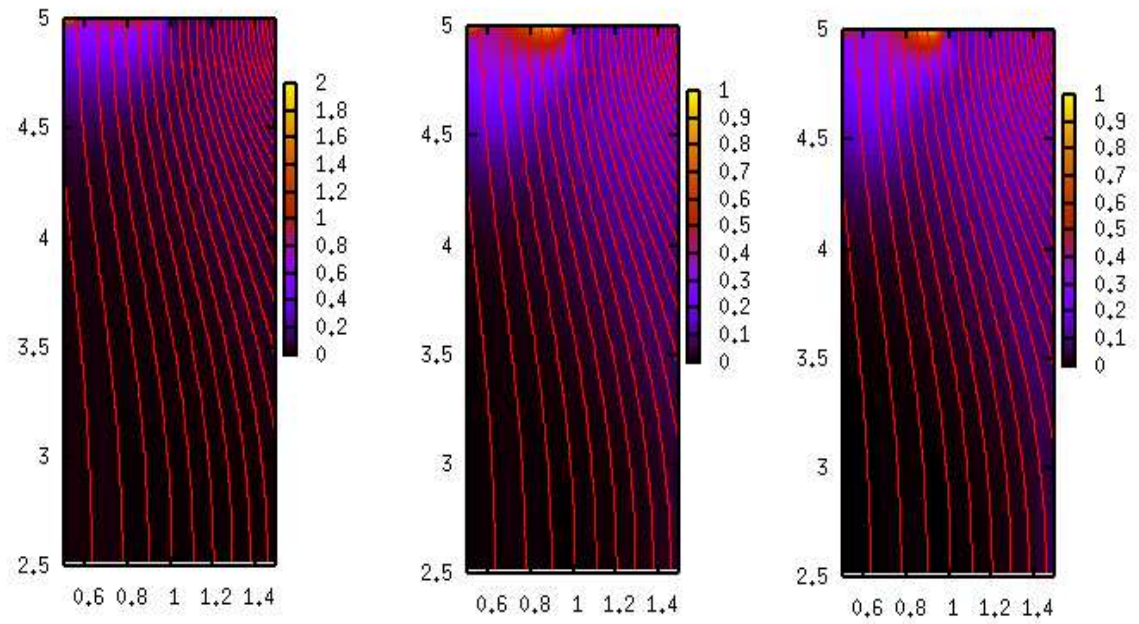


Figure E.3: Contour plots of neutral density distribution at different Mach numbers. Left: 0.8, middle: 1.9, right: 2.3. The red curve lines are the external mirror B-field lines. The end-wll neutral density is decreasing as the confinement gets better.

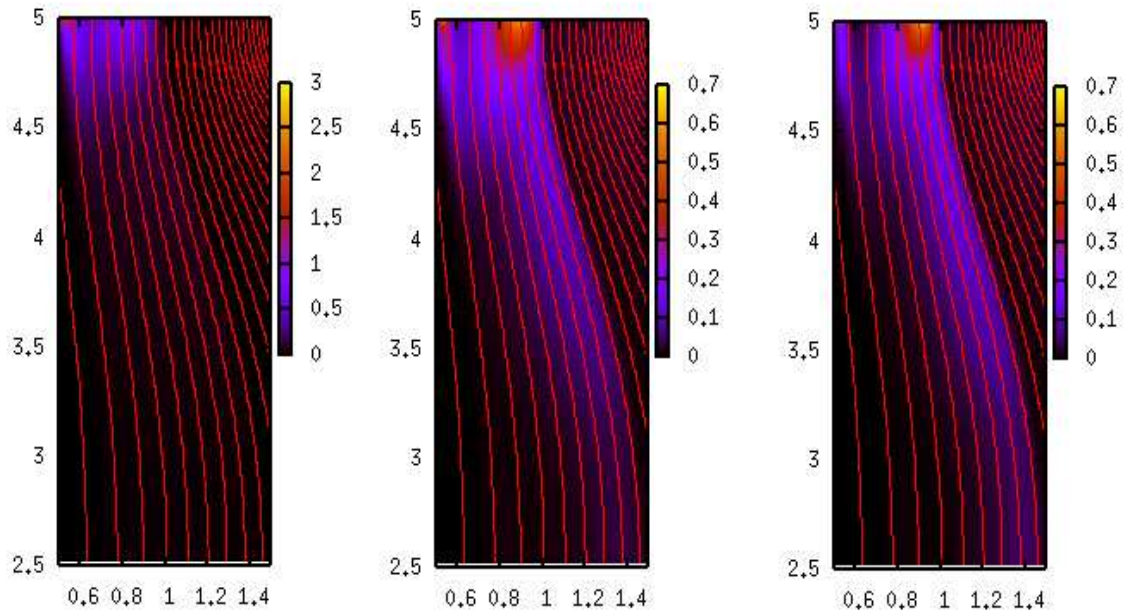


Figure E.4: Contour plots of interaction parameter nN distribution at different Mach numbers. Left: 0.8, middle: 1.9, right: 2.3. The red curve lines are the external mirror B-field lines. The dominant interaction region is shifting from the end-region to the side which, in this case, is along the LFS.

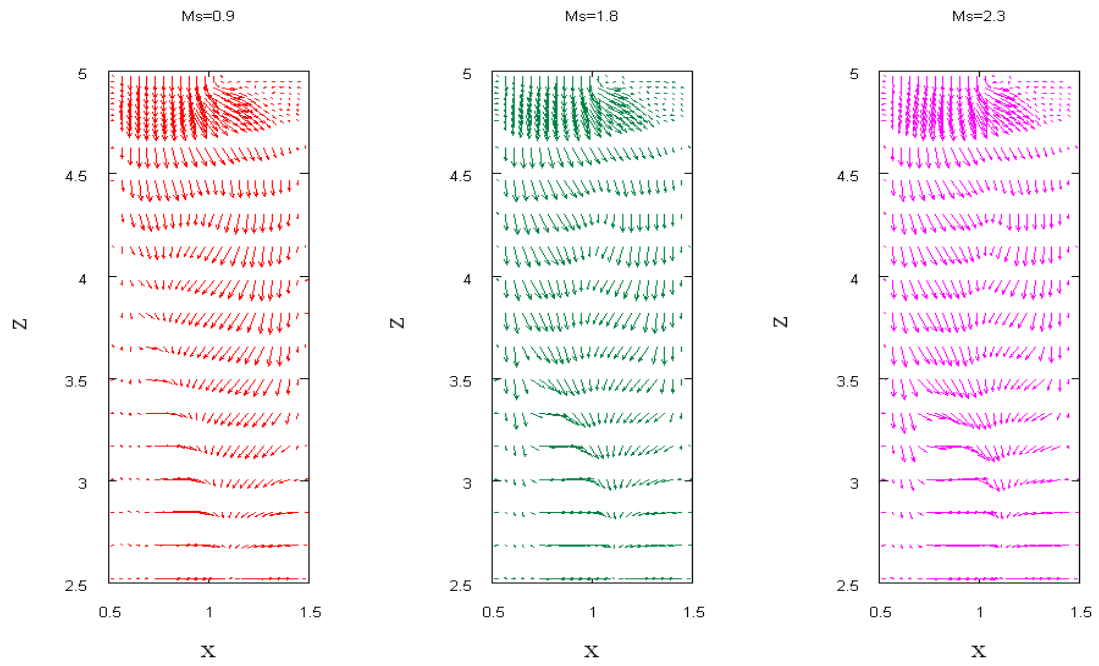


Figure E.5: Neutral flow vectors plots at different Mach numbers. Left: 0.8, middle: 1.9, right: 2.3. The red curve lines are the external mirror B-field lines. It shows the 2D flow structures in the mirror field geometry.

RHS (negative) term appears in the plasma momentum equation, Eq.(3.7). Fig. E.6 shows the contour plots of this quantity at different Mach numbers. It is found that the frictional force, although is decreasing as Mach number increases, is not negligible in the current parameter range. It is found that when we try to increase

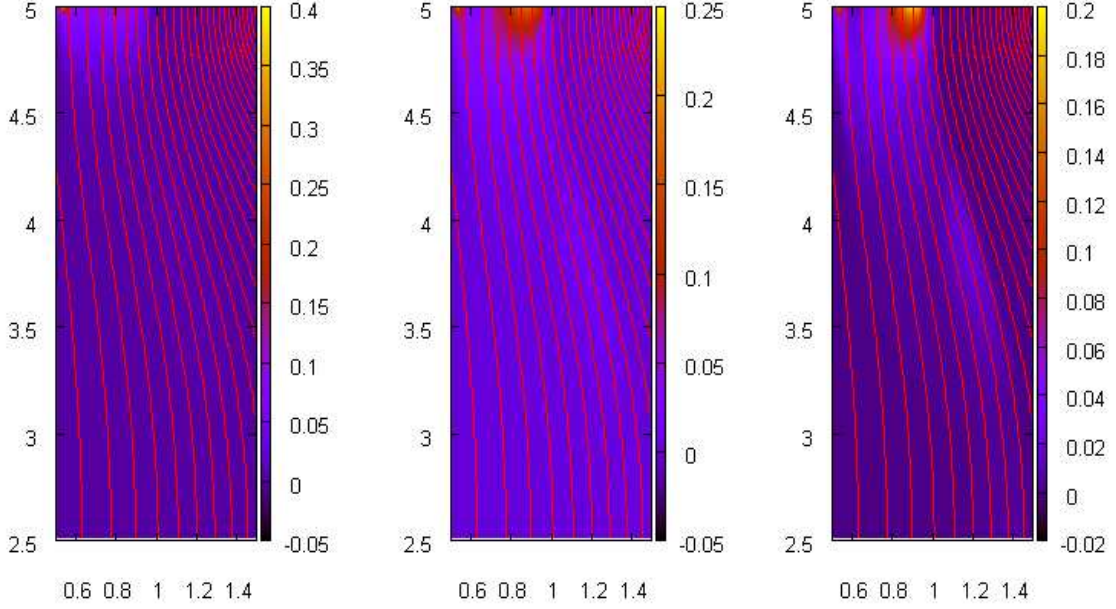


Figure E.6: Charge-exchange frictional force on plasma in the azimuthal direction, $nN(u_\theta - U_\theta)$, at different Mach numbers. Left: 0.8, middle: 1.9, right: 2.3. The red curve lines are the external mirror B-field lines. The frictional force is found to be decreasing and concentrating on the end-wall for this range of Mach numbers.

the Mach number further, numerical instability starts to appear. It is suspected that the plasma density at the interior region decreases so much that it goes negative and the code cannot handle this situation. However, a concrete explanation and resolution is still under investigation.

Appendix F

Simulation Parameters

In this appendix, we present the values of the physical parameters used in the 2D simulation. These values are determined according to some observations and assumptions of the MCX experimental parameters while being restricted by the computational resources available. Table F.1 shows the values of the physical parameters assumed for MCX. Table F.2 compares the normalized physical parameters assumed for MCX and those used in the 2D simulations.

Parameters	Assumed MCX values
B-field	0.2 Tesla
n_{core}	10^{20} m^{-3}
L_x	0.2 m
Temperature	15 eV
α_{cx}	$10^{-14} \text{ m}^3 \text{ s}^{-1}$
α_i	$10^{-14} \text{ m}^3 \text{ s}^{-1}$

Table F.1: Physical parameters assumed for MCX

Normalized Parameters	Assumed MCX values	2D Sim.
B-field	1	1
n_{core}	1	1
L_x	1	1
Temperature	0.008	0.04
α_{cx}	0.46	0.5
α_i	0.46	0.5
*Kinematic viscosity, ν	1.7×10^{-5}	0.005
*Resistivity, η	2×10^{-4}	0.005

*According to Braginskii[55]

Table F.2: Comparison of the normalized physical parameters assumed for MCX and those used in the 2D simulations

Bibliography

- [1] B. Lehnert. Rotating plasmas. *Nuclear Fusion*, 11:485–533, 1971.
- [2] R. F. Ellis, A. B. Hassam, S. Messer, and B. R. Osborn. An experiment to test centrifugal confinement for fusion. *Phys. Plasmas*, 8(5):2057–2065, 2001.
- [3] R. F. Ellis, A. Case, R. Elton, J. Ghosh, H. Griem, A. B. Hassam, R. Lunsford, S. Messer, and C. Teodorescu. Steady supersonically rotating plasmas in the Maryland Centrifugal experiment. *Phys. Plasmas*, 12(5):Art. No. 055704, 2005.
- [4] J. Ghosh, R. C. Elton, H. R. Griem, A. Case, A. W. DeSilva, R. F. Ellis, A. B. Hassam, R. Lunsford, and C. Teodorescu. Radially resolved measurements of plasma rotation and flow-velocity shear in the maryland centrifugal experiment. *Phys. Plasmas*, 13(2):Art. No. 022503, 2006.
- [5] R. F. Ellis C. Teodorescu, , A. Case, R. Clary, A. B. Hassam, R. Lunsford, and S. Messer. New high rotation mode in magnetized rotating plasmas. *Plasma Phys. Controlled Fusion*, 48(7):945–954, 2006.
- [6] A. B. Hassam. Nonlinear stabilization of the rayleigh-taylor instability by external velocity shear. *Phys. Fluids B-Plasma Phys*, 4:485–487, 1992.
- [7] Yi-Min Huang and A. B. Hassam. Velocity shear stabilization of centrifugally confined plasma. *Phys. Rev. Lett.*, 87(23):Art. No. 235002, Nov 2001.
- [8] S. W. Ng and A. B. Hassam. Finite larmor radius assisted velocity shear stabilization of the interchange instability in magnetized plasmas. *Phys. Plasma*, 12:Art. No. 064504, 2005.
- [9] C. S. Pitcher and P. C. Stangeby. Experimental divertor physics. *Plasma Phys. Control. Fusion*, 39:779–930, 1997.
- [10] T. D. Rognlien. Understanding of edge plasmas in magnetic fusion energy devices. *Plasma Phys Control. Fusion*, 47:A283–A295, 2005.
- [11] Fülöp T., P. J. Catto, and P. Helander. Neutral diffusion and anomalous effects on ion flow shear. *Phys. Plasmas*, 5(9):3398–3401, 1998.
- [12] Fülöp T., P. J. Catto, and P. Helander. Effect of neutral atoms on takamak edge plasmas. *Phys. Plasmas*, 8(12):5214–5220, 2001.
- [13] P. J. Catto, P. Helander, J. W. Connor, and R. D. Hazeltine. Neutral particle and radiation effects on pfirsch-schlüter fluxes. *Phys. Plasmas*, 5(11):3961–3968, 1998.

- [14] T. D. Rognlien, J. L. Milovich, M. E. Rensink, and G. D. Porter. A fully implicit, time-dependent 2-d fluid code for modeling tokamak edge plasmas. *J. Nuclear Mater.*, 196:347–351, 1992.
- [15] D. Heifetz, D. Post, M. Petravic, J. Weisheit, and G. Bateman. A monte-carlo model of neutral-particle transport in diverted plasmas. *J. Comp. Phys.*, 46:309–327, 1982.
- [16] P. C. Stangeby. *The Plasma Boundary of Magnetic Fusion Devices*. Institute of Physics Pub., Philadelphia, 2000.
- [17] A. Fruchtman, G. Makrinich, P. Chabert, and J. M. Rax. Enhanced plasma transport due to neutral depletion. *PRL*, 95:Art. No. 115002, 2005.
- [18] J. Hartmann. Det kgl. danske videnskabernes selskab. *Mathematisk-fysiske Meddelelser*, XV:1–27, 1937.
- [19] R. J. Goldston and P. H. Rutherford. *Introduction to Plasma Physics*. Institute of Physics Publishing, Bristol and Philadelphia, 1995.
- [20] D. E. Post and Behrisch R., editors. *Physics of Plasma-Wall Interactions in Controlled Fusion*. Plenum Press, New York, 1986.
- [21] J. Wesson. *Tokamaks*. Oxford University Press, Inc., New York, 2nd. edition, 1997.
- [22] I. Langmuir. The interaction of electron and positive ion space charges in cathode sheaths. *Phys. Review*, 33:954, 1929.
- [23] D. Bohm. *The Characteristics of Electrical Discharges in Magnetic Fields*. McGraw-Hill, New York, 1949.
- [24] K. U. Riemann. The bohm criterion and sheath formation. *J. Phys. D-applied Phys.*, 24(4):493–518, 1991.
- [25] K. U. Riemann. Plasma-sheath transition in the kinetic Tonks-Langmuir model. *Phys. Plasmas*, 13(6):Art. No. 063508, 2006.
- [26] V. Godyak and N. Sternberg. On the consistency of the collisionless sheath model. *Phys. Plasmas*, 9(11):4427–4430, 2002.
- [27] R. N. Franklin. Comment on "On the consistency of the collisionless sheath model". *Phys. Plasmas*, 10(11):4589–4589, 2003.
- [28] P. C. Stangeby and A. V. Chankin. The ion velocity (bohm-chodura) boundary-condition at the entrance to the magnetic presheath in the presence of diamagnetic and exb drifts in the scrape-off layer. *Phys. Plasmas*, 2(3):707–715, 1995.
- [29] I. H. Hutchinson. The magnetic presheath boundary condition with ExB drifts. *Phys. Plasmas*, 3(1):6–7, 1996.

- [30] B. Lehnert. Screening of a high-density plasma from neutral gas penetration. *Nuclear Fusion*, 8:173–181, 1968.
- [31] B. Lehnert. Quasi-steady plasma-neutral gas balance in magnetic bottles. *Physica Scripta*, 12:327–336, 1975.
- [32] B. Lehnert. Plasma-neutral gas boundary layers. *Nuclear Instruments and Methods*, 129:31–37, 1975.
- [33] Peter J. Catto. A short mean-free path, coupled neutral-ion transport description of a tokamak edge plasma. *Phys. Plasmas*, 1:1936–1943, 1994.
- [34] Mathematica(trademark) 5.0, wolfram research, inc., 2003.
- [35] T. D. Rognlien and M. E. Rensink. Edge-plasma models and characteristics for magnetic fusion energy devices. *Fusion Eng. and Design*, 60:497–514, 2002.
- [36] Yi-Min Huang and A. B. Hassam. Magnetorotational and parker instabilities in magnetized plasma dean flow as applied to centrifugally confined plasmas. *Phys. Plasmas*, 10(1):204–213, 2003.
- [37] Yi-Min Huang and A. B. Hassam. Resistive magnetohydrodynamic equilibrium and stability of a rotating plasma with particle sources. *Phys. Plasmas*, 11(8):3738–3747, 2004.
- [38] Yi-Min Huang and A. B. Hassam. Magnetohydrodynamic stability of centrifugally confined plasmas. *Phys. Plasmas*, 11(5):2459–2465, 2004.
- [39] Yi-Min Huang, D. Goel, and A. B. Hassam. Ideal magnetohydrodynamic interchanges in low density plasmas. *Phys. Plasmas*, 12(3):Art. No. 032107, 2005.
- [40] B. Lehnert. Stability of plasmas penetrated by neutral gas. *Nuclear Fusion*, 13:781–791, 1973.
- [41] M. Z. Tokar. Self-sustained oscillations in a plasma-wall system with strongly inhomogeneous diffusion of charged particles. *Phys. Rev. Lett.*, 95:Art. No. 265002, 2005.
- [42] E. L. Vold, A. K. Prinja, Najmabadi F., and R. W. Conn. Coupled plasma-neutral fluid transport computations using the neutral diffusion approximation. *Fusion Tech.*, 22:208–226, 1992.
- [43] T. D. Rognlien, D. D. Ryutov, N. Mattor, and G. D. Porter. Two-dimensional electric fields and drifts near the magnetic separatrix in divertor tokamaks. *Phys Plasmas*, 6(5):1851–1857, 1999.
- [44] P. N. Guzdar, J. F. Drake, McCarthy D., Hassam A. B., and C. S. Liu. Three-dimensional fluid simulations of the nonlinear drift-resistive ballooning modes in tokamak edge plasmas. *Phys. Fluids B-Plasma Phys.*, 5:3712–3727, 1993.

- [45] P. Guzdar and I. Shamim. Model for the high-rotation to ordinary-mode transitions observed in MCX. College Park, Maryland, USA, 2007. Innovative Confinement Concepts Workshop.
- [46] J. D. Jackson. *Classical Electrodynamics*. John Wiley & Sons, Singapore, 2nd edition, 1975.
- [47] Yi-Min Huang. *Magnetohydrodynamic Equilibrium and Stability of Centrifugally Confined Plasmas*. PhD thesis, University of Maryland, College Park, August 2004.
- [48] H. Alfvén. *On the Origin of the Solar System*. Clarendon Press, Oxford, 1954.
- [49] B. Lehnert. The partially ionized plasma centrifuge. *Physica Scripta*, 7:102–106, 1973.
- [50] Robert Lunsford. *Parametric Limitations on Discharge Performance in the Maryland Centrifugal Experiment*. PhD thesis, University of Maryland, College Park, January 2007.
- [51] J. C. R. Hunt and K. Stewartson. Magnetohydrodynamic flow in rectangular ducts. ii. *J. Fluid Mech.*, 23:563–581, 1965.
- [52] H. E. Wilhelm and S. H. Hong. Boundary-value problem for plasma centrifuge at arbitrary magnetic Reynolds numbers. *Phys. Review A*, 15:2108–2116, 1977.
- [53] U. Müller and L. Bühler. *Magnetofluidynamics in Channels and Containers*. Springer, Berlin, 2001.
- [54] T. Nagy and Dememdy. Z. Effects of Hall currents and Coriolis force on Hartmann flow under general wall conditions. *Acta Mechanica*, 113:77–91, 1995.
- [55] S. I. Braginskii. *Reviews of Plasma Physics*, volume 1, page 205. Interscience, New York, 1965.